Micro Black Holes at the LHC and An X-ray Survey of the ATLAS SCT

Nick Brett

Sub Department of Particle Physics

University of Oxford

n.brett1@physics.ox.ac.uk

August 20, 2007

Contents

1

The ATLAS Experiment

1.1 Introduction

The ATLAS experiment aims to extend the knowledge of particle physics beyond the energies and statistical limits it currently faces. ATLAS is a particle detector designed to operate at the Large Hadron Collider (LHC) based at CERN, the European Organisation for Nuclear Research. The LHC will collide particles with energies far in excess of those achieved by any previous machine. The ATLAS detector, along with a number of other experiments, will observe the properties and behaviour of the particles involved in those collisions. This will expose the ATLAS experiment to so far unobserved phenomena and possibly to as yet unknown new physics.

Particle physics observations made to date can be accounted for by a set of related theoretical models known as the Standard Model of particle physics (SM). This model describes the observed physics very well but leaves a number of questions unanswered. The origin of the mass of SM particles is unaccounted for and the process by which the disparate theories in the SM can be connected together is also uncertain. Further theories exist which offer solutions to these and other questions raised by the SM but are yet to be confirmed or excluded by observation. The LHC in general and the ATLAS detector specifically set out to make these required observations and extend the reach of modern particle physics knowledge.

The LHC and the ATLAS detector are described in more detail in the sections that follow.

1.2 The Large Hadron Collider

The Large Hadron Collider is a new particle accelerator currently under construction at CERN. The LHC will primarily operate as a proton-proton collider but is also capable of accelerating heavy lead ions for $\mathrm{P_b} - \mathrm{P_b}$ collisions.

The LHC is over 27 km long and forms a closed circle with a diameter of approximately 8 km. The accelerator is housed in a tunnel located between 50 m and 175 m bellow ground level on the outskirts of Geneva. This is the same tunnel as was once occupied by the Large Electron Positron (LEP) collider. The layout of the LHC engineering work is shown in figure 1.1.

There are several stages involved in accelerating beam of particles before they actually reach the LHC. Protons are produced by striping the electrons from hydrogen atoms. A linear accelerator (Linac2) is used to accelerate the protons to an energy of 50 MeV and inject them into the Proton Synchrotron Booster (PSB) ring. The protons leave the PSB with an energy of 1.4 GeV and enter the Proton Synchrotron (PS) ring where they are boosted to an energy of 25 GeV before being injected into the Super Proton Synchrotron (SPS) and taken to an energy of 450 GeV. The proton beam is then divided

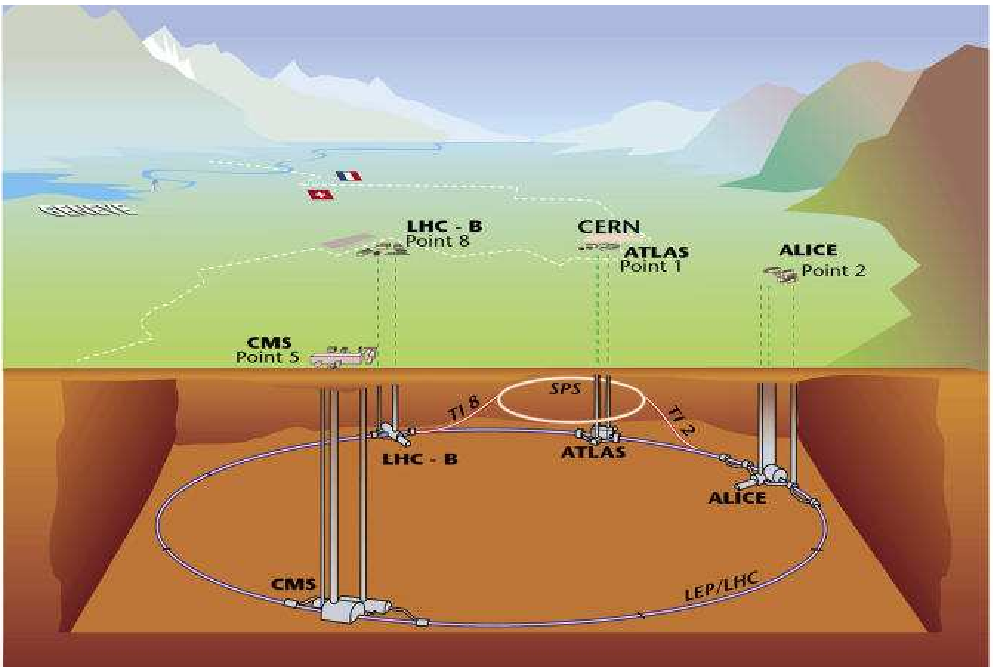

Figure 1.1: The image shows a simplified drawing of the excavations under Geneva which house the LHC and the related experiments. The accelerator tunnel is shown as a white ring passing through the caverns containing the ATLAS, ALICE, CMS and LHC-b experiments. The SPS is also shown as a smaller white ring above the ATLAS cavern with two injector tunnels connected to the LHC. The surface of the ground is shown above the excavations in green along with lake Geneva and the Swiss-French border marked by a dashed white line.

in two and delivered to the LHC itself in counter rotating directions. The LHC relies on superconducting Radio Frequency (RF) cavities to further increase the beam energy. A total of sixteen cavities are involved, eight per beam arranged in two sets of four. The RF cavities are responsible for accelerating the proton beams in the LHC from the injection energy of 450 GeV to the final energy of 7 TeV per proton.

The LHC employs two separate beam pipes which run parallel to one another, each guiding a beam of protons in opposite directions. The beams are manipulated by a system of 9300 magnets including dipoles, quadrupoles, sextupoles, octupoles, decapoles etc. A total of 1232 superconducting dipole magnets are required to confine the counter rotating beams to the circular path of the LHC. The magnetic field lines form a circle in the plane perpendicular to the direction of the beams. This means that the two beam pipes placed one on either side of the accelerator experience magnetic fields in opposite directions. Positively charged protons can be accelerated in the clockwise direction in one pipe and the anti-clockwise direction in the other.

Both the magnets and the RF accelerators must be cryogenicly cooled and as a result the LHC is currently the largest cold mass in the world. The accelerator cavities operate at a temperature of 4.5 K whilst the dipole magnets are cooled to an operating temperature of 1.9 K by liquid helium. The niobium-titanium (NbTi) cables that generate the dipole field actually become superconducting at the higher temperature of 10K. The lower operating temperature is due to the nature of the coolant. Helium becomes a super-fluid at $\sim 2.17\ K$ which posses a very high thermal conductivity, improving its ability to cool the magnets.

When operating at full capacity, the LHC should be capable of producing proton-proton collisions with a maximum Centre of Mass (CoM) energy of 14 TeV. This is an order of magnitude higher than the current world leading hadron accelerator, the Tevatron at Fermi Lab, which achieves a CoM energy of ∼2 TeV. The two beams will each consist of 2808 bunches of $1.15x10^{11}$ protons. The bunches will be a few centimetres in length with a transverse dimension on the order of millimetres whilst in the accelerator. However, the bunches are *squeezed* before entering any of the interaction points, reducing the transverse dimension to 16 μm in order to maximise the rate of collisions.

The LHC has a design luminosity of $10^{34}\mathrm{m}^{-2}\mathrm{s}^{-1}$ with the possibility of a 100 fold increase being implemented as part of a proposed upgrade (referred to as Super LHC) approximately 10 years after the machine is first switched on. Protons are accelerated in bunches (groups of particles). The rate at which bunches travelling in opposite directions pass through one another at the designated interaction points (the bunch crossing frequency) is 40 MHz. At design luminosity each bunch crossing will result in an average of 23 proton-proton interactions and lead to particles impacting on the detector surrounding each interaction point. Therefore the bunch crossings determine the clock signal used to synchronise the LHC electronics with those employed by each of the different particle detectors.

The effect of having multiple interactions per bunch crossing is that particles produced by completely different interactions may pass through the detector at effectively the same time. This effect is often referred to as *pile-up* and presents a challenge to experimental physicists interpreting LHC data. The most promising mechanism for separating the products of different interactions involves computing the initial vertex, the point in space where the proton-proton collision actually occurred. These vertices's should be well confined in the xy plane as a result of focusing the proton beams. system. However, the distribution of the vertices's in the z direction, along the beam line, should be comparatively large.

The construction schedule of the LHC is constantly changing to keep pace with unprecedented developments. Current projections put the time for closing the accelerator and producing the first beam somewhere near the end of 2007. Initial running will involve proton-proton collisions with a CoM energy of approximately 900 GeV, the energy provided by the SPS upon injection to the LHC. 14 TeV collisions will not occur until the bending magnets have been fully tested using the low energy beam, a task which could take some six months and places the start of design energy collisions somewhere in 2008.

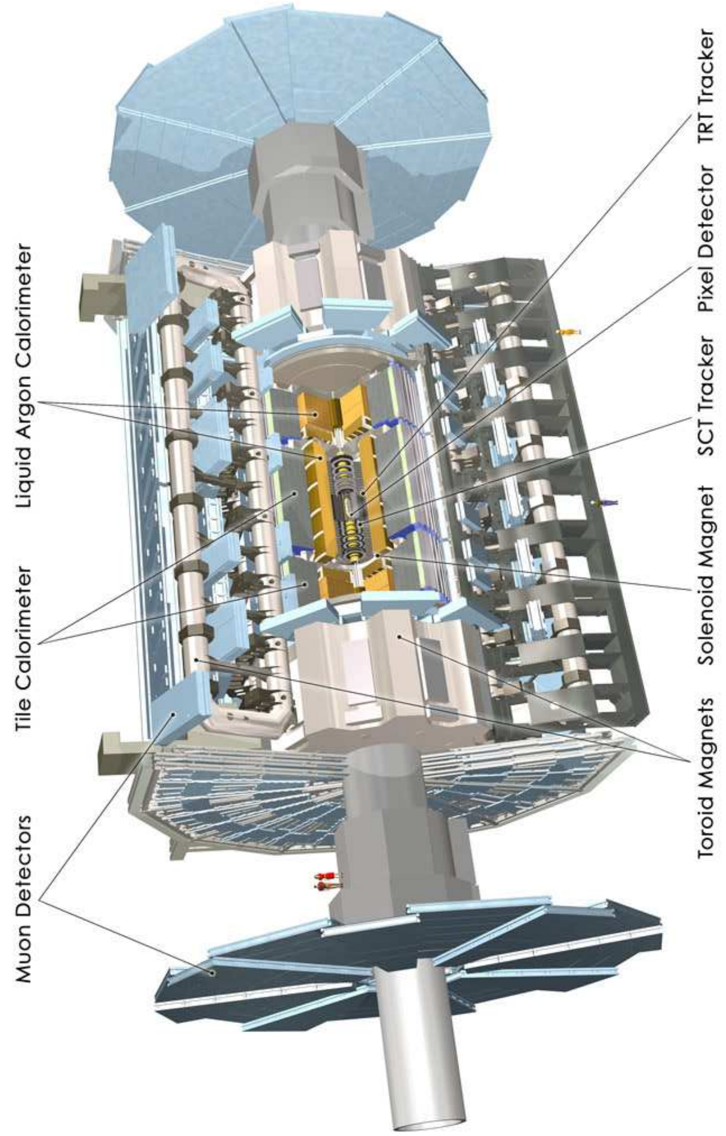

Figure 1.2: A computer generated image of the final proposal for the ATLAS particle detector. The prominent sub-detectors are labelled in the diagram. The inner detector is shown in the centre of the diagram, surrounded by the EM (Liquid Argon) calorimeter (yellow) and the hadronic (tile) calorimeter (grey). The detector is approximately 22m in diameter and 44m along its major axis. The figure includes four standard people to give an idea of scale.

1.3 The ATLAS Detector

ATLAS (an acronym which stands for *A Toroidal LHC ApparatuS*)is a multipurpose particle detector currently under construction at CERN for operation at the LHC. The detector is approximately 22 m in diameter and 44 m in length with a total mass of ∼7000 Tons. Figure 1.2 shows a computer generated image of the ATLAS detector which has been cut away to reveal some of the more important sub-systems.

ATLAS has been designed as a general purpose detector to observe previously unseen physics in the new energy regime opened up by the LHC. The detector has been equipped to detect and identify the majority of particles produced by the physics processes occurring at its centre. Some regions of the detector are occupied by cabling and other support structures which impede its ability to measure physics processes. An understanding of these limitations is vital to physics studies performed using ATLAS data or related simulations.

The ATLAS detector has an approximately cylindrical shape with the accelerator running along its axis, as can be seen in figure 1.2. The detector is often described using a cylindrical polar coordinate system. The interaction point at the very centre of the detector sits at the origin of this coordinate system whilst the accelerator lays along the z-axis. Rotation about the z-axis is labelled ϕ with zero pointing directly upwards whilst radial distance from the z-axis is sometimes referred to as r. The velocity of a particle leaving the interaction point is more easily described using ϕ in this coordinate system and the pseudo-rapidity η[1] The value of η can be positive or negative, depending on the sign of the velocities component along the z-axis. The magnitude of η is small for velocities with a small z-component and infinitely large for velocities which run parallel

[1] $\eta = -ln\left(tan\left(\frac{\theta}{2}\right)\right)$ Where θ is the angle between the z-axis and the direction of the particle.

to the z-axis.

ATLAS consists of a number of sub-detectors, each designed for different but complimentary purposes. Starting from the centre of the detector, ATLAS includes a set of pixel and silicon strip detectors, a transition radiation detector, electromagnetic and hadronic calorimeters and finally, a muon spectrometer. Notable features of the detector include the large air core superconducting toroid's which make up the muon spectrometer, accounting for a majority of the detectors physical volume. The sub-detectors are discussed in more detail in the sections that follow. Typically particle detectors employ a magnetic field to measure the momentum of charged particles. A large magnetic field is generated at several points within the the ATLAS detector for precisely this purpose. The field permeates through the entire detector and its shape is slightly more complicated than that used in the majority of particles detectors. The magnetic field and detector sub-systems are discussed in more detail below. Further details can be found in the ATLAS Technical Design Report (TDR) [2].

1.3.1 The Inner Detector

The inner detector (ID) comprises the central tracking region of ATLAS. Working outwards from the beam pipe, this consists of the pixel detector, the Semi-Conductor Tracker (SCT) and the Transition Radiation Tracker (TRT). These components are all contained within a compact super-conducting magnetic solenoid (CS) which is capable of generating a uniform 2 T magnetic field throughout most of the volume occupied by the ID. Figure 1.3 shows a computer generated image of the ID whilst table 1.1 provides a summary of the ID sub-components with their extent in η and r.

The purpose of the ID is to track the passage of charged particles as they leave the

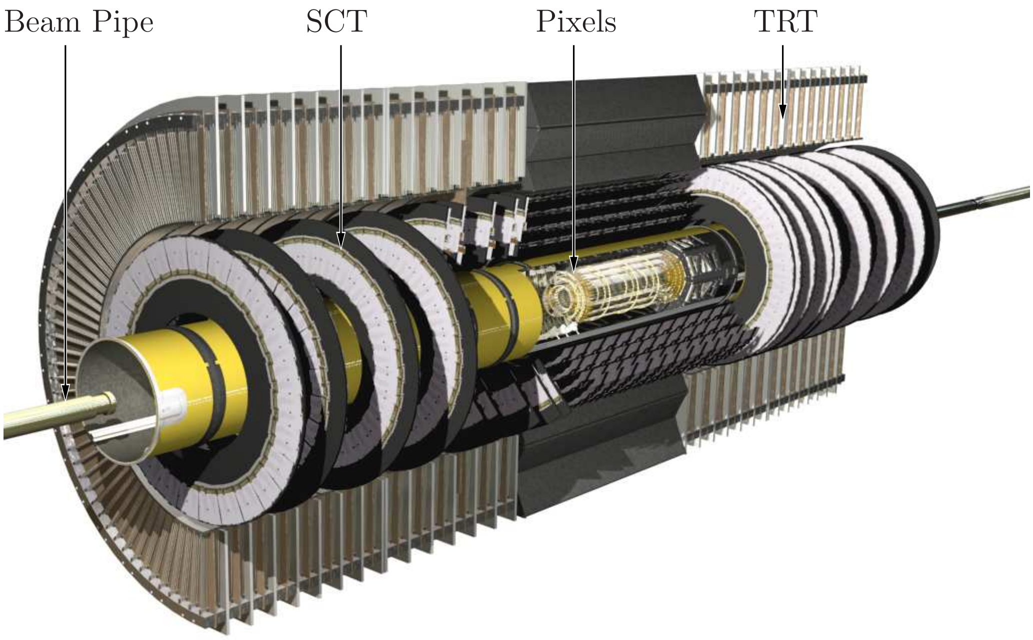

Figure 1.3: A computer generated image of the inner detector. The yellow cylinder running through the centre of the diagram represents the enclosure surrounding the beam pipe and its associated services. The construction in the very centre of the figure, within the yellow cylinder represents the pixel detector whilst the structure immediately outside the yellow cylinder represents the SCT. The shape and location of the TRT is indicated by the outermost structure in the diagram.

interaction point at the centre of the detector. The components of the ID record the location of points where charge has been liberated by the passage of a high energy charged particle. These points, known as *hits* are fitted with helical functions to form *tracks* representing the path a particle took through the ID. Each track can then be associated with a reconstructed particle and its curvature in the ID's magnetic field can be used to determine the particles momentum. The highest precision in hit position measurement is required nearest the IP and is provided by the silicon pixel detector. The SCT and TRT have successively poorer position resolution.

The $1/P_T$ resolution of the ATLAS ID is shown in figure 1.4 as a function of η for

component	**section**	**position in η**	**position in r**
Pixel	b-layer	$\|\eta\| < 2.5$	40mm
	barrel	$\|\eta\| < 1.7$	110mm and 130mm
	end-cap	$1.7 < \|\eta\| < 2.5$	$110 < r < 200$mm
SCT	barrel	$\|\eta\| < 1.4$	300mm, 373mm, 447mm and 520mm
	end-cap	$1.4 < \|\eta\| < 2.5$	$270 < \|r\| < 560$mm
TRT	barrel	$\|\eta\| < 0.7$	$560 < r < 1070$mm
	end-cap	$0.7 < \|\eta\| < 2.5$	$480 < r < 1030$mm
CS	barrel	$\|\eta\| < 2.5$	1150mm

Table 1.1: Summary of the physical extent of all sub-components comprising the ATLAS inner detector[3].

samples of single muons with energies of 0.5, 5, 20 and 1000 GeV. All of the plots in the figure show a degradation in resolution with increasing η. The three sub-detectors of the ID are described in more detail bellow.

Pixels

The pixel detector consists of three concentric cylinders in the barrel section and ten disks, five each at positive and negative z. The inner most barrel is known as the b-layer, this is mounted directly onto the beam pipe and is removable. The pixel detector is so named because of the manner in which its active detector components are arranged. Instead of employing strips with a stereo angle as used in the SCT described bellow, the silicon is divided into active blocks 50 μm in $r\phi$ and 300 μm in z. This removes the ambiguity in hit position normally associated with silicon strip detectors and allows for very good vertex resolution, even in the z direction.

Semi-Conductor Tracker

The Semi-Conductor Tracker (SCT) occupies a large part of the ATLAS tracking volume. The SCT can be divided into three parts, the barrel section which extends to $|\eta| < 1.3$ and two end-cap sections which cover the range $1.3 < |\eta| < 2.47$. The barrel section consists of four concentric cylinders 1.85 m in length whilst the end-caps each consist of nine wheels 1.94 m in length with a diameter of 1.14 m. The four barrels are labelled 3 to 6, accounting for the three layers of the pixel detector. The SCT is made up of a carbon fibre support structure on which a number of silicon strip detectors called *modules* are mounted, along with the associated services. The modules mounted in the barrel and end-cap sections are slightly different. All of the modules are constructed from two layers of silicon strips mounted back to back with a slight stereo angle between the two. In the barrel section the modules have their strips approximately aligned with the z-axis. The strips produce hit position measurements in $r\phi$ whilst the stereo angle and the combination of two strip measurements is used to find the position in the z direction. The modules in the end-cap have their strips aligned in the radial direction, perpendicular to the z-axis. Here, the stereo angle between the strips is used to determine the radial position of a hit. There are 4088 silicon strip detectors, know as modules mounted on the SCT with a combined total of 6.3 million read out channels. The SCT and the silicon modules are described in more detail in chapter 7.

Transition Radiation Tracker

The Transition Radiation Tracker (TRT) is positioned between the SCT and the EM calorimeter. The tracker consists of a large number of 4 mm diameter *straw tubes*, each containing xenon gas and a 30 μm diameter gold-plated sense wire. There are 50 000 tubes in the barrel section, running parallel to the z-axis and 320 000 in the forward sections installed perpendicular to the z-axis. Each of the tubes in the barrel are divided in half and read out at each end, leading to a sub-detector with a total of 420 000 read out channels. The TRT is designed to collect a large number of data points for each reconstructed track. A charged particle passing through the TRT should interact with approximately 36 individual straw tubes.

The TRT is useful in electron identification. The straw tubes are surrounded by a radiator material which emits x-rays upon the passage of a charged particle. This is the "transition radiation" mentioned in the sub-detectors name. The intensity of the transition radiation is related to the mass and energy of the charged particle. Xenon gas is employed in the tubes enabling the detection of the x-rays. The read out modules for each of the tubes are aware of two different thresholds and can report whether the charge collected by an individual wire is above the low threshold or the high threshold. Transition radiation will increase the amount of ionisation in a straw tube so increase the probability of exceeding the high threshold. An electron can be identified as such by considering the ratio of high threshold hits to total hits in its associated track.

1.3.2 Calorimetry

The ATLAS calorimetry system has been designed to provide good energy and position measurements as well as excellent missing E_T recovery. Figure 1.5 shows a simplified representation of the ATLAS calorimetry sub-system.

The calorimetry system can be separated into two distinct parts. The Electromagnetic (EM) calorimeter which is designed to contain most of the energy deposited by electrons and photons and the Hadronic calorimeter (Had) which collects hadronic energy deposits which extend beyond the depth of the EM calorimeter. The total combined mass of the ATLAS calorimeters, including the magnetic flux return for the inner solenoid (which is built into the hadronic tile calorimeters support structure) is 4000 Tons. Table 1.2 shows the range in η covered by each of the calorimeter sub-systems.

component	**section**	**position in η**
Electromagnetic	barrel	$\lvert\eta\rvert < 1.475$
	end-cap	$1.375 < \lvert\eta\rvert < 3.2$
Hadronic	barrel	$\lvert\eta\rvert < 1.6$
	end-cap	$1.6 < \lvert\eta\rvert < 3.2$
	forward	$3.1 < \lvert\eta\rvert < 4.9$

Table 1.2: Showing the pseudo-rapidity η range covered by the different parts of the ATLAS calorimeter.

The ATLAS calorimetry is not uniform over the entire range of η. The design of both the EM and Had calorimeters varies across η along with the physics requirements and construction challenges. There is a section of dead material covering the range $1.375 < |\eta| < 1.475$ which is known as the gap-region. This gap-region acts as a conduit for services required by the inner detector such as power cables, optical fibres and cryogenic fluid supplies. Electromagnetic and Hadronic energy reconstruction is known to be poor in this region. The EM and Had calorimeters are described in more detail in the following two sections.

Electromagnetic Calorimeter

The Electromagnetic (EM) calorimeter is based on a lead/liquid argon scintillator design with an accordion geometry. The calorimeter incorporates a total of 190 000 readout channels, has a depth of more than $24X_0$ (radiation lengths) in the barrel section and above $26X_0$ in the end-cap. Figure 1.6 below presents the EM calorimeter design, showing a radial section through the different sampling layers.

The barrel section of the EM calorimeter is made up of two half barrels, separated by a 6mm gap at z equals zero. The EM calorimeter is positioned behind the ID, cryostat and compact solenoid. The barrel section of the EM calorimeter is divided into three layers. The first layer with a constant thickness of $6X_0$ (including upstream material) is positioned in front of the EM calorimeter to facilitate measurements of shower shape before entering the main section of the calorimeter. This means that the amount of showering and therefore energy loss undergone by a particle before reaching the EM calorimeter can be estimated and accounted for. This layer covers the range $|\eta| < 1.8$ and consists of fine strips with a size of $\Delta\eta \times \Delta\phi = 0.003 \times 0.1$ and a separation of $\sim 4mm$. These strips run in the $r\phi$ direction, providing shower shape measurement in the η direction. The magnetic field in the ID distorts the shape of any EM shower in the phi direction making measurements of shower shape less useful along that axis. The second, middle sampling represents the bulk of the calorimeter's depth (extent in R) and is intended to collect the majority of any electromagnetic energy deposits. The total depth of the calorimeter and all upstream material before the end of the second sampling is $\sim 24X_0$. The second sampling is segmented into square towers of size $\Delta\eta \times \Delta\phi = 0.025 \times 0.025$ which is approximately equal to $4 \times 4cm$ at $\eta = 0$. The third, back sampling is a thin layer at the back of the calorimeter with a depth that varies in η between $2X_0$ and $12X_0$ and a granularity half that of the second sampling. Energy deposited in this layer is used to estimate the amount of electromagnetic energy that may have escaped the EM calorimeter and been lost in the cryostat before the Had calorimeter or entered the Had calorimeter itself, a quantity referred to as *Hadronic leakage*.

The EM calorimeter is augmented with a pre-sampling layer in the region $|\eta| < 1.8$

where the material in front of the calorimeter exceeds $\sim 2X_0$. The pre-sampler consists of a lead/LAr layer which is 1.1 cm thick in the barrel region and 0.5 cm in the end-cap. This additional layer is designed to compensate for losses in material upstream of the calorimeter.

Energy measurements performed using the calorimeter take account the energy deposited in the different sampling layers. The pre-sampler, strip (first sampling), middle and back samplings are combined as shown in equation 1.1. The results are weighted using empirically determined values chosen to maximise the energy resolution.

$$E_{Total} = W_{global}\left(W_{ps}E_{ps} + E_{str} + E_{mid} + E_{back}\right) \tag{1.1}$$

The energy deposited by electrons in the EM calorimeter is measured combining the data collected from a cluster of 3×7 calorimeter cells in $\eta \times \phi$. The larger size in the ϕ direction accounts for the spreading of EM showers caused by the magnetic field in the ID.

The resolution of electron energy measurements varies with the incident energy of the electron and as a function of η. Figure 1.7 shows these variations for electrons of various energies using plots taken from the ATLAS TDR. The variation of energy resolution in η as shown in figure 1.7 (b) is determined by the mechanical layout of the detector. The resolution around η equals $\sim$ 1.5 is particularly poor. This region is the so-called gap region and corresponds to the interface between the barrel and end-cap calorimeters. Figure 1.8 shows the layout of the ID and EM calorimeter and covers the gap region. The region includes a large amount of dead material in the form of cables, services etc for the ID. The electron energy resolution also varies as a function of the electrons incident energy, as shown in figure 1.7 (a). The resolution follows a $1/\sqrt{E(GeV)}$ distribution with a constant term, as described in equation 1.2.

$$\frac{\sigma}{E} = \sqrt{\frac{a^2}{E} + b^2} \tag{1.2}$$

The first term in equation 1.2 (a^2/E) is determined by the number of samplings (layers of scintillator+absorber) in the calorimeter. This first term varies as a function of η and becomes less important as the incident energy increases. The constant term (b in equation 1.2) is dependant on the position in η and determined primarily by longitudinal leakage and local changes in the calorimeters energy response which have not been accounted for by earlier calibration.

Hadronic Calorimeter

The Hadronic calorimeter is located outside the EM calorimeter in the radial direction. The total depth of the calorimeter is 11λ (radiation lengths) at η equals zero, which includes 1.5λ of uninstrumented support structure. This is sufficient to provide good energy reconstruction of jets entering the calorimeter and to prevent the majority of hadronic activity from passing through the calorimeter and into the muon system.

The hadronic calorimeter extends over the range $|\eta| < 4.9$ and the technology employed varies with η. The range $|\eta| < 1.6$ is covered by an iron-scintillator tile system which consists of plastic scintillator plates embedded in an iron absorber. A LAr system, similar to that used in the EM calorimeter is used over the range $\sim 1.5 < |\eta| < 4.9$. The radiation levels are highest in this region of the detector so the intrinsically radiation hard LAr technology is more appropriate. The LAr system is separated into and end-cap calorimeter which extends to $|\eta| < 3.2$ and a high density forward calorimeter covering the rest of the range to $|\eta| < 4.9$.

The iron-scintillator tile system is further divided into one barrel and two extended barrel segments. Each segment is separated into three radial layers with depths of 1.4λ, 4.0λ and 1.8λ at η equals 0. The tile calorimeter is made up from cells of $\Delta\eta \times \Delta\phi = 0.1 \times 0.1$ in the first two layers and 0.2×0.1 in the last layer and is read out with a total of 10 000 channels. The calorimeter covers the range 2.28m to 4.23m in the radial direction, placing it behind the EM calorimeter which itself has a depth of $\sim 1.2\lambda$.

The hadronic end-cap calorimeters are each separated into two wheels with equal diameter, one positioned further along the z-axis than the other. Both wheels are constructed of copper absorber plates separated by a 8.5mm gap filled with liquid argon scintillator. The inner most wheel uses 25mm thick copper plates whilst the outer uses 50mm plates. The inner wheel is separated into two readout sections along z whilst the outer is read out as one. The total depth of the end-cap is 12λ.

The hadronic calorimeter forward section is placed about 5m from the IP and consists of three layers in z with a total depth of 9λ. This section of the calorimeter is made up of an array of metal rods orientated parallel to the z-axis and embedded in a block of metal. The first layer is constructed from copper whilst the second and third layers are made from tungsten. The thin gap between the rods and the block is 250μm, 375μm and 500μm wide in the first, second and third layers and respectively. The gap is filled with a liquid argon scintillator.

The energy resolution of the hadronic calorimeter varies with energy and as a function of η. Figure 1.9 shows the energy resolution for jets in di-jet events as a function of energy (a) and η (b). The energy resolution in the had calorimeter follows the same shape as that in the EM calorimeter, as in equation 1.2. The energy resolution and the constants a and b are dependent on the cone size with which the jets are reconstructed. Different cone sizes will be optimal for different accelerator luminosities and detector occupancy. The energy of reconstructed jets will also affect the optimal cone size. As can be seen from figure 1.9 (a), the difference in energy resolution between jets reconstructed with different cone size falls with increasing jet energy. This is because jets with higher energy have a larger boost and are generally narrower. These jets suffer less from energy losses from parts of the shower which extend laterally outside of the cone. Figure 1.9 (b) shows how the energy resolution varies with η. The plot indicates that the resolution degrades as η approaches 1.6 and ~ 3 which corresponds with gaps in the hadronic calorimeter listed in table 1.2 (although there are insufficient data points in the plot to draw this conclusion it is supported by further analysis in [2]).

1.3.3 Muon System

The ATLAS muon system is extremely large, accounting for most of the detectors volume. The system comprises of a large number of drift tubes assembled around a set of air-core super-conducting magnetic toroid's. Minimising the amount of material in the muon system by choosing not to use an iron core reduces the degradation of resolution that would normally result from multiple scattering. However, the maximum achievable strength of the magnetic field and therefore its overall bending power is reduced. The large volume of the spectrometer goes some way toward compensating for this.

A summary of the muon systems major components with there extent in η and r is laid out in table 1.3.

component	section	extent in η
spectrometer	barrel	± 1.475
	end-cap	$1.375 < \|\eta\| < 3.2$
Magnets	barrel	$\pm 1.0\eta$
	end-cap	$1.4 < \|\eta\| < 2.7$

Table 1.3: Showing the pseudo-rapidity η range covered by the different parts of the ATLAS muon system.

Muon Spectrometer

The muon spectrometer is made up of a large number of drift tubes. The tubes themselves are 30mm in diameter and constructed from aluminium. They are filled with 93% Ar and 7%CO_2. The drift tubes are mounted in spacer frames which are then fitted to the detectors support structure. The muon chambers are positioned in such a way that any muon passing through the spectrometer should interact with at least three of them.

The relative positions of the large muon chambers in the barrel section are measured by an optical system which provides a precision of $\sim 30\mu m$ for the chambers in an individual tower. Alignment between towers as well as the alignment of the smaller muon chambers outside of the barrel region will be achieved using tracks.

The Muon system also employs Cathode Strip Chambers (CSC), Resistive Plate Chambers (RPC) and Thin Gap Chambers (TGC) for triggering and in the very forward regions of the detector where radioactive flux is very high.

Magnetic Toroid's

The magnetic field in the muon system is responsible for bending the path of incident muons. This allows for measurement of muon momentum through the curvature of their tracks.

The magnetic field is provided by eight super conducting toroid's in the barrel section over the range $|\eta| < 1.0$. The region of the spectrometer in the range $1.4 < |\eta| < 2.7$ the field is provided exclusively by the two smaller end-cap toroid's which are inserted into the ends of the barrel. The region between the barrel and end-cap fields is commonly referred to as the transition region as tracks passing through it are affected by both the barrel and end-cap fields.

1.4 Reconstruction

The data produced by the ATLAS detector can be analysed using a set of software developed by the ATLAS collaboration. This software consists of many different algorithms designed to reconstruct the characteristics of particles that may have passed through the detector. The software goes under the collective name of *Athena* and represents what is considered by the ATLAS collaboration to be the best way to interpret data produced by their detector. A summary of the different particle reconstruction algorithms implemented in Athena is given below.

1.4.1 Electrons and Photons

The reconstruction process for electrons and photons are quite similar. This stems from the fact that it is impossible to separate electrons from photons based on calorimeter information alone. Electrons and photons both deposit energy in exactly the same way through pair production and Bremstralung in the EM calorimeter. As charged particles electrons leave a track in the ID which can be used to separate them from electrons. Within the ATLAS reconstruction software an electron is initially a photon with an associated track.

Electron reconstruction in ATLAS is accomplished by two separate algorithms, one for low P_T and one for high P_T electrons. The high P_T algorithm uses clusters in the EM calorimeter as a starting point and then attempts to find a track that matches the cluster from the inner detector. The track matching is achieved by first finding a track that enters the calorimeter at a similar location to the centre of the electron candidates energy deposit.

The low P_T algorithm is designed to find electrons that have not deposited large amounts of energy in the EM calorimeter. As a result the low P_T algorithm works in the opposite way to the high P_T algorithm, first a track is taken from the inner detector, then an attempt is made to identify a corresponding cluster in the EM calorimeter. The electrons produced by the low P_T algorithm are of little interest in the study of MBH events where very high P_T particles are expected to contain the bulk of the energy produced. Those electrons produced by the low P_T algorithm are also more difficult to interpret than those with high P_T. Electrons from the low P_T algorithm are ignored in this analysis.

1.4.2 Muons

There are a number of competing development teams working within the ATLAS muon reconstruction software and as a result it can be difficult to know which implementation will prove most effective. Broadly, the software can be separated into two different categories, a low P_T algorithm and a high P_T one. High P_T reconstruction involves muons which produce tracks in the muon spectrometer, having passed through the entire inner detector. The low P_T algorithm is limited to reconstructing muons that only leave traces in the inner detector and is mainly involved in identifying muon signals in the hadronic calorimeter.

1.4.3 Jets

These reconstructed objects differ from the photons and muons described above. A jet is not a well defined fundamental object but a collection of different particles that happen to be moving in a similar direction. The number of jets reconstructed in an event is highly dependant on the definition used. ATLAS employs two different algorithms for reconstructing jets and each can be configured in a range of different ways.

The *cone* algorithm is the more conventional of the two. A jet is identified as a stream of particles contained within a cone shaped region of space. The tip of the cone is located at the IP and its size defines the solid angle which it encompasses. The cone algorithm in ATLAS operates with a fixed size cone which is directed toward a cluster in the detectors calorimeter. The direction of the cone is adjusted in the vicinity of the cluster until the energy it contains is maximised. Multiple cones are used to identify jets in a single event, the number of cones is determined by the number of calorimeter clusters present. The default event reconstruction provided by Athena includes two different sets of reconstructed jets produced by the cone algorithm implemented with cone sizes of ΔR[2] equals 0.4 and 0.7, where the later is the size used by default.

The KT topological algorithm functions by growing clusters of associated cells in the calorimeter. Cells are added to a cluster if their energy content shows a small deviation from neighbouring cells that are already in the cluster.

[2]where $\Delta R = \sqrt{\Delta\eta^2 + \Delta\phi^2}$.

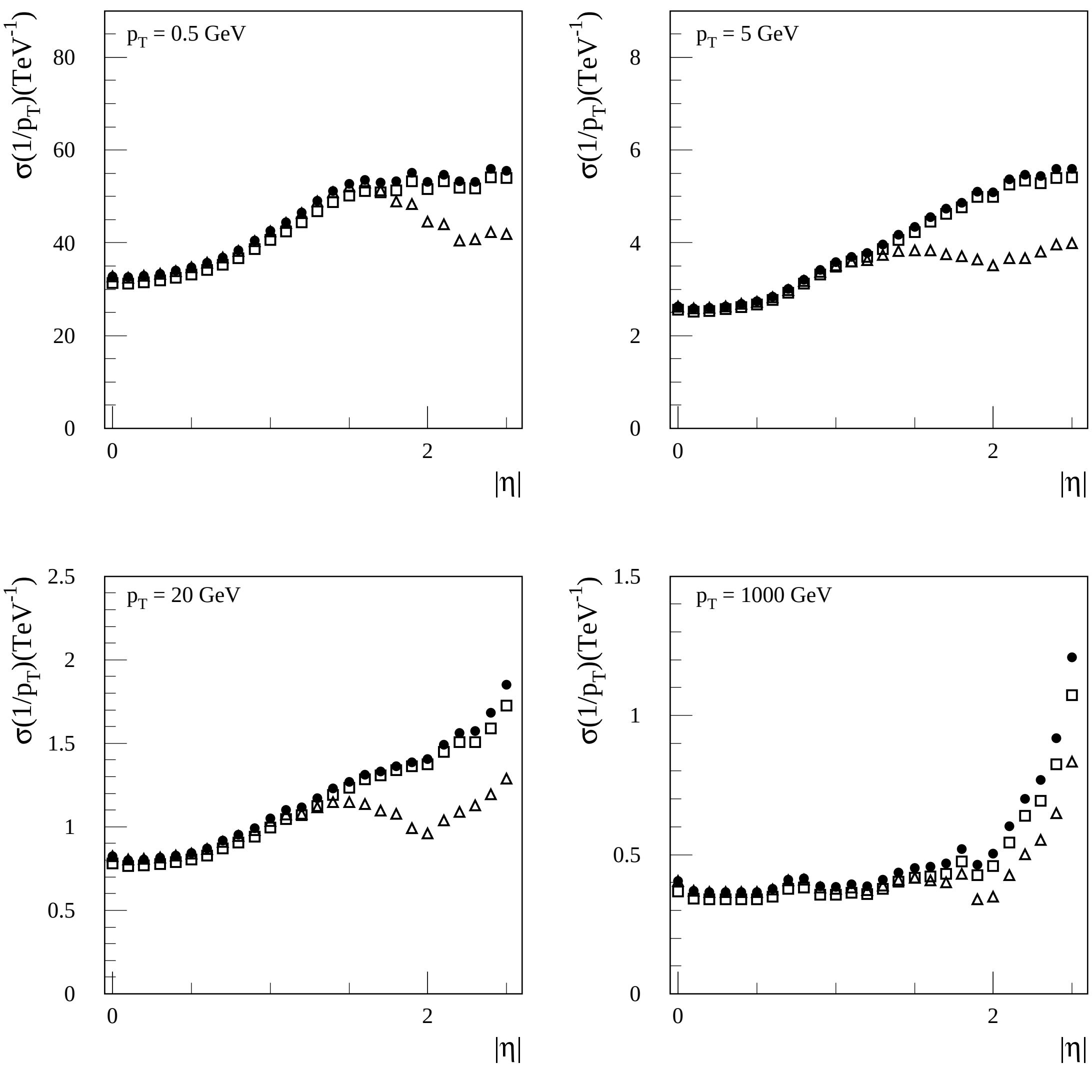

Figure 1.4: Showing the $1/P_T$ resolution of the ATLAS inner detector as a function of η. Each of the plots shows the $1/P_T$ resolution for a sample of single muons with a different energy. The results are shown for a solenoid field with and without a beam constraint in square and circles respectively. The triangles show the results with a uniform field and no beam constraint.

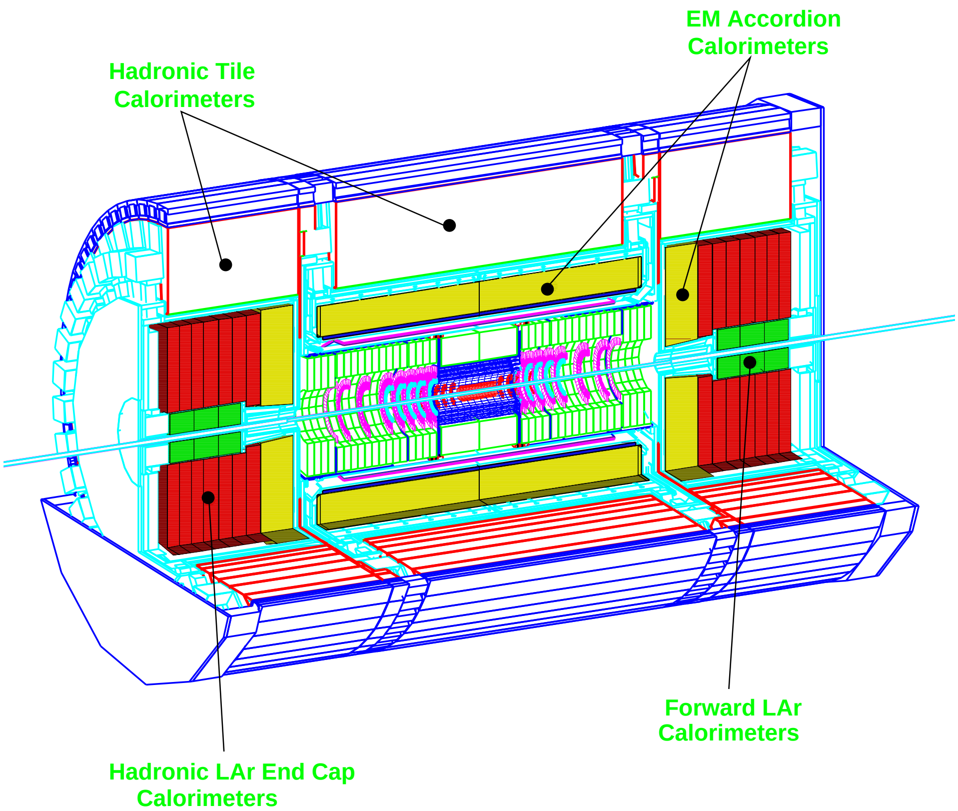

Figure 1.5: Simplified diagram of the ATLAS calorimetry sub-system.

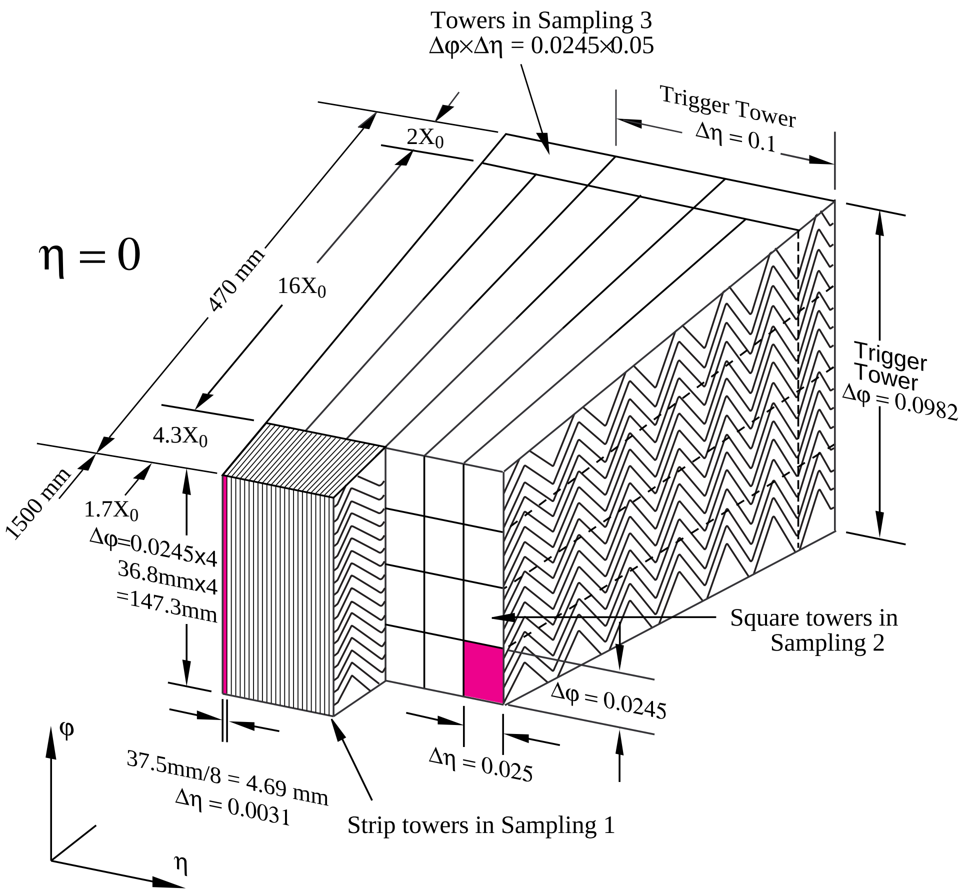

Figure 1.6: Diagram showing the layout of the EM calorimeter barrel section. The accordion geometry of the absorber/scintillator material is show whilst the first, second and third sampling layers are highlighted in red, blue and green respectively.

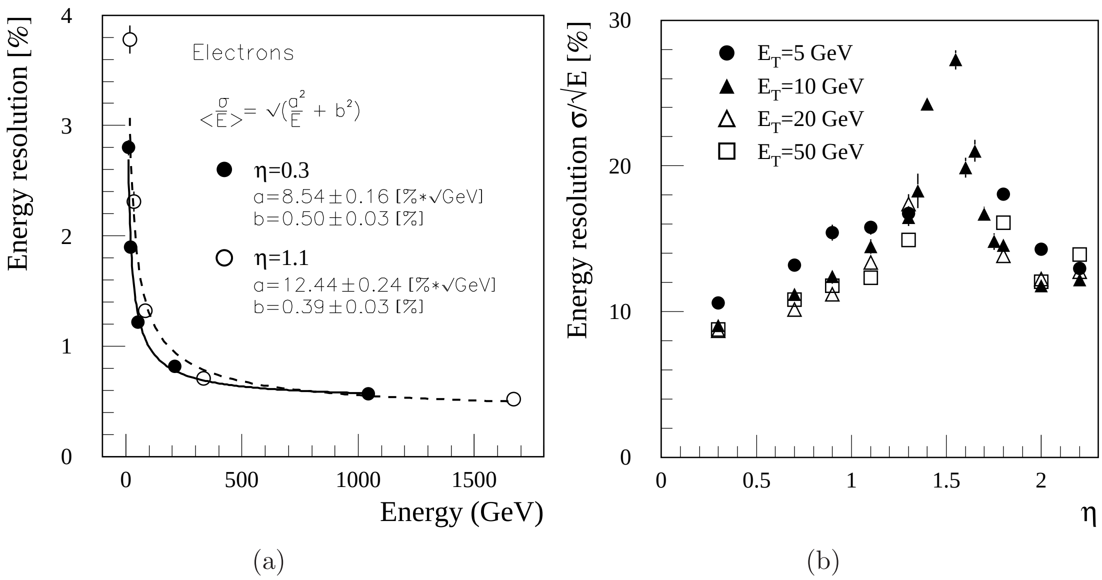

Figure 1.7: Showing the electron energy resolution of the ATLAS EM Calorimeter. (a) shows the energy resolution of electrons at η of 0.3 (solid line) and 1.1 (dashed line) as a function of the incident energy. (b) shows the energy resolution achieved for electrons of various transverse energies as a function of η. Both plots originated from the ATLAS TDR[2].

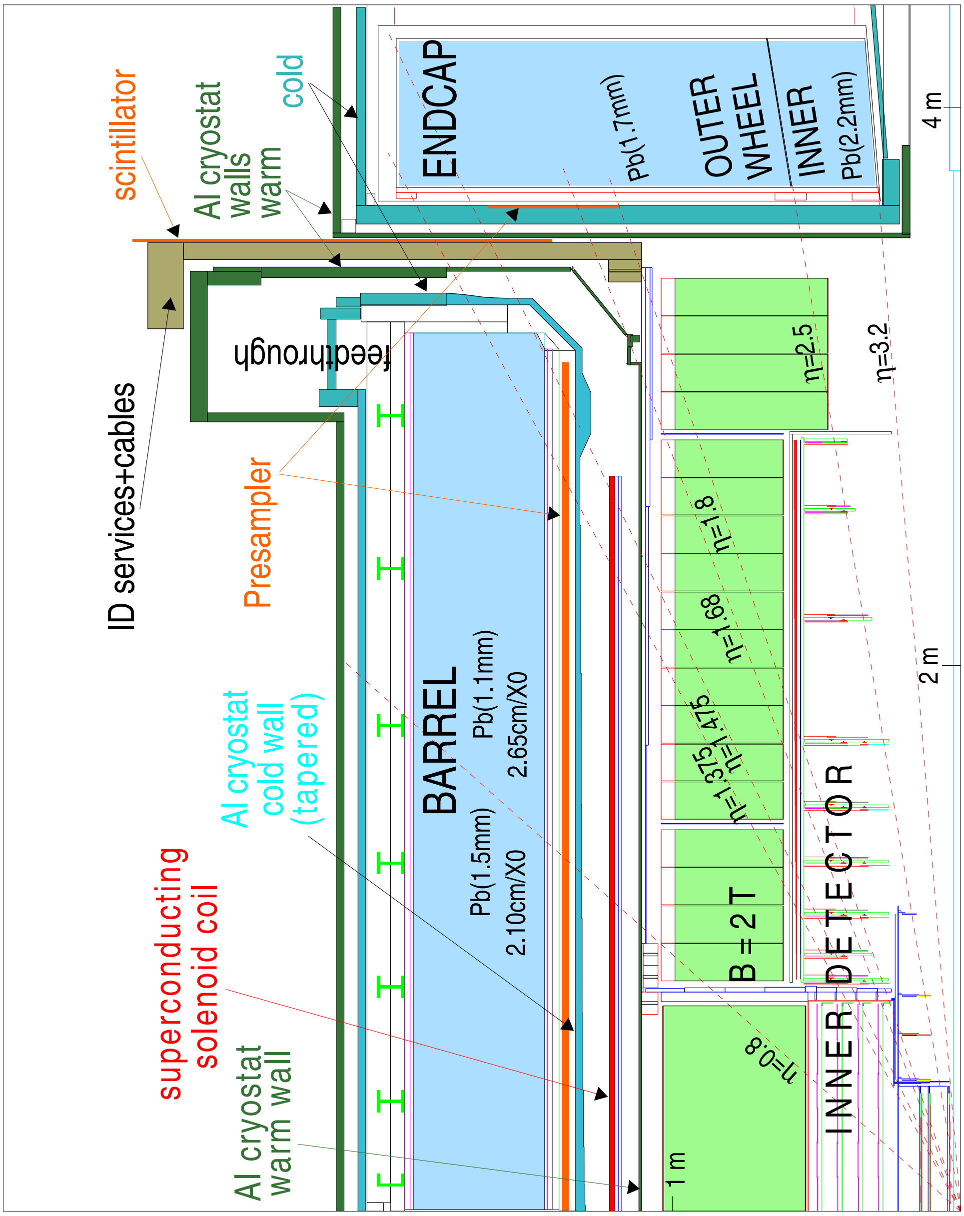

Figure 1.8: Showing a cross section through the ATLAS ID and EM calorimeter. The figure shows one quarter of the detector, with the IP in the bottom left corner of the image. The various sub-detectors are labelled in the figure. Red dashed lines have been used to indicate straight paths projected from the IP at different values of η.

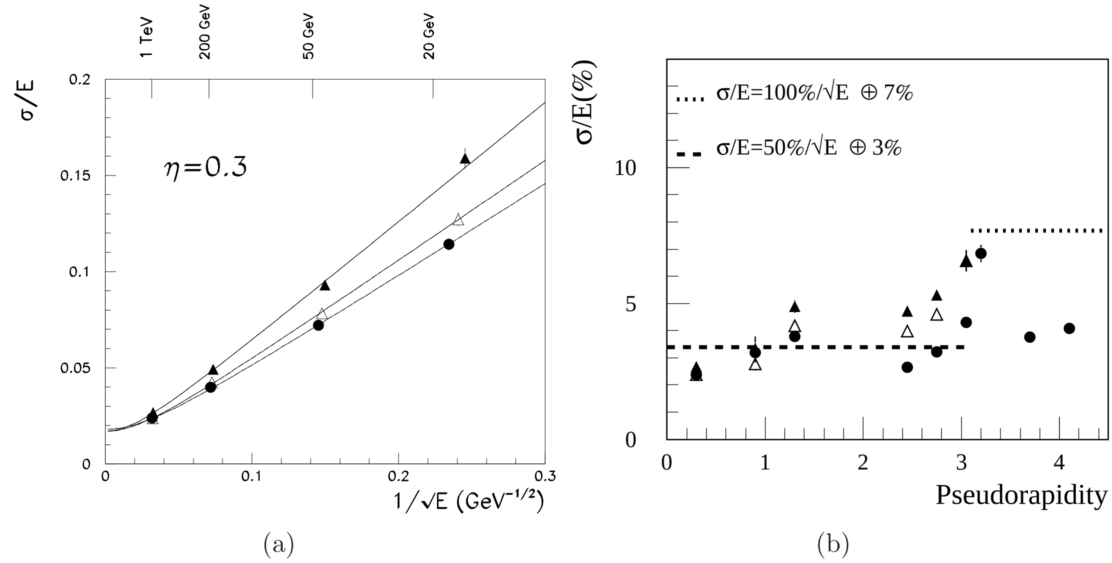

Figure 1.9: Showing the jet energy resolution of the ATLAS Hadronic calorimeter. Plot (a) shows the energy resolution as a fraction for jets at η equals 0.3 as a function of $1/\sqrt{E}$ over an energy range of 20 GeV to 1 TeV. Black circles, open triangles and black triangles represent jets reconstructed with a cone size, ΔR of 1.5, 0.7 and 0.4 respectively. Plot (b) shows the energy resolution as a percentage for jets with an energy of 1 TeV as a function of η. The black circles represent the total energy in the calorimeter. The open and black triangles represent jets with a cone size, ΔR, of 0.7 and 0.4 respectively. The plots shown here were obtained from[2].

Part I

Micro Black Holes

2

Underlying Physics Of Microscopic Black Holes

2.1 Introduction

One of the major obstacles to the complete understanding of particle physics is the difference in scale between the fundamental forces. Gravity is a much weaker force than the strong, weak and electromagnetic forces that are routinely involved in particle physics interactions. This difference in scale is often referred to as the *hierarchy problem*. There are a number of theories that suggest the weakness of gravity may simply be an effective observation and that, fundamentally, gravity is just as strong as the other forces in nature when measured at very small length scales. These theories offer a solution to the hierarchy problem and at the same time introduce a new set of observable phenomenology.

Microscopic Black Holes (MBH) are a potential consequence of strong gravity at short length scales. The production of MBHs at the LHC would present a prominent signal and radically change the current understanding of gravity. This chapter describes the physics involved in the production and evolution of Microscopic Black Holes. The physics described is relevant to MBH events that occur in hadron collider experiments such as ATLAS.

2.2 Gravity and the Standard Model

The driving force behind modern particle physics is a desire to understand the fundamental forces of nature. The SM describes the observations made in experimental particle physics with a small group of theories describing the behaviour of several separate forces. A unified theory of particle physics would combine the forces of nature, presenting a common rule that defines them all. There are four known types of interaction between fundamental particles, these are described by the electromagnetic, strong, weak and gravitational forces. The first three can be described within the framework of Quantum Field Theory (QFT). These forces can be understood using similar mathematical constructs and, most importantly, they can all be studied in experiments at particle colliders. These experiments provide a wealth of experimental data regarding the behaviour of the strong, weak and electromagnetic forces. Gravity is perhaps the least well understood of the fundamental forces and this is largely because it has so far remained beyond the reach of particle physics collider experiments.

The strength of gravity is considerably less than that of the other three fundamental forces. As an example, the gravitational force between two protons is approximately 36 orders of magnitude weaker than the electromagnetic force between the same particles. The field describing each of the fundamental forces has an associated mass scale which is inversely proportional to its coupling strength. The scale associated with the electromagnetic, weak and strong forces is below 1 TeV whilst the scale of gravity is the Planck Mass (M_{pl}) which is approximately 10^{16} TeV[4].

The difference between the forces is so vast that it makes the eventual unification of gravity with the the other forces extremely unlikely using the current model. A new model of gravity would be required to solve this hierarchy problem and make the unification of all the SM forces possible.

The relative weakness of gravity means that even if its effects were apparent in particle physics experiments they would be difficult to observe in an environment dominated by the other forces. A number of dedicated experiments have been undertaken to examine the behaviour of gravity at length scales on the order of 1 mm[7] but weakness of gravity has prevented further measurement. Nothing is really known about gravity below the macroscopic scale.

The effects of gravity are best described by Einstein's General Theory of Relativity (GR). However, the assumptions behind GR are not valid on the relatively small length scales or energies involved in particle physics. According to current convention GR should have an ultra-violet cut off beyond which it is no longer a useful model of gravity. At some energy scale GR should be replaced by a quantum theory of gravity. Although such a theory is currently unavailable it is reasonable to assume that GR cannot be applied to systems with energy below some value, usually taken to be on the order of a few M_{pl}. This means that GR cannot be used to explain gravitational interactions in systems with mass (or energy) less than M_{pl}. The value of M_{pl} is derived from the strength of gravity, described by Newtons constant G, as shown in equation 2.1.

$$G_{Newton} = \frac{1}{M_{pl}^2} \tag{2.1}$$

The value of M_{pl} produced by equation 2.1 is somewhere in the region of 10^{19} GeV, which is well in excess of the energies currently available to particle physics. Even the full 14 TeV CoM energy of the LHC is ~ 15 orders of magnitude below the Planck scale. Therefore the low energy limit of GR is beyond the reach of any current or feasible future collider based particle physics experiments. A stronger gravity would lead to a smaller Planck Mass and an extension to the range of energies over which GR is applicable.

There are currently many theories which suggest that the behaviour of gravity may change at short length scales, potentially becoming much stronger than it appears to be at the length scales which have been observed so far. These theories involve adding extra spatial dimensions to modern physics and exist in several different incarnations.

2.3 Models of Extra Dimensions

Particle physics is firmly rooted in a four dimensional space-time, as described by Einstein's General Relativity. There is however, no known fundamental reason why this should be so. Theories which include more than four dimensions are often able to provide new solutions to problems in modern physics.

In the 1920s, Kaluza and Klein developed one of the first extra dimensional theories with the aim of unifying GR with electromagnetism. They found that it was possible to write down Einstein's GR and Maxwell's equations in the same tensor equation, provided that it had 4 spatial dimensions. The additional dimension was closed in on itself or *compactified* with a cylindrical shape. This allowed the extra dimension to remain flat (no intrinsic curvature) but with the property that a translation of $n2\pi r_c$, where n is an integer and r_c is the radius of compactification, would always map onto the same position in the extra dimension. This new degree of freedom (motion in the extra dimension) had the same properties as the $U(1)$ gauge symmetry responsible for much of the behaviour of electromagnetism.

Kaluza and Klein's theory allowed all particles to propagate in the extra dimension, introducing a new kind of phenomenology. Firstly, as the extra dimension is closed, any momentum orthogonal to the normal three spatial dimensions must be quantised. The behaviour is similar to the quantisation of available energy states for particles trapped in a potential well. Secondly, a particle with momentum in the direction of the extra dimension will appear to have an additional mass when measured by a four dimensional observer. This is most easily explained by equation 2.2 where P_x is momentum in three spatial dimensions, P_n is momentum in the extra dimension and m is the mass as observed in three spatial dimensions.

$$\begin{aligned} E^2 &= P_x^2 + P_n^2 \\ &= P_x^2 + m^2 \end{aligned} \tag{2.2}$$

The mechanism of generating an additional mass through momentum in an extra dimension leads to the possibility that a mass-less particle can appear massive. Further more, the additional mass is quantised. This means that a single particle can appear as a spectrum of particles with different masses. This phenomenon is referred to as a Kaluza Klein (KK) tower of particles and is a feature of many models which involve extra dimensions.

Kaluza and Klein's theory has been ruled out as a method for unification. The model is not able to incorporate the modern quantum mechanical description of electromagnetism or the existence of the weak and strong force. More importantly the possible existence of extra dimensions has been studied using data from particle physics experiments. The existence of extra dimensions would modify the behaviour of all the fundamental particles which propagate in them. The accuracy of standard model predictions of precision particle physics results places severe limits on the allowed size of any extra spatial dimensions. Extra dimensions that affect the behaviour of SM particles may not have a radius of curvature greater than $\sim 10^{-3}$ fm, which is equivalent to an energy scale of $\sim$ TeV^{-1}.

Theories of extra dimensions are by no means excluded from modern physics. Extra dimensions are essential for string theory, which typically requires either 11 or 26 dimensions in order to be self consistent. However, string theory allows these extra dimensions to be compactified to such an extent that they no longer have any influence on observable particle physics below some large energy scale. These small extra dimensions have no bearing on the observable physics of microscopic black holes in particle collider experiments.

2.3.1 ADD type models

In 1998, Arkani-Hamed, Dimopoulos and Dvali (ADD) proposed a new explanation of the hierarchy problem[5]. They proposed that the only scale in physics was the electroweak scale, M_{EW}. The observed weakness of gravity is explained by the existence of two or more extra dimensions throughout which gravity may propagate. The extra dimensions are closed in on themselves. This means that at short length scales gravity follows a $1/r^{2+n}$ law whilst at larger length scales it follows the more familiar $1/r^2$ law.

Allowing only gravity to propagate in the proposed extra dimensions enables ADD type theories to largely ignore the limits placed on the size of extra dimensions by precision particle physics measurements. The standard model particles are restricted to a four dimensional hyper-surface that is embedded within the higher dimensional space. This hyper-surface is usually referred to as a *brane* (from the word membrane) whilst the full extent of the extra dimensional space is labelled the *bulk*. Models of this type have the interesting property that the difference between the strength of gravity and that of the other fundamental forces can be related to the difference in the volumes of space accessible to the different fields.

The extra dimensions described in ADD are closed, as they are in the KK model described above. At length scales greater than the radius of the extra dimensions gravity behaves as it would in four dimensional GR. However, at length scales smaller than the radius of the extra dimensions it is able to propagate freely in what is essentially an n-dimensional flat minkowski space-time.

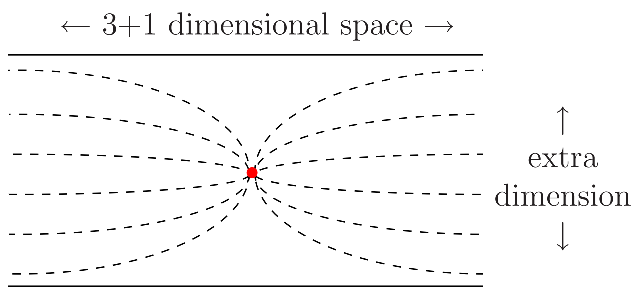

Figure 2.1: A simple diagram illustrating gravities dependence on length scale in the ADD model with a single extra dimension. At short length scales, close to the gravitational point source at the centre of the diagram, the field lines point in all directions so the force of gravity falls off as $1/r^3$. At larger length scales away from the point source the field lines are constrained to the flat 3+1 dimensional space so the force of gravity falls off as $1/r^2$. This means that gravity can be stronger than currently thought but loose a large part of its strength over a distance which is smaller than the size of the extra dimension.

When propagating in three spatial dimensions gravitational flux diverges through the two dimensional surface of a three dimensional sphere, giving rise to the inverse square law. When propagating in n spatial dimensions gravitational flux diverges through the n-1 dimensional surface of an n dimensional sphere, leading to a $1/r^{n-1}$ dependence between the strength of gravity and the distance r from the source. This means that if gravity does have access to extra dimensions of this type then its strength would fall off much more quickly at short length scales than it does at large length scales. Figure 2.1 is a simple cartoon designed to illustrate this point. Behaviour of this kind would allow the fundamental strength of gravity to be much larger than currently thought. Gravity's real strength would only be apparent at very short length scales, smaller than the radius of the extra dimensions. Adjusting the size and number of extra dimensions in the theory allows variation in the fundamental scale of gravity whilst still reproducing the observed 4-dimensional scale of M_{pl}.

The relationship between the fundamental Planck Mass, M_*, as observed in the bulk and the volume of the extra dimensions r^n is described in equation 2.3. This equation assumes that each of the extra space-like dimensions has the same radius r.

$$M_{pl}^2 = M_*^{2+n} r^n \tag{2.3}$$

The model proposed by ADD suggests that the fundamental scale of gravity is the same as the electroweak scale, $\sim 1\ TeV$. ADD belongs to the Large Extra Dimension (LED) class of models. LED models involve a linear relationship between the difference in the observed and fundamental Planck mass and the volume of the extra dimensional space. Using equation 2.3 it is possible to show that a value of M_{pl}^* of 1 TeV in a theory with one extra dimension would require the extra dimensional radius, r to be $\sim 5 \times 10^{14}$m which is on the same scale as an astronomical unit. This is obviously unrealistic and would be ruled out by observations of the motion of planets in the solar system. There are a number of sources that place limits on the maximum size of the extra dimensions in LED models. Requiring two extra dimensions reduces the required size of r to ~ 2 mm for a fundamental Planck Mass of $\sim$ TeV, which was within the limits set by direct measurements of gravity at short length scales at the time the ADD theory was put forward. However, more recent torsion-balance experiments have shown that the inverse square law holds down to lengths of ~ 0.05mm[7]. This new limit means that the number of extra dimensions must be greater than two if the fundamental Planck mass is to remain at the electroweak scale. There are also other more stringent limits on ADD type models derived from astrophysical measurements. A short summary of some of these limits is presented in table 2.1.

The ADD model gives rise to a tower of KK graviton states, each with a different mass. As the other standard model particles are restricted to a brane they cannot be excited in this way. The extra dimensions in ADD models are large and so analogous to a wide potential well. This means that the spacing between the allowed values of momenta in the extra dimensions is small. When the effects of detector resolution are considered it becomes clear that identifying the masses of individual graviton states in ADD models would most likely be impossible. This leads to an observable continuum of graviton mass states.

Momentum must be conserved in these extra dimensions as it would be in any 4-dimensional description of space-time. Gravitons with extra dimensional momentum are still coupled to the other SM fields which remain restricted to the four dimensional brane. As a result gravitons can exchange momentum with these fields and, through them, with the brane to which they are bound. This means that in ADD models it is possible to produce single and virtual gravitons and still conserve momentum.

Searches for ADD type models of extra dimensions have been performed at collider experiments in the past and the potential application to data from the ATLAS detector has been considered. These studies often concentrate on direct or indirect searches for a spectrum of KK gravitons[9].

2.3.2 Randall-Sundrum Type Extra Dimension Models

Warped extra dimension models are typified by the Randall-Sundrum type I scenario[10]. This model involves a single extra spatial dimension which is not closed on itself but is bounded by two 3+1[1] dimensional branes. The extra dimension is not flat as it was in the ADD model discussed above, instead the geometry is that of a five dimensional an anti-de sitter space[2]. The four dimensions of observable space-time are described by an approximately flat minkowski metric at any point in the five dimensional space. However, this metric is scaled by a *warp factor* which is exponentially dependent on its position in the extra dimension. This means that length scales, and therefore energy scales[3] change as a four dimensional observer moves through the fifth, extra dimension. The RS model demands that the Standard Model particles are constrained to one of the two branes that bound the extra dimension. This brane is called the *TeV brane*. Gravity is strongly attracted to the other brane, known as the *Planck brane*, but gravitons are able to propagate throughout the extra dimension. The energy scale of gravity is the same as that of the SM fields, being on the order of a TeV. However, this energy scale only applies at the position in the extra dimension where the field is localised. The change in length and energy scales that occurs when moving across the extra dimension means that the mass scale of gravity appears very large (and the strength of gravity correspondingly small) when measured on the TeV brane. Figure 2.2 shows a simple cartoon designed to

[1] Three spatial dimensions and one time dimension

[2] Ads_5 exhibits an overall negative curvature. It is similar to a de Sitter space in that it is a solution to Einstein's equations but with a negative cosmological constant.

[3] as length is inversely proportional to energy

illustrate this model.

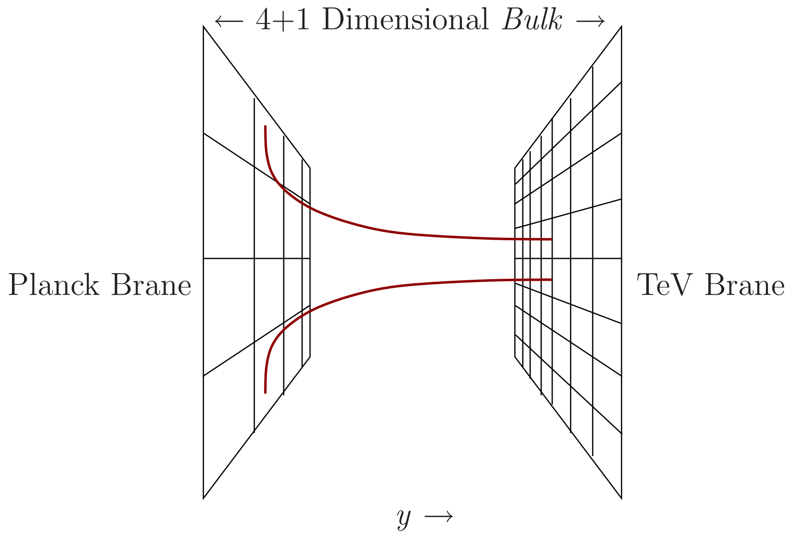

Figure 2.2: Showing a simple cartoon illustrating the configuration of the extra dimension in a Randall-Sundrum type I model. The TeV brane is shown on the right whilst the Planck brane is shown on the left. Length scales become exponentially larger and therefore energies become correspondingly smaller as a function of position in the extra dimensional bulk, as illustrated by the red lines in the diagram.

The difference in scale between gravity and the other standard model forces is exponentially dependent on the size of the extra dimensions. The separation between the two branes in the RS type I model can be relatively small and still generate the large scale differences observed by experiment. The RS model requires a separation between branes of approximately 50 Plank Lengths to generate the observed hierarchy. This compares favourably with the factor of $(M_{pl}/TeV)^{2/n}$, something like $\sim 10^6$ for two extra dimensions, required by large extra dimension models such as ADD[10]. This feature alone makes Randall-Sundrum type models attractive as an explanation of the hierarchy problem. In comparison, the ADD models simply reformulate the problem from one of differences in the strength of forces to one of explaining the large size of extra dimensions in which only gravity may propagate.

The five dimensional line element describing the metric of a Randall Sundrum model is expressed in equation 2.4, where y is the coordinate in the direction of the extra dimension and k is a constant which embodies the warp factor. This representation places the Plank brane at $y = 0$ and the TeV brane at $y = \pi$.

$$ds^2 = e^{-k\pi y}\eta_{\mu\nu}dx^\mu dx^\nu + dy^2 \tag{2.4}$$

The warp factor, k, changes length and energy scales as an observer moves through the extra dimension. RS models are often characterised by the parameter k/M_{pl} as this ratio determines difference between the fundamental and observed scale of gravity.

Randall-Sundrum models also allow for a single particle with extra dimensional momentum to appear as a new particle with an additional mass, in a similar fashion to the KK towers of particles resulting from models with closed extra dimensions. The two branes at the extremities of the extra dimensional space provide appropriate boundary conditions for this to happen. The size of the extra dimensions in these models is small when compared to those employed in the ADD type models discussed earlier. As a result the spacing between the allowed momenta in the extra dimensions is large. This results in a large separation between the observable mass states of particles with extra dimensional momentum. Randall-Sundrum type models allow for the observation of individual mass peaks resulting from the separate excitations of gravitons in the model.

Type II Randall Sundrum models differ from type I in that the second, brane has been moved an infinite distance away from the first brane in the extra dimension. Type II models effectively have one brane.

Table 2.1 shows some of the limits placed on models of extra dimensions by table top, astronomical and particle physics experiments. The torsion balance experiment[7] highlighted represents the current best limit produced by table top experiments on the allowed size of the extra dimensions. The strongest limits on ADD models come from astrophysics where the presence of KK modes of particles can have an observable affect on super-nova[8]. Recent searches at the Tevatron[11] have resulted in stringent limits on the mass of the RS graviton.

Experimental Measurement	**Limits**
Deviations from Newtons Law	
Torsion-balance experiment[7]	inverse square law holds to 0.56μm
ADD type models	
Decay of KK gravitons from super-nova[8]	$M_* \gtrsim 500$ TeV (n=2)
Excessive heating of super-nova by KK decays[8]	$M_* \gtrsim 1700$ TeV (n=2)
Randall-Sundrum Type models	
Search for New Physics in Di-Electron Events[11]	$M_G < 889\ GeV$ for $k/M_{pl} = 0.1$

Table 2.1: Summary of some of the limits placed on models that include extra dimensions. The table includes limits on the allowed size of the extra dimensions, the fundamental Planck Mass M_* and the mass of the RS graviton M_G.

2.4 Microscopic Black Holes

The existence of astronomical Black Holes with masses many times that of the sun is an accepted result of Einstein's General Relativity. Indirect evidence for the existence of astronomical black holes is available from astronomy.

As discussed above, GR does not describe the behaviour of gravity in interactions with energy less than the Planck Mass, M_{pl}. In 3+1 dimensions the value of M_{pl} is $\sim 10^{19}$GeV. This means that under the currently accepted model of physics the behaviour of gravity in a particle collider is not governed by GR. Even if this restriction did not exist and GR extended to cover all energies the cross section for MBH production would be suppressed by M_{pl}^4, making it vanishingly small. However, if gravity is in fact much stronger than currently thought and this hidden strength is revealed in the exploration of very short length scales then the production of MBH will become a possibility.

MBH are not so much a new physical model as they are a potential symptom of strongly coupled gravity at short length scales. The underlying mechanism behind the strong gravity may affect the cross section for the formation of MBH and the properties of any extra spatial dimensions could well affect their behaviour and decay.

2.4.1 The Nature of Black Holes

A Black Hole is often defined as an object for which the gravitational escape velocity is greater than the speed of light. The possible existence of such objects was suggested before the conception of Einstein's Theory of Relativity. Newtonian gravity along with a finite speed of light allows for an object that is so massive that light cannot escape its surface. Such an object is called a Dark Star.

Under General Relativity the definition of a black hole is similar but the mathematical description is quite different. General Relativity describes gravity not as a force but as a distortion of four dimensional space-time. Every object not under the influence of any external force moves along a straight line in this four dimensional space-time with a total speed equal to the speed of light. As the three spatial components of an objects velocity increase so the component in the time dimension must decrease. The paths followed by objects with constant momentum through space-time are called geodesics. These paths can be calculated using Einstein's equations.

Any spherically symmetric distribution of mass can be described as a gravitational point source from any position outside of the distribution. There will be a spherical surface surrounding that point source upon which the curvature of space-time is so great that light cannot escape. This surface is also spherically symmetric and its radius is described by the Schwarzschild equation which is shown as equation 2.5 below.

$$R_s = \frac{2GM}{c^2} \equiv \frac{2M}{M_{pl}^2} \tag{2.5}$$

Light will only become trapped by a mass distribution like the one described above if the physical radius of that distribution is smaller than its Schwarzschild radius. Typically a black hole will form if a large amount of matter or energy is compressed into a small volume. More specifically a Schwarzschild black hole will be formed if any amount of spherically symmetric non-rotating uncharged matter or energy is compressed into a volume with a radius smaller than its Schwarzschild radius. The Schwarzschild black hole represents the simplest type of black hole. More complex black hole solutions exist to the equations of GR which can be applied to different sets of initial conditions.

The equivalence principle states that the effects of gravity and acceleration are completely indistinguishable for an inertial observer. As far as black holes are concerned, this means that if a rotating body forms a black hole the shape of its event horizon will be different to that of a non-rotating black hole. The properties of a rotating black hole are described by the Kerr solution to the equations of GR. These include a distortion of the event horizon from the spherical symmetry of the Schwarzschild solution and the addition of a new region in which test particles may be accelerated by coupling to the angular momentum of the black hole. This new region is called an ergo-sphere due to its capacity to do work. Electric charge will also effect the shape and behaviour of a black hole. Black Holes carrying electric charge are modelled by the Neumann solution to the equations of GR.

The formation of microscopic black holes from two partons (see below) would lead to the possibility of producing a black hole with a non-zero colour charge. This is something which hasn't been considered in the literature to any great degree and the behaviour of colour charged black holes is not well understood. This places an additional uncertainty on MBH physics.

2.4.2 Black Hole Formation in a Particle Collider

A Black Hole will form if enough matter or energy is forced into a small enough volume. This is precisely what Particle colliders such as the LHC are designed to do. When two protons collide large amounts of energy are focused into a very small region of space. A naive analysis would show that a microscopic black hole would be formed if two partons interacted with one another with an impact parameter (distance of closest approach) less than twice the Schwarzschild radius as calculated from the collisions centre of mass energy.

The cross section for MBH production would then simply be the cross section of the event horizon of a black hole with mass equal to the centre of mass energy of the collision. This is shown by equation 2.6 below.

$$\sigma_{mbh} = \pi r_s^2 \tag{2.6}$$

However, equation 2.5 showed that the Schwarzschild radius is inversely proportional to the Planck Mass squared. This means that the cross section for MBH production is suppressed by an order of the Planck-mass to the power of four, as seen in equation 2.7 below.

$$\sigma_{mbh} = \frac{4\pi M^2}{M_{pl}^4} \tag{2.7}$$

This suppression means that MBH production is essentially ruled out under unmodified GR. However, if the value of M_{pl} is closer to a TeV as suggested by some theories of extra dimensions, including those discussed above, then the suppression is greatly reduced and the cross section for MBH production becomes important.

The cross section calculation above is rooted entirely in classical GR. Without the kind of reduction in the value of M_{pl} afforded by the extra dimensional theories discussed above any interaction at the LHC would be well below the classical cut off for gravity and governed entirely by an unknown theory of quantum gravity.

The cross section for MBH production increases with the CoM energy of collisions. From equation 2.7 it can be seen that σ_{mbh} is proportional to the CoM energy squared. This behaviour is quite unlike most processes in particle physics whose cross sections fall with energy and provides a possible means of identifying MBH events after correcting for PDFs. MBH production, if found to be a possibility at the LHC, would become more prevalent with energy and may effectively censor higher energy particle interactions from future experiments.

2.4.3 Hawking Radiation

The emission of Hawking radiation[12] is the mechanism by which Black Holes are expected to decay. The derivation of Hawking Radiation is based on propagating a quantum mechanical wave equation in the vicinity of a collapsing body which must eventually form a Black Hole. The result is that Black Holes emit radiation in the form of fundamental particles and gravitational waves during their formation and continue to do so for the rest of their existence. Hawking states that the former was expected but the later was not. The continual emission of radiation is the phenomenon usually called Hawking radiation.

The Hawking Temperature of a Black Hole characterises the energy spectrum of the particles which it emits. A direct analogy is drawn between the behaviour of Black Holes and the laws of thermodynamics. A Black Hole acts like a perfect black body radiator (with some modification, discussed later) with a Hawking Temperature which is inversely proportional to its mass. Equation 2.8 contains the expression for the Hawking Temperature of a Schwarzschild Black Hole as a function of its mass.

$$T_H = \frac{\hbar c^3}{8\pi G M k_B} \tag{2.8}$$

Where c is the speed of light, G Newtons gravitational constant, M the mass of the Black Hole and k_B is Boltzmann's constant.

The calculation of Hawking Temperature presented in equation 2.8 assumes a universe with three spatial dimensions. The energy of collisions at the LHC will never be sufficient to form Black Holes in three spatial dimensions so it must be assumed that any MBH that are observed will be embedded in more than three dimensions. Equation 2.8 is a more general formulation of the Hawking Temperature calculation which applies to a Schwarzschild Black Hole in any number of dimensions. The dependence on the number of extra dimensions n leads to Black Holes getting hotter as the the number of dimensions increases. As the Hawking Temperature of a Black Hole increases the particles that it emits become fewer and harder.

$$T_H = \frac{1+n}{4\pi R_{BH}} \equiv \frac{1+n}{M_{BH}^{1/1+n}} \tag{2.9}$$

Where M_{BH} is the mass of the Black Hole, R_{BH} its radius and n the total number of dimensions.

The emission spectrum of a MBH are influenced by properties other than its Hawking Temperature. The electric charge of a Black Hole will influence the emission of electrically charged particles, leading to a bias towards those particles with the same sign as the MBH. The angular momentum of a Black Hole will affect the type of particle emitted, leading to an increased number of particles with large spin which would have an especially large impact on the number of gravitons produced by the decaying Black Hole. There will also be an effect on the emission spectrum from the coupling between the spin of a potentially emitted particle and the gravitational field of the Black Hole itself. These properties which effect the Black Hole emission spectra are collectively referred to as *Grey Body Factors*[17]. When these factors are taken into account, and the subsequent decay of unstable emitted particles is considered ratio of hadronic to leptonic active expected from the decay of an MBH is approximately 5:1. The energy and flavour spectrum of particles emitted during MBH decay is discussed in more detail in chapter 5.

The lifetime of MBH events is dependant on the environment in which they are formed. Under an ADD scenario the lifetime of an MBH produced at the LHC would typically be 10^{-26} seconds[15]. MBH produced in RS models can potentially have lifetimes anywhere between that of the ADD variety and 10^{9} seconds[13], with the value being inversely dependant on the thickness of the brane. Such meta-stable MBHs would appear as missing energy or heavy charged particles in a detector. The subject of stable MBH signals is not considered in this work.

The derivation of Hawking radiation relies on the forming Black Holes event horizon becoming an infinite future horizon. That means that all geodesics must have pass through the horizon in the infinite future. This assumes that the Black Hole will exist into the infinite future, which is not a good assumption when considering microscopic Black Holes with a potential lifetime of 10^{-26} seconds. The gravitational collapse of the Black Hole assumed in Hawking derivation must be quasi-static. Microscopic Black Hole formation in a particle collider will not conform with this assumption either. MBH formation at the LHC will likely be a violent affair producing MBH with very large angular momentum and complex multi-pole moments in the event horizon.

Although Hawking Radiation is an established part of theoretical physics, it has never actually been observed experimentally. This is considered reasonable as Black Holes with a high mass have a correspondingly low temperature and remain stable as they can accrue matter faster than they lose energy through radiation. Super massive, low temperature Black Holes emit very low energy radiation which can not be observed. Low mass Black Holes with a high temperature and potentially observable emissions are unstable and therefore not prevalent in the universe.

However, if MBH formation is possible at the LHC then it is also possible in cosmic ray interactions with the atmosphere. Strict limits can be placed on the behaviour of these MBH simply by estimating the number which would be trapped in the centre of a planet such as Jupiter after a period of continued exposure to cosmic rays. It seems that if MBH are produced then they must decay or disappear in some way.

2.5 Summary

The underlying physics of Microscopic Black Holes centres around GR, Hawking Radiation and an increase in the observed strength of gravity at short length scales. There are a number of theories which suggest that the true strength of gravity could be hidden from observation because the force is able to propagate in one or more extra spatial dimensions. These extra dimensions must be small, on the order of ~ 0.05 mm or smaller. According to these models, the full strength of gravity should become apparent when interactions governed by gravity are observed at length scales smaller than the size of the extra dimensions. These extra dimensions remain closed to SM particles so their existence is not constrained by precision particle physics measurements. An increase in the strength of gravity would lead to a rescaling of the Planck Mass and a corresponding increase in the MBH production cross section. Without this increase in the strength of gravity and corresponding decrease in the fundamental Planck mass MBH production would not occur at the LHC.

MBH have an extremely short lifetime and decay effectively instantaneously in the ATLAS detector. The process of Hawking radiation is responsible for the decomposition through the emission of a broad spectrum of particles. Through the theory behind Hawking Radiation, a MBH can be modelled as an approximate black body emitter with a temperature that is inversely proportional to its mass. The decay of a MBH leads to an isotropic distribution of particles of all types with even probability. Those MBH likely to be produced at the LHC will emit particles with energies which follow an approximate black body spectrum with a peak at 500 GeV and ranging up to several TeV.

The cross section for MBH will increase with CoM energy until, eventually MBH production could become the dominant process in particle interactions. This scenario could lead to an eventual censorship of high energy physics processes behind the event horizons of MBHs.

3

Monte Carlo Event Generation

3.1 Introduction

Making the connection between observations made in particle physics experiments and the underlying physics which lead to those observations is difficult. Particle physicists rely heavily on computer simulation of the underlying physics during this processes. Monte-carlo simulations provide a controlled environment which can replicate the behaviour of a particle detector in response to a know physics process. A typical analysis will compare the distributions found in real physics data with those generated by a computer simulation of a certain physics process. Arguments can then be made as to whether or not that simulated process is occurring in the real physics data.

All of the simulation work carried out during this analysis involved the ATLAS software framework Athena. Athena version 11.0.42 was used for all results produced using the ATLAS full simulation. Results produced from the ATLFAST simulation made use of Athena version 10.0.0.

3.2 Standard Model Event Generator

The HERWIG event generator [14] is a monte-carlo program for simulating particle physics processes. Herwig can be used to generate a large number of different Standard Model (SM) physics processes as well as a number of Supersymetry (SUSY) and other exotic processes. The program is then able to take the fundamental particles produced by these physics processes and calculate there behaviour as they pass through time and space. These calculations include the processes of Quantum ChromoDynamics (QCD) that allow fundamental quarks and gluons to form measons and baryons, usually called hadronization.

There are, of course, a large number of new and exotic particle physics processes which Herwig is unable to simulate. In order to accommodate such processes Herwig is able to accept a collection of fundamental particles as input from an external program and then process those particles in the same way as it would handle particles produced by one of its internal physics processes. The specification for this interface was determined by the Les Houches accord and a very similar mechanism to the one used in Herwig has been implemented in other particle physics monte-carlo programs.

The Herwig program has been used to hadronise the fundamental particles produced by the different event generators employed during this analysis. The version of Herwig used was incorporated into the ATLAS software framework, Athena. Herwig version 6.507 was used during this analyses.

3.3 Micro Black Hole Event Generation

Micro Black Hole events can be simulated using a monte-carlo program. There are several of these available at the moment. The program used during these studies is called Charybdis [15]. Version 1.0 of Charybdis was used in all the results presented in this work.

The Charybdis monte-carlo program uses the ADD model of extra dimensions discussed above. The limits placed on this model, largely by astronomical data mean that if it is real the value of M_{pl} must be at least on the order of $\sim 1000TeV$. This limit places ADD MBH well beyond the reach of the LHC. However, MBH produced by ADD models might not behave very differently from those produced by other models of extra dimensions. The simulated MBH produced by Charybdis still serve as a useful model of MBH behaviour and decay at the LHC and as such are extremely useful in any study of MBH physics.

The Charybdis monte-carlo produces a list of particles produced directly by a simulated MBH via Hawking Radiation. These particles must then undergo hadronization and subsequent decays which are not handled by Charybdis. Instead a separate monte-carlo program must be used. Charybdis has been written to take advantage of the Les Houches Accord which defines a standard protocol for communication between monte-carlo programs. As a result either Herwig or Pythia can be used to perform secondary decays and hadronization on the output of Charybdis. The Herwig monte-carlo program was used for all such calculations performed in this analysis.

The decision to use Herwig was driven entirely by the problems encountered when interfacing the Charybdis+Pythia combination with the ATLAS software framework (Athena). The Charybdis+Pythia combination proved extremely unstable within Athena, despite the fact that it ran without error outside of Athena.

Charybdis Configuration Options

The Charybdis program offers a number of configuration options which can be used to control the generation of each MBH event. These options are outlined bellow.

Plank Mass The value of M_{pl} in the ADD model used by Charybdis. The value is used to calculate MBH cross section as well as the mass at which the black hole ceases to be governed by classical GR and becomes a remnant.

Total number of dimensions Determines the number of dimensions in the ADD model used by Charybdis. This includes the three accepted spatial dimensions.

Minimum Black Hole Mass Lower cut off placed on generated MBH mass.

Maximum Black Hole Mass Upper cut off placed on generated MBH mass.

Number of particles in remnant decay When the MBH becomes lighter than a certain cut off it is no longer considered acceptable to model its behaviour using classical GR. The Black Hole becomes a remnant that can no longer decay via the process of Hawking Radiation. As there is no know theory of quantum gravity with which to model the further evolution of the MBH its remaining mass and any other conserved quantities are divided amongst a number of decay products. This variable determines the number of decay products that Charybdis should use.

Time variation of Black hole temperature The Hawking temperature of a black hole is derived from its mass, assuming the black hole follows a quasi-static evolution. The mass of an MBH changes as it decays and its Hawking temperature can be recalculated after each particle emission. Alternatively the Hawking temperature can be calculated at the point when the MBH is created and remain unchanged throughout its lifetime. This variable determines whether the temperature should change (true) or remain constant (false) during the lifetime of the MBH.

Grey Body factors At a basic level the probability of a black hole emitting a any particle with mass lower than the black holes temperature is equal. However, the gravitational field surrounding a black hole interacts with the particles it emits. This is especially true for particles with non-zero spin. The effect of these interactions is to change the spectrum of emitted particles from a black body spectrum to a so called *grey body* spectrum. This parameter determines weather or not the grey body factors are taken into account during the simulation.

Kinematic cut enabled This parameter determines whether the decay of the MBH obeys the *kinematic limit*. This is a result of Newtonian mechanics which means that the energy of a particle emitted by the black hole cannot exceed the energy of the remains of the black hole itself.

Option	**Default Value**
Plank Mass	1000 (GeV)
Total number of dimensions	6
Minimum Black Hole Mass	5000 (GeV)
Maximum Black Hole Mass	14000 (GeV)
Number of particles in remnant decay	2
Time variation of Black hole temperature	true
Grey Body factors	true
Kinematic cut enabled	true

Table 3.1: The configuration options made available by the Charybdis Micro Black Hole generator program are listed in the table above. The default value for each parameter as used during this analysis is also listed

3.4 Single Particle Event Generation

During the course of this analysis the response of the ATLAS detector to particles with specific properties was studied. This required the production of several data sets comprising events which contain only a single particle with those specific properties.

The Athena software framework includes a single particle event generator called single particle gun.

3.5 ATLAS Detector Simulation

Generated events must be passed through a simulation of the ATLAS detector in order to reproduce the detectors response.

3.5.1 ATLAS Fast Simulation

The ATLAS collaboration has developed a fast simulation of its detector, called ATLFAST. This program is designed to produce a rough estimate of the detectors response to a generated event, sacrificing accuracy for a reduction in the required CPU time per event.

ATLFAST is implemented as a set of parameters approximating the detectors response to the impact of different types of particle. The direction and energy of particles is take from the monte-carlo truth and smeared according to the detectors resolution in certain regions. Limits in the detectors design are also taken into account, preventing, for example, the identification of electrons with η higher than the limit of the ID.

3.5.2 ATLAS Full Simulation

The full simulation of the ATLAS detector is much more computationally intensive than the ATLFAST simulation discussed above. The full simulation is based on the GEANT package [16] which is used to simulate the passage of particles through matter.

The geometry of the ATLAS detector has been translated into a set of GEANT volumes for use in the simulation. This detector description has had several incarnations, with changes made when mistakes are discovered and when changes have been made to the expected detector layout.

The running of a simulation using all of the ATLAS full simulation software is separated into several stages. First the monte-carlo event generation is used to produce a set of particles, simulating all of there behaviour up until the point where they interact with any material surrounding the interaction point. The Passages of those particles through the beam pipe and on through the entire ATLAS detector is handled in the second stage. The second stage employs GEANT and the description of the physical detector held in the GEANT volumes mentioned above. The output of the second stage is a collection of charge deposition and other relics left in the detector by the passage of the simulated particles. The third stage of the full simulation emulates the digital readout systems employed by all the different sub-detectors in ATLAS. This third stage results in a set of data as close as possible to what would actually be produced by the ATLAS electronics after a physics event.

After the different stages of simulation have been executed the simulated data is passed to the actual ATLAS reconstruction software.

3.6 Summary

The ATLAS particle detector and the physics processes it has been designed to measure can be simulated through a number of different software packages. These simulations provided a controlled environment in which all the variables affecting the final output of the ATLAS experiment can be known. Comparisons between the results of controlled simulation and the unknown processes that lead to real physics data can be used to better understand that data and its probable cause.

The physics of MBH and the associated SM processes can be simulated by the Charybdis and Herwig packages respectively, providing an impression of the distribution of particles that may result from MBH events. The response of the ATLAS detector to those particles can be modelled in a comprehensive manor using the a number of different software packages collectively referred to as *full simulation*. A less accurate approximation to the detectors response can be achieved through the lower computational demands of the *ATLFAST* package.

4

TeV Energy Scale Electrons

4.1 Introduction

Micro Black Hole events can lead to the production of particles from the entire SM spectrum. The decay products occupy a broad range of energies which can extend up to a few TeV. Any analysis of MBHs will require a good understanding of the detector's response to particles with energies in the TeV range. An analysis of the detector's response to the full spectrum of particles expected from MBH events would be well beyond the scope of this work. A study of the ATLAS detector's response to very high energy electrons was carried out as a contribution to the complete analysis.

Two separate algorithms are used to identify high and low energy electrons, as described in chapter 1 section 1.4. Reconstructed electrons produced by the low energy algorithm have been ignored in this analysis as they have little barring on the reconstruction of TeV energy scale electrons.

The performance of electron reconstruction varies between the barrel and end-cap regions of the detector, so these are studied separately in all that follows. The region between the barrel and end-cap is known as the gap region. Electron reconstruction is poor in this region because the ID services are routed through this section of the detector, introducing a large amount of dead material. The performance in the gap region is analysed independently of that in the barrel and end-cap regions. Section 4.6 of this chapter shows that the effects of the gap region extend over the range $1.3 < |\eta| < 1.7$. The simulated single electron events studied in this analysis are separated into a barrel and an end-cap sample and referred to as such during some parts of this chapter. The barrel sample contains events in the range $|\eta| < 1.3$ whilst the end-cap sample contains events in the range $1.7 < |\eta| < 2.5$.

The process of identifying and reconstructing TeV energy scale electrons in the ATLAS detector is discussed in the rest of this chapter. The following section describes the production of simulated data necessary for the study. Later sections are concerned with electron identification and the reconstruction of energy and momentum.

4.2 Sample Generation

The Single Particle Gun monte-carlo program (chapter 3 section 3.4) was used to generate a set of data samples containing single electrons and single positrons with energies fixed at 0.5, 1.0, 1.5 and 2.0 TeV with a flat distribution in η between ± 2.5 and ϕ between $\pm\pi$. Each sample contained 10 000 events. The samples were then passed though the ATLAS full simulation software (chapter 3) in order to approximate the detector's response to the events.

The ATLAS electron reconstruction software calculates values for a number of different variables and employs them to identify potential electrons. The values associated with each successfully reconstructed electron are retained. However, those combinations of clusters and tracks that fail to be reconstructed as electrons are discarded, along with the calculated values which caused them to fail. The calculated values for the failed electrons must be studied in order to evaluate the electron reconstruction algorithm. The variables themselves proved to be complicated and replicating the software used to produce them would be difficult and prone to error. Instead, the selection criteria defined in the electron reconstruction software were altered to allow any combination of cluster and track to be successfully reconstructed as an electron, retaining the values of all the variables involved. As a result, some of the plots in the what follows have been produced from the standard ATLAS electron reconstruction whilst others show the results of the modified reconstruction. The plots produced using the modified reconstruction have been labelled as such.

4.3 Electron Selection

The decay of MBH can result in the production of very high energy electrons (on the order of a few TeV). The performance of the reconstruction software when handling TeV energy scale electrons must be determined in order to properly reconstruct MBH events. The electron selection and identification efficiency achieved by the ATLAS software has been determined by comparing the monte-carlo truth with the reconstructed electrons from the generated samples of single electrons (described above). When an event is found to contain more than one reconstructed electron then the most energetic reconstructed electron has been chosen for study in the following analysis. The selection efficiency is in this case a measure of how many reconstructed events contain at least one reconstructed electron.

The ATLAS software performs electron reconstruction in two separate stages. First, a *coarse* electron selection stage returns a large number of potential electron candidates. These candidate electrons represent combinations of signals in the EM calorimeter and ID which could potentially have been caused by the passage of an electron through the detector. The coarse electron selection has a deliberately large acceptance to ensure a high selection efficiency. The electron candidates are then passed through a second stage of *stringent* identification tests. These tests determine the likelihood that a reconstructed electron candidate represents a real electron. The acceptance for this second stage is necessarily lower than the first. The method of separating the electron reconstruction into two stages allows for more detailed analysis of reconstructed events. A naive analysis need only make use of those electrons which pass all the identification tests in the second stage whilst a more in depth analysis is free to interpret the results of the electron identification tests in more sophisticated ways.

Figure 4.1 shows the coarse and stringent electron reconstruction efficiency vs. generated energy for single electron events in the barrel and end-cap regions of the detector. The two plots shown in figure 4.1 indicate a decline in reconstruction efficiency with increasing generated energy. The fraction of single electron events which contain at least one reconstructed electron candidate shown in figure 4.1 (a) falls with increasing energy. The requirements of the stringent electron selection tests lead to a further reduction in efficiency, as shown in figure 4.1 (b). The coarse electron selection efficiency will be discussed in more detail in section 4.4 that follows. The effects of the stringent electron selection tests on the efficiency shown in plot (b) are discussed in section 4.5.

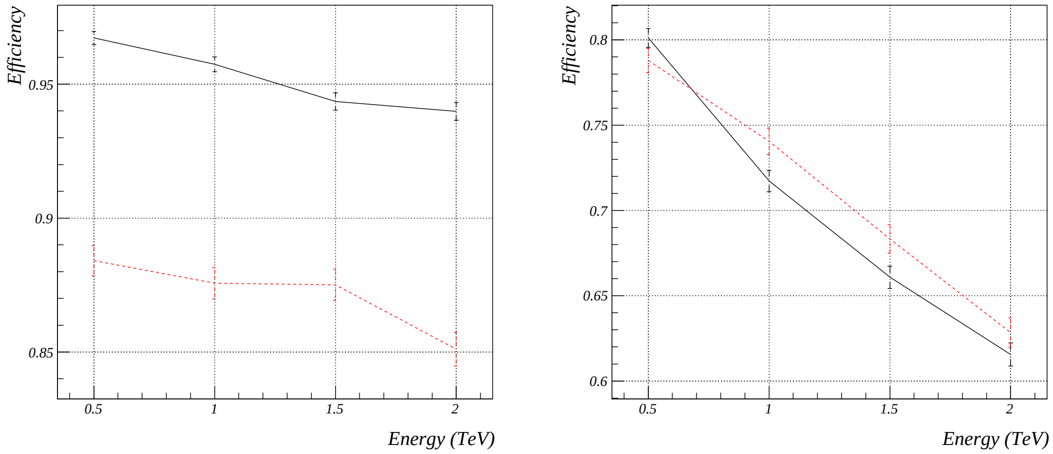

(a) (b)

Figure 4.1: The fraction of events containing at least one reconstructed electron shown as a function of the generated electron energy in TeV. The black and red lines represent the barrel and end-cap sections of the detector respectively. Plot (a) shows the fraction of events containing at least one electron candidate whilst plot (b) shows the fraction of events containing at least one electron which passes all of the subsequent electron identification tests.

4.4 Coarse Electron Selection

Each electron candidate object consists of a cluster in the EM calorimeter and a track in the ID which pass the coarse electron selection criteria. The candidates are produced by first testing all the EM clusters to reveal those that are likely to have been produced by photons or electrons, as apposed to other types of particle. An algorithm is then used to determine which, if any of the tracks in the ID best matches up with each of the chosen clusters.

The track matching algorithm used in Athena compares parameters that have been calculated from both the cluster and the track. Each potential cluster and track combination is assessed by considering the difference in position (in η and ϕ) and the energy reconstructed from an EM cluster divided by the momentum measured from a track,

test variable	**cut value**
$\Delta\eta$ 1^{st} sampling	< 0.05
$\Delta\phi$ 2^{nd} sampling	< 0.1
E/P	< 4.0

Table 4.1: Default track matching cuts imposed during the coarse electron selection by the ATLAS reconstruction software. The test includes placing a cut on the separation between track and cluster in η and ϕ as well as a cut on the energy reconstructed from a cluster divided by the momentum measured from the curvature of its associated track.

E/P. The difference in cluster and track position is measured by subtracting the weighted Barry centre of the cluster from the location of the ID track. The clusters η position is taken from the 1^{st} sampling of the calorimeter whilst the ϕ position is taken from the 2^{nd} sampling. This is done because the 1^{st} sampling of the calorimeter consists of fine strips running in the $r\phi$ direction which are designed to measure the structure of showers and offer the most precise measurement of η. The magnetic field in the ID distorts any showers which form there in the ϕ direction so no attempt is made to measure the structure of showers in ϕ (see chapter 1). The η and ϕ positions of the track are calculated by extrapolating the track into the region of the calorimeter in which the equivalent cluster position was measured. Table 4.1 summarises the cuts applied to $\Delta\eta$, $\Delta\phi$ and E/P during track matching.

The distributions of $\Delta\eta$ and $\Delta\phi$ for the single electron samples are shown in figure 4.2. The $\Delta\eta$ distribution is symmetric about zero but the $\Delta\phi$ distribution is not. The tail to negative values of $\Delta\phi$ is caused by radiation from electrons passing through the inner detector. The magnetic field in the ID runs parallel to the z-axis so accelerates electrons in the ϕ direction but not in η. This means that electrons are separated from radiated photons in ϕ by the ID's magnetic field. The electron samples used to generate this distribution contain both electrons and positrons in equal proportions. The distribution of

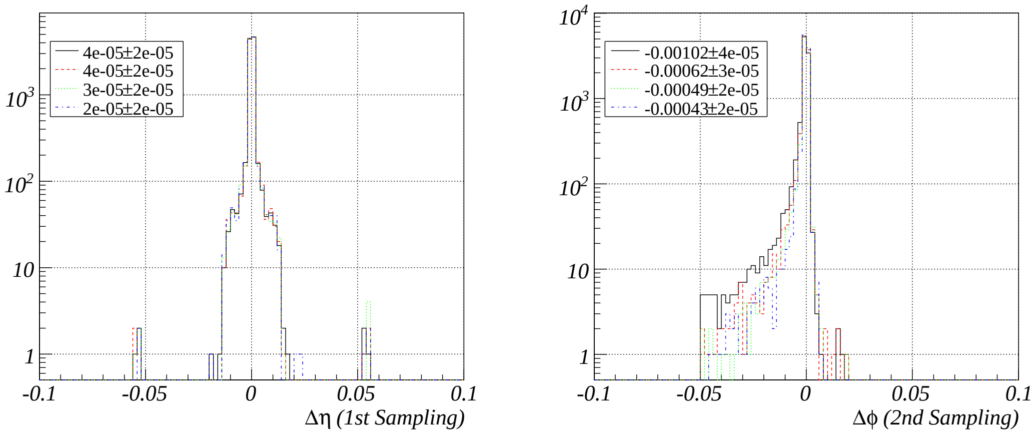

(a) (b)

Figure 4.2: Separation in (a) η in the first sampling of the EM calorimeter and (b) ϕ in the second sampling of the EM calorimeter between an EM cluster and the associated ID track. The plots show distributions for reconstructed electron candidates in samples of generated single electrons with energies of 0.5 TeV (black), 1.0 TeV (red), 1.5 TeV (green) and 2.0 TeV (blue).

$\Delta\phi$ should therefore be symmetric as the negative and positively charged electrons should bend in opposite directions under the influence of the magnetic field. This symmetry is removed by the ATLAS reconstruction software by changing the sign of $\Delta\phi$ based on the curvature of the reconstructed track (and therefore on the reconstructed charge of the tracked particle). This is done to ensure that all large $\Delta\phi$ resulting from radiation are on the negative side of the distribution, simplifying the process of identifying this radiation and correcting for it. The cuts on $\Delta\phi$ detailed in table 4.1 are applied to this unsymmetrical distribution.

The distributions shown in figure 4.2 both fall entirely within the range specified by the cuts imposed on them ($|\Delta\eta| < 0.05$ and $|\Delta\phi| < 0.1$). These distributions have no effect on electron reconstruction efficiency at the TeV energy scale.

The energy calculated from a cluster is compared with the momentum calculated from a track as part of the track matching process. The energy and momentum of a highly relativistic particle should be approximately the same. $E^2 = P^2 + m^2$ where the mass m is a constant which can be ignored once E and P become sufficiently large. Energy and momentum are compared by studying the value of E/P and demanding that for a matching cluster and track its value is close to one.

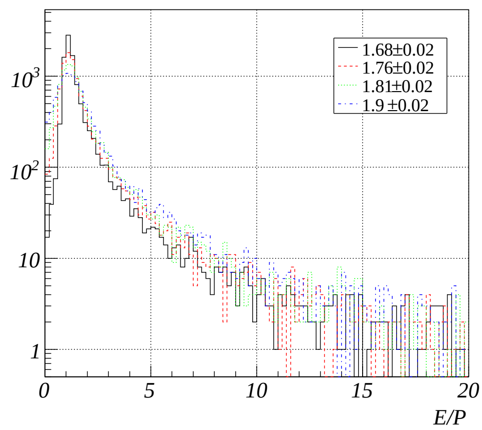

(a)

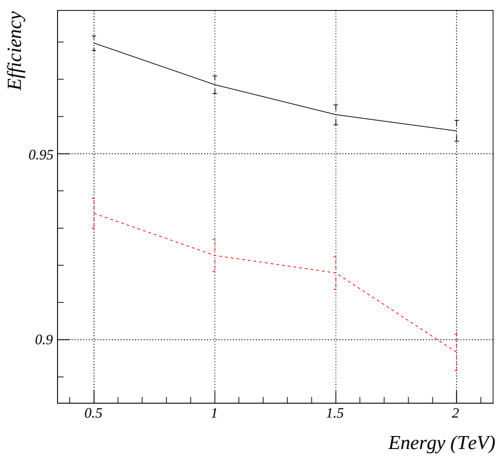

(b)

Figure 4.3: Showing the E/P distributions for samples of single electrons generated with energies of 0.5 TeV (black), 1.0 TeV (red), 1.5 TeV (green) and 2.0 TeV (blue) are shown in (a). The fraction of those events that fulfil the cut on $E/P > 4.0$ is shown in (b) as a function of energy. The black and red lines in (b) indicate the efficiency of the E/P cut in the barrel and end-cap sections of the detector respectively.

Figure 4.3 shows the distribution of E/P for the same single electron samples described above. The electron candidate reconstruction algorithm rejects matches between cluster and track where $E/P > 4.0$. Figure 4.3 (b) shows that the selection efficiency in the barrel region (black line) drops from 0.98 at 0.5 TeV to 0.96 at 2.0 TeV. The efficiency in the end-cap region (red line) falls from 0.93 to 0.89 over the same energy range.

The efficiency of the E/P selection cut is consistently worse in the end-cap region than in the barrel region over the entire energy range. This is because the $1/P_T$ resolution is poorer in the end-cap region than the barrel region[3]. This degradation in resolution is in part caused by non-uniformity in the B-field towards the end of the ID's solenoid.

4.5 Stringent Electron Selection

A number of different tests are performed by the reconstruction software in order to determine the likelihood of an electron candidate representing a real electron. The results of these tests are made available along with the reconstructed electron candidates and open to interpretation during analysis work. The ATLAS collaboration recommends that only electrons passing all of these electron identification tests should be considered as part of a physics analysis. The efficiency of electron identification in this second stage of the reconstruction is discussed in this section.

The cuts imposed on electron candidates as part of the stringent electron selection are as follows.

Hadronic Leakage A cut is placed on the ratio of E_T measured in a $\Delta\eta \times \Delta\phi = 0.2 \times 0.2$ section of the first compartment of the hadronic calorimeter to the E_T measured in the EM calorimeter.

LArEM 2nd Sampling A test based on the shape of an electrons shower in the second sampling of the EM calorimeter. The test is divided into two parts. The first part is a cut on the energy deposited in a $\Delta\eta \times \Delta\phi = 3 \times 7$ cell cluster divided by the energy in a 7×7 cluster. In the second part the lateral width of the shower is calculated in a 3×5 cell window. The calculation involves weighting the η position of each cell with its energy before finding their standard deviation.

LArEM 1st Sampling A test based on the shape of an electrons shower in the first sampling layer of the EM calorimeter. This test uses the fine strips that make up the calorimeter in the range $|\eta| < 2.35$ to detect substructure in a shower. This aids in the identification of single π^0, γ or other particles which may have been included in a shower. The test involves a search for multiple peaks in energy over the region covered by a shower as well as cuts on the width of the shower and the shape of its core.

Track η Rejects any tracks with a reconstructed η beyond the extent of the precise region of the SCT.

Track Hits A0 Rejects tracks which have a low number of hits in either the pixel or SCT sub-detectors. A cut is also placed on the impact parameter A0 between the track and the vertex of the event.

Track Match and E/P Imposes a cut on the separation in η and ϕ between a track and its associated cluster within the EM calorimeter. The test also rejects potential electrons when reconstructed energy does not match reconstructed momentum by placing a cut on E/P.

Track TRT Uses the TRT to reject hadronic tracks by cutting out those with a low proportion of high threshold hits (see chapter 1).

Figure 4.4 shows the fraction of reconstructed electrons that pass each of the stringent selection cuts. These results were obtained by running the Athena electron reconstruction with the recommended default settings. Electrons produced by the separate soft electron reconstruction algorithm were ignored. The information is plotted as a function of generated electron energy. The efficiency of the Hadronic and LArEM 1st sampling tests

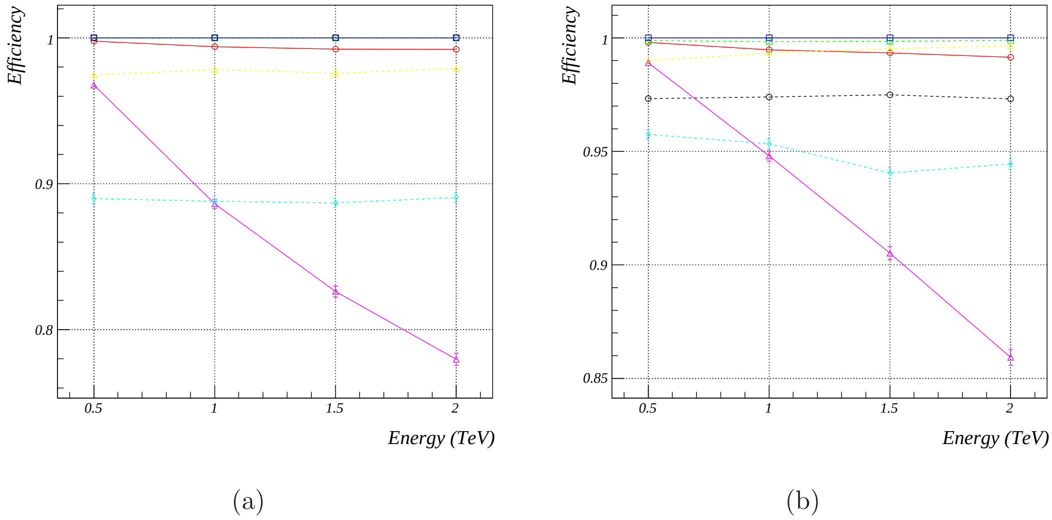

Figure 4.4: Showing the number of electrons which pass the each of the stringent electron selection cuts divided by the number of electrons which pass the course electron cuts. Each of the tests is represented by a different colour; Hadronic Leakage (black), LArEM 2nd Sampling (red), LArEM 1st Sampling (green), Track η (dark blue), Track Hits A0 (yellow), Track Match and E/P (pink) and Track TRT (light blue). Plot (a) shows the results for the barrel and (b) the end-cap regions of the detector.

(represented by the black and green lines) cannot be seen in figure 4.4 (a) as they have a pass rate of 1.0, which is identical to that represented by the dark blue line and are obscured by it.

The LArEM 1st and 2nd sampling, track η and Track Hits A0 tests show relatively little variation with energy or η and will not be discussed further. The remaining tests appear to have the largest effect on reconstruction efficiency and are discussed in more detail. The fraction of electrons that pass the Track Match and E/P test (shown in pink, figure 4.4) shows the strongest dependence on energy in both the barrel and end-cap regions of the detector. The fraction of electrons passing this test in the barrel region (plot (a)) falls from 0.97 at 0.5 TeV to 0.78 at 2.0 TeV. The fraction passing the test in the end-cap region (plot (b)) falls from 0.99 at 0.5 TeV to 0.86 at 2.0 TeV. This test is the main cause of the drop in electron reconstruction efficiency with energy for very high energy electrons and is discussed in more detail in section 4.5.1. The fraction of electrons passing the Track TRT test (shown in light blue, figure 4.4) remains relatively constant as energy increases. However, the fraction of electrons passing this test in the barrel region is approximately 0.89 whilst in the end-cap region it is nearer 0.95. The efficiency is higher in the end-cap than the barrel region and the difference between the two is approximately 5%, which is larger than any of the other tests. This observation is discussed in section 4.5.3. The fraction of electrons passing the hadronic leakage test (shown in black, figure 4.4) also changes between the barrel and end-cap regions. The fraction of electrons passing the test is 1.0 in the barrel region but falls to approximately 0.97 in the end-cap region. The behaviour of this test is discussed in section 4.5.2.

Each of the electron identification tests consists of one or more cuts imposed on a particular variable. In several cases the value of the cuts changes as a function of η. This is because the properties of the detector change with η and the electron reconstruction algorithms must compensate for this. Where this is the case during the following sections the fraction of electrons passing a test is shown in each of the different η ranges and the default values of each cut are presented.

4.5.1 Track Match and E/P

The track match and E/P test is essentially a more aggressive version of the track matching procedure applied in the coarse selection of electron candidates, as described in section 4.4. The test provides an indication of how well clusters and tracks are matched. Cuts are applied to the separation between cluster and track in η and ϕ as well as the value of E/P. The cut applied to E/P is different in the barrel and end-cap sections of the detector. The cuts applied during the track match and E/P stringent electron selection are summarised in table 4.2. The distributions of $\Delta\eta$ and $\Delta\phi$ and E/P for the generated single electron samples discussed above have already been presented in figure 4.2 ($\Delta\eta$ and $\Delta\phi$) and figure 4.3 part (a) (E/P). However, these plots were produced before the coarse electron candidate selection cuts had been applied. Figure 4.6 shows the distribution of $\Delta\eta$ and E/P for the highest energy reconstructed electron in each event after the coarse electron candidate selection cuts have been applied. The same figure also shows the fraction of electrons that pass the $\Delta\eta$ and E/P cuts as part of the track match and E/P stringent electron selection. The highest energy reconstructed electron in every generated events passed the cuts on $\Delta\phi$ so these distributions are not shown.

test variable	**cut value**
$\Delta\eta$ in 1^{st} sampling	< 0.02
$\Delta\phi$ in 2^{nd} sampling	< 0.05
E/P in barrel region	0.8 - 1.3
E/P in end-cap region	0.7 - 2.5

Table 4.2: Track Match and E/P cuts imposed on electron candidates as part of the stringent electron selection process. The test involves placing cuts on the separation between cluster and its track in η and ϕ as well as the energy reconstructed from the cluster divided by the momentum measured from the curvature of the associated track.

Table 4.2 shows that the cuts placed on the minimum and maximum values of E/P are more relaxed in the end-cap region than they are in the barrel region. This is because the momentum, P is measured by first finding the transverse momentum, P_T and then dividing by $\sin\theta$. The measurement of P_T is made by finding the radius of curvature of the track in the ID's magnetic field. Tracks in the end-cap region will have a smaller fraction of momentum in the measurable transverse direction than those in the barrel. The measurement of E/P is therefore less reliable in the end-cap region.

Figure 4.5 (b) shows that the majority of electrons pass the cuts imposed on $\Delta\eta$. The

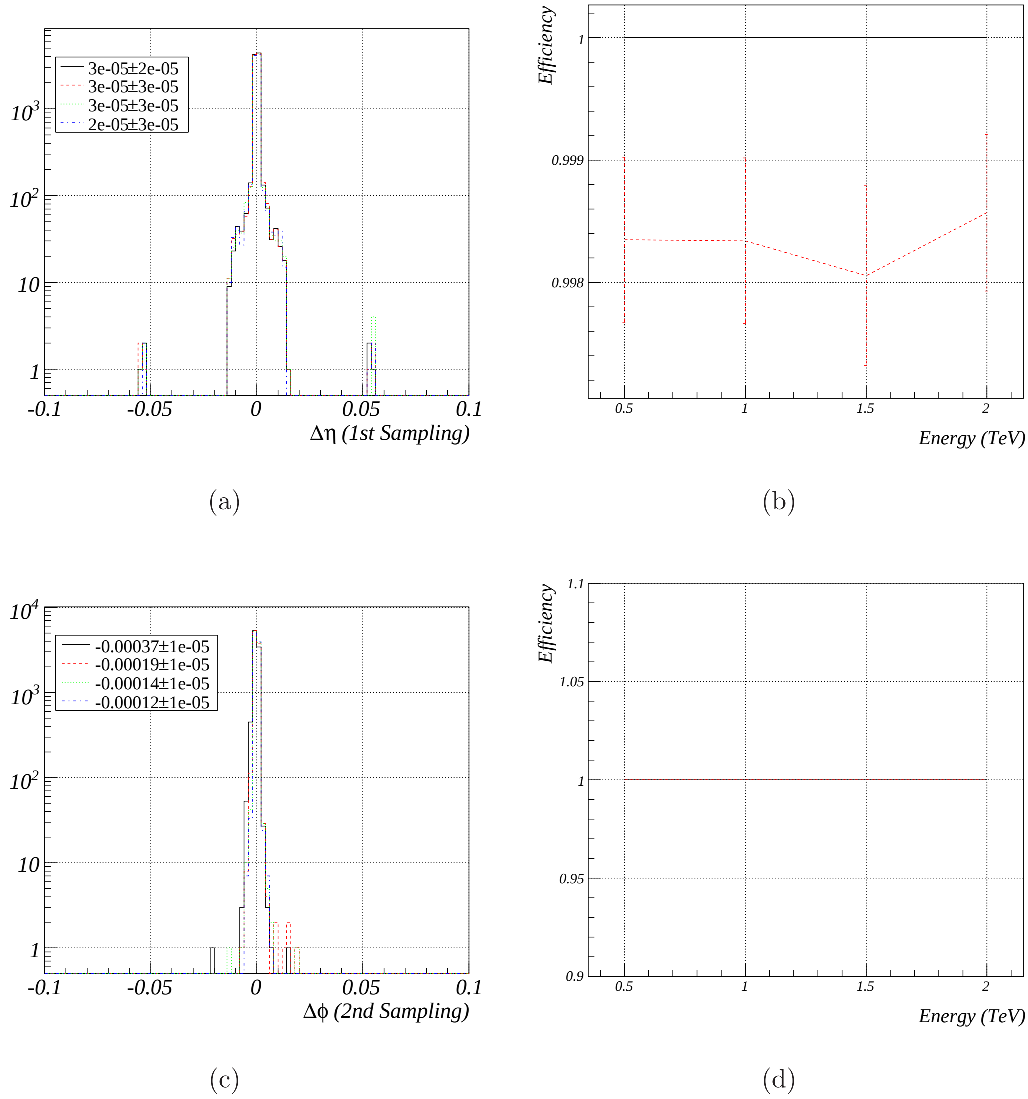

Figure 4.5: Showing the track match distributions associated with the track match and E/P test for the highest energy reconstructed electron which passes the course electron selection cuts in each event. The distribution of $\Delta\eta$ in the 1^{st} sampling of the EM calorimeter in both the barrel and end-cap regions is shown in (a). The fraction of electrons which pass the track match $\Delta\eta$ cuts is shown separately for the barrel and end-cap regions in (b). The distribution of $\Delta\Phi$ in both the barrel and end-cap regions is shown in (c). The fraction of electrons which pass the track match $\Delta\Phi$ cuts is shown separately for the barrel and end-cap regions in (d). The black, red, green and blue lines in (a) and (c) represent events in both the barrel and end-cap regions with generated energy of 0.5, 1.0, 1.5 and 2.0 TeV respectively. The black and red lines (b) and (d) represent the fraction of electrons passing each of the cuts in the barrel and end-cap regions of the detector respectively.

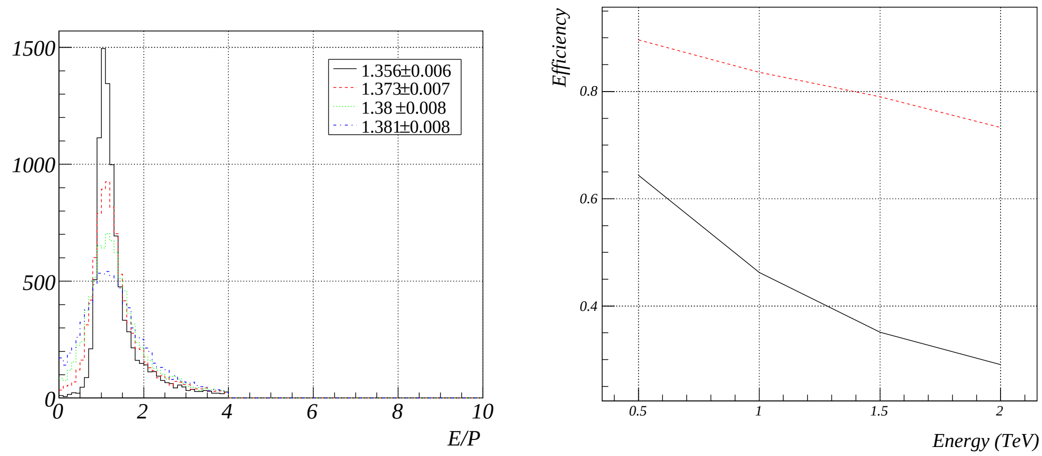

(a) (b)

Figure 4.6: Showing the E/P distribution associated with the track match and E/P test for the highest energy reconstructed electron in each event. The distribution of E/P in both the barrel and the end-cap is shown in (a) whilst the fraction of events in which the highest energy electron passes the track match E/P cuts is shown in (b). The black, red, green and blue lines in (a) represent events with generated energy of 0.5, 1.0, 1.5 and 2.0 TeV respectively. The black and red lines (b) represent the fraction of electrons passing each of the cuts in the barrel and end-cap regions of the detector respectively.

pass rate in the barrel region is 1.0, that in the end-cap is slightly lower at approximately 0.998 but still very close to one. The pass rate does not have a dependence on generated electron energy across the single electron samples studied.

The E/P distributions shown in figure 4.6 (a) become broader as the generated electron energy increases. The plots in figure 4.6 (b) show that the fraction of events in which the highest energy reconstructed electron has an E/P within the imposed cuts falls as the generated electron energy increases. The fraction of electrons that pass the E/P cuts in the barrel region falls from 0.65 at 0.5 TeV to 0.30 at 2.0 TeV. The fraction that pass the cuts in the end-cap falls from 0.90 at 0.5 TeV to 0.75 at 2.0TeV. The plot also shows that the pass rate in the barrel region is considerably lower than it is in the end-cap region.

The poor E/P distribution is caused by increasingly poor electron momentum reconstruction at higher energies. This is expected and discussed further in section 4.7. The E/P distribution is entirely responsible for the behaviour of the track match and E/P test pass rate shown by the pink line in figure 4.4.

4.5.2 Cluster Hadronic Leakage

Electromagnetic objects such as electrons or photons generally deposit most of their energy by showering in the EM calorimeter. Hadronic objects tend to have longer showers which extend through the EM calorimeter and into the hadronic calorimeter. The fraction of the energy in a reconstructed shower that is deposited in the hadronic calorimeter can be used to separate hadronic from electromagnetic objects. This is often referred to as *hadronic leakage* when mentioned in the context of electromagnetic objects. The hadronic leakage of electron candidates is calculated by dividing the energy deposited in the hadronic calorimeter behind the electron's cluster by the energy deposited by the electron in a 3x7 cell cluster in the EM calorimeter. The distribution of the hadronic leakage for the generated single electron samples is shown in figure 4.7. The fraction of reconstructed electrons which pass the hadronic leakage cuts imposed as part of the stringent electron selection is shown in the same figure. The hadronic leakage cuts used in different η ranges are shown in table 4.3.

The different cut values shown in table 4.3 have been designed to account for the variation in calorimeter depth and the distribution of dead material across the different η ranges over which they apply. With correctly adjusted cut values the pass rate for the hadronic leakage test should be constant across the detector.

Figure 4.4 shows that the efficiency for the hadronic leakage test remains constant

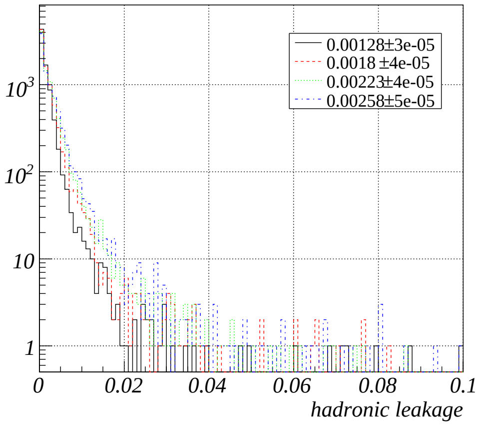

(a)

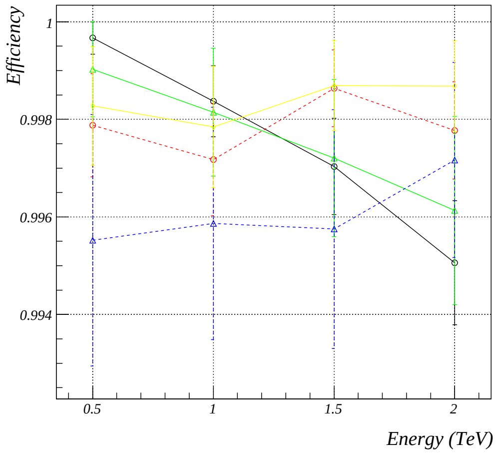

(b)

Figure 4.7: The E_T deposited in the hadronic calorimeter divided by the E_T measured in a 3x7 cell cluster for the most energetic reconstructed electron in each event for both the barrel and end-cap regions is shown in (a). The distributions show were produced from a sample of single electrons with generated energies of 0.5 TeV (black), 1.0 TeV (red), 1.5 TeV (green) and 2.0 TeV (blue). The fraction of the highest energy reconstructed electron's in each event which pass the hadronic energy leakage test is shown in (b). The different coloured lines in (b) indicate reconstructed electrons with η between 0-0.8 (black), 0.8-1.5 (red), 1.5-1.8 (green), 1.8-2.0 (blue) and 2.0-2.47 (yellow).

between 0.5 TeV and 2.0 TeV for the 0.8-1.5 (red), 1.8-2.0 (blue) and 2.0-2.47 (yellow) η regions. The efficiency falls from 0.999 at 0.5 TeV to 0.996 at 2.0 TeV in the 0-0.8 (black) and 1.5-1.8 (green) η regions. The 0-0.8 and 1.5-1.8 η regions which exhibit the drop in efficiency with energy also have the largest maximum hadronic leakage cuts, as shown in table 4.3.

The difference in the pass rate for the hadronic leakage test between the barrel and end-cap sections apparent in figure 4.4 is not present in figure 4.7. Any difference in efficiency between barrel and end-cap would result in a difference between the 0-0.8 and 0.8-1.5 η regions (black and red lines) and the 1.5-1.8, 1.8-2.0 and 2.0-2.47 η regions (green, blue and yellow lines).

η range	max. Hadronic Leakage Fraction
0 - 0.8	0.04
0.8 - 1.5	0.025
1.5 - 1.8	0.05
1.8 - 2.0	0.03
2.0 - 2.47	0.025

Table 4.3: Showing the cuts imposed on electron candidates as part of the the cluster hadronic leakage test. These cuts are the maximum allowed values for the ratio of energy deposited by an electron candidate in the hadronic calorimeter over the energy deposited in a 3x7 cell region of the EM calorimeter.

4.5.3 Track TRT

The Track TRT test takes advantage of the transition radiation produced by electrons as they pass through the radiator material in the TRT. Transition radiation increases the signal produced by a straw tube in the TRT. The readout for each straw tube is able to discriminate between normal and increased signal hits (those with transition radiation) by using two separate signal threshold values, one lower and one higher. The sub-detector has been designed to produced transition radiation only in response to the passage of an electron. The proportion of high threshold hits in an electron's track should be much higher than that in a track produced by any other particle. A cut imposed on the proportion of high threshold hits can improve electron identification. Figure 4.8 shows the distribution of low threshold hits, high threshold hits and the ratio between them as produced by the TeV scale single electron samples described above.

The cuts imposed on the ratio of high threshold hits to the total number of hits in different parts of the detector are summarised in table 4.4. The track TRT test is not applied in the most forward region between 2.0 and 2.47, hence the cut value of -1 given in table 4.4 and the pass fraction of 1 shown by the yellow line in figure 4.8. The test is not applied in the range $2.0 < |\eta| < 2.47$ because there are no active TRT components

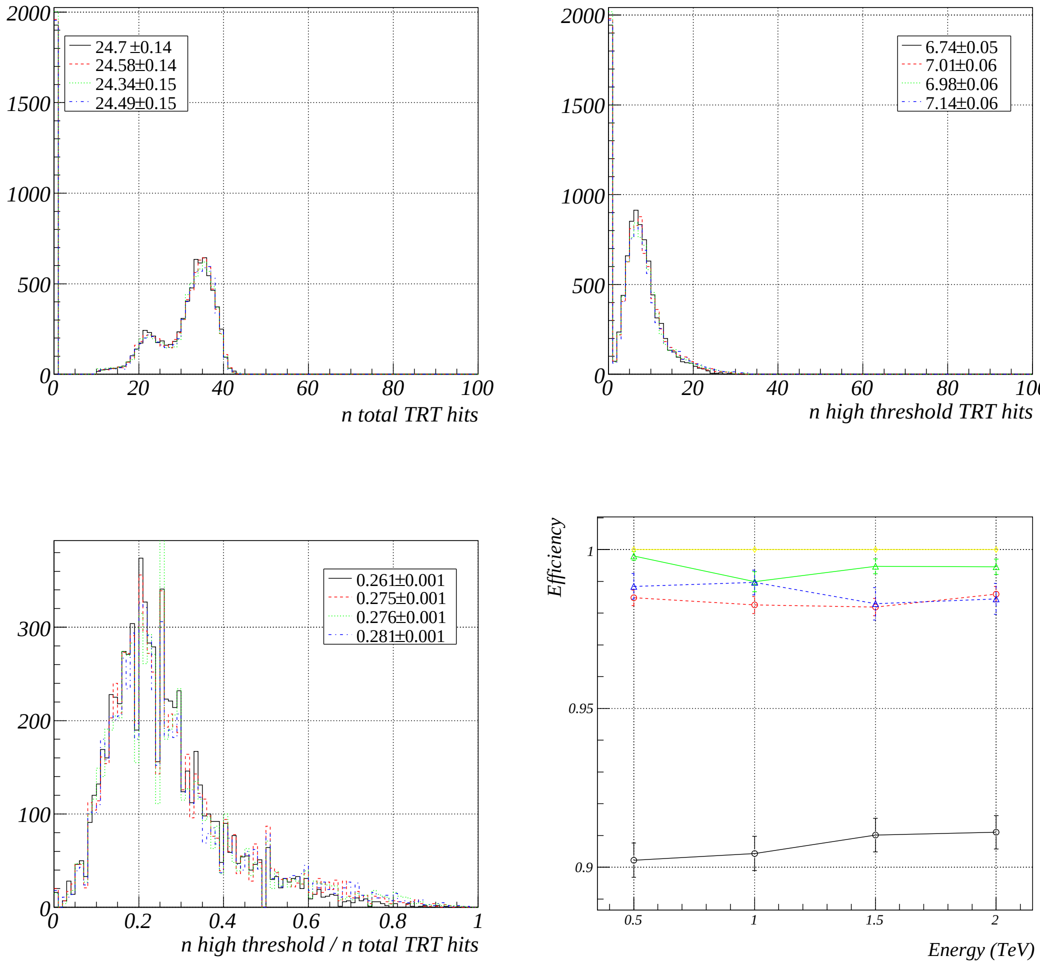

Figure 4.8: Showing the number and type of hits in the TRT for single electrons with generated energies of 0.5 TeV (black), 1.0 TeV (red), 1.5 TeV (green) and 2.0 TeV. Plot (a) shows the total number of hits in the TRT, (b) the number of high threshold hits in the TRT and (c) the ratio of high threshold hits to the total number of hits. The plot in (d) shows the fraction of electrons which pass the Track TRT cut. The different coloured lines in plot (d) show the pass rate in the five different η ranges over which the cut is applied. These ranges are 0-0.8 (black), 0.8-1.5 (red), 1.5-1.8 (green), 1.8-2.0 (blue) and 2.0-2.47 (yellow).

η range	min. high threshold hit fraction
0 - 0.8	0.1
0.8 - 1.5	0.08
1.5 - 1.8	0.1
1.8 - 2.0	0.1
2.0 - 2.47	-1

Table 4.4: Showing the cuts placed on reconstructed electron candidates as part of the track TRT electron identification test. The number of hits in a track which pass the TRT's built in high threshold cut is divided by the total number of hits in the same track. The resulting fraction must be higher than the minimum value specified. The minimum value varies with η and the test is not applied to electron candidates in the range $2.0 < |\eta| < 2.47$.

in the region. Changes in the design of ATLAS led to the section of the TRT in question being delayed, and then replaced by SCT services.

Figure 4.4 shows that the efficiency for the track TRT stringent electron selection does not vary with energy but does change from 0.89 in the barrel region to approximately 0.95 in the end-cap region of the detector. This behaviour is also apparent in figure4.8 (d). The figure indicates that the efficiency for the track TRT stringent electron selection does not vary with electron energy. However, the efficiency in the 0-0.8 η region (black line) is approximately 0.91 whilst in the 0.8-2.47 region (red, green and blue lines) the efficiency is approximately 0.99. The lower efficiency in the 0-0.8 η region contributes to the lower efficiency in the barrel region seen in figure 4.4.

The track TRT is not applied in the 2.0-2.47 η region so all electrons in this region are seen to pass the cut. This also contributes to the higher efficiency in the end-cap region than in the barrel region for the track TRT stringent electron selection.

4.6 Energy Reconstruction For TeV Energy Scale Electrons

The ability of the ATLAS calorimeter to reconstruct the energy of electrons will affect the precision of any measurement of MBH mass. It is therefore important to understand the energy reconstruction of very high energy electrons produced in MBH decays. The energy of reconstructed electrons is measured using the EM calorimeter and should follow a normal distribution about the generated electron energy. The distributions of E/E^{true} for both the barrel and end-cap sections of the detector are shown in figure 4.9 for the samples of generated single electrons described in section 4.2. The distributions are shown along with fitted Gaussian functions, the mean, linearity and width of which are also shown in the same figure.

The distributions of E/E^{truth} shown in figure 4.9 for both the barrel (a) and end-cap (b) regions have fitted Gaussian functions with mean close to one (shown in plot (c)). The difference of approximately 0.5% between the reconstructed and generated electron energy is equivalent to a few GeV at the TeV energy scale studied. The variation in the mean with energy is also very small, indicating that the linearity of the reconstructed electron energy is very good in both the barrel and the end-cap regions of the detector.

The mean of the fitted distributions in both regions of the detector show a small decrease (on the order of a few GeV) with increasing generated energy. This may be due to an increase in hadronic leakage with electron energy, as is apparent in figure 4.7 (a). This hypothesis could not be confirmed without further investigation.

Figure 4.10 (b) shows how the mean of the E/E^{truth} distributions changes as a function of $|\eta|$ for the four different energy electron samples. This is not the mean of Gaussian

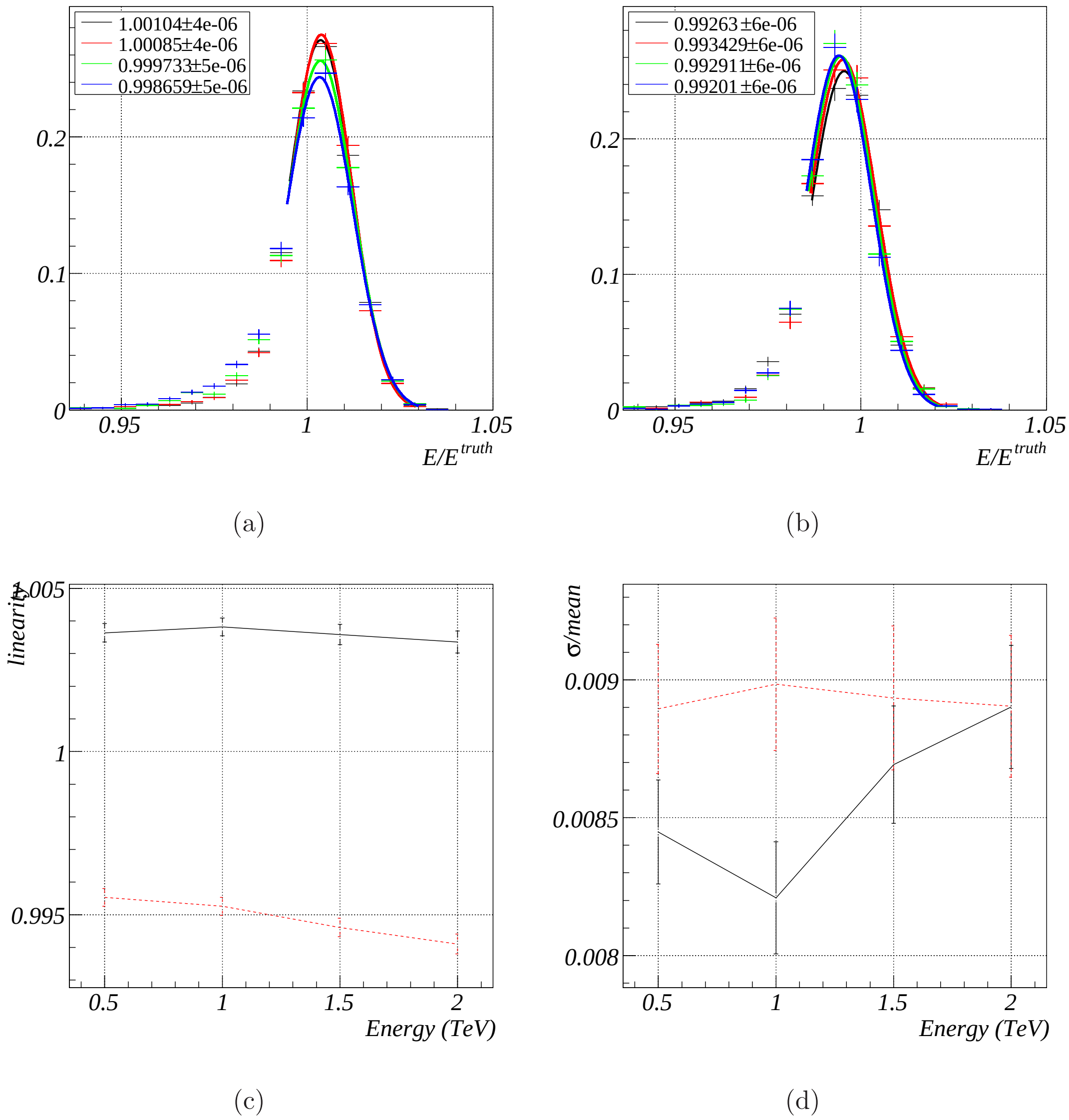

Figure 4.9: Showing reconstructed electron energy resolution. These plots show the distribution of reconstructed electron energy divided by the generated electron energy, E/E^{truth} as recorded in the monte-carlo truth. Distributions for 0.5 (black), 1.0, (red) 1.5 (green) and 2.0 (blue) TeV samples of single electrons are shown along with with a fitted Gaussian function. The relevant distributions for the barrel section of the SCT are shown in (a) whilst those for the end-cap are shown in (b). Plots (c) and (d) show the mean and σ/mean obtained from the fitted Gaussian as a function of the generated electron energy. The results in plots (c) and (d) are shown in black for the barrel region and red for the end-cap.

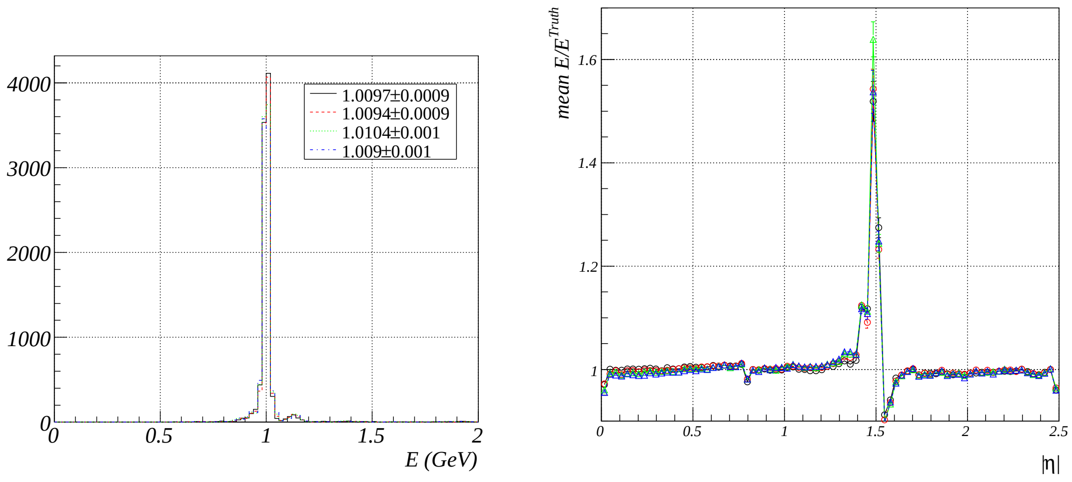

(a)

(b)

Figure 4.10: Showing the distribution of E/E^{truth} for all η in (a) and the mean of the distribution as a function of $|\eta|$ in plot (b).

functions fitted to the data (as shown in figure 4.9 (c)) but the mean of the entire distribution. This is because the samples contained insufficient statistics to produce reasonable fits when divided over so many bins in η. As a result, the mean values shown in figure 4.10 (a) are more strongly influenced by tails and non-Gaussian behaviour in the E/E^{truth} distributions. The largest peak in figure 4.10 (b) appears at $|\eta| = 1.475$. The position of this peak is consistent with the end of the EM calorimeter's barrel section (chapter 1 section 1.3.2). Electrons with $|\eta| > 1.475$ would be measured entirely by the EM calorimeter's end-cap and the gap scintillator (chapter 1 figure 1.8).

The smaller dip at $|\eta| \sim 0.8$ is consistent with a small reduction in the total radiation length of the EM calorimeter's third (largest r) sampling at the same position in η. This feature of the EM calorimeter is shown in[20].

The peak at $|\eta| = 1.475$ and the smaller features extending to $|\eta| = 1.3$ correspond with the gap-region in the range $1.375 < |\eta| < 1.475$. However, the plot shows that the mean reconstructed energy deviates from the generated value over the range $1.3 < |\eta| < 1.7$. These deviations include the peaks in the range $1.3 < |\eta| < 1.5$ and the dip in the range $1.5 < |\eta| < 1.7$. This observation was used to determine that electrons in the range $1.3 < |\eta| < 1.7$ should be excluded from the analysis in this chapter in order to avoid the effects of the gap region.

Figure 4.10 (b) indicates that at $|\eta| \sim 1.5$, the region covered by the largest peak, the mean reconstructed electron energy is ~ 1.6 times the generated energy. An increase in the reconstructed energy above the value of the generated energy cannot be explained by energy losses in the detector. Instead, the increase in reconstructed energy is likely to result from a miss calibration of the calorimeter in this region and/or at the TeV energy scale. The energy reconstruction formula used to interpret data from the ATLAS detector's EM calorimeter is shown in Equation 4.1. This is exactly the same as equation 1.1 in chapter 1.

$$E_{Total} = W_{global} \left(W_{ps} E_{ps} + E_{str} + E_{mid} + E_{back} \right) \tag{4.1}$$

Energy reconstruction in the EM calorimeter (described in more detail in chapter 1) involves summing the energy collected in each layer of the EM calorimeter and that collected in the pre-sampling layer. The energy measured in the pre-sampler is weighted before being added to the sum. The weight used, W_{ps} is dependent on η. W_{ps} is determined empirically varying its value whilst trying to optimise the energy resolution. The pre-sampling layer is used to compensate for energy losses and early showering of charged particles in dead material throughout the ID. The variation in the value of W_{ps} with η is used to account for the variation in material and the resulting variation in energy loss in

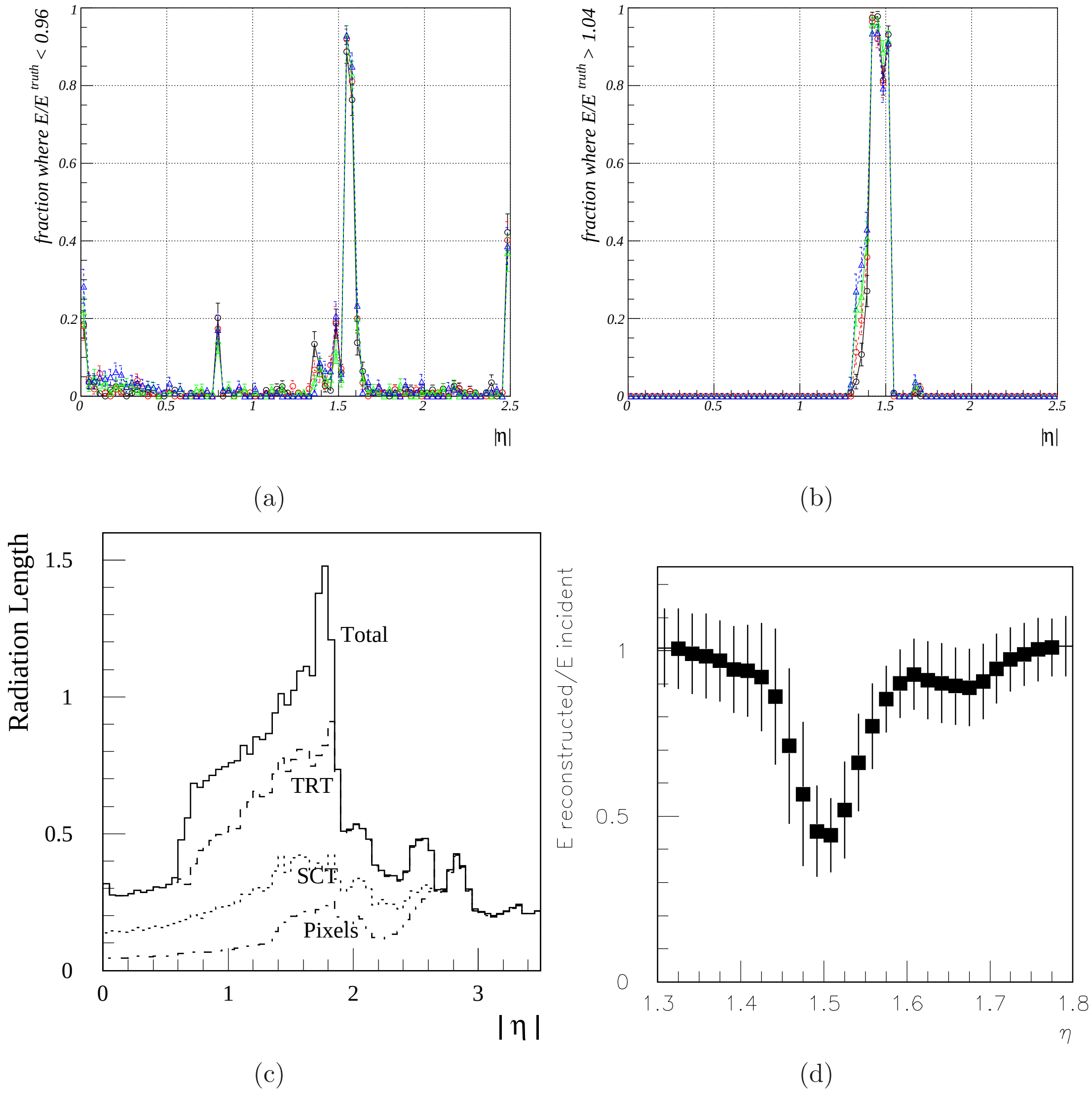

Figure 4.11: Showing the fraction of the highest energy electrons in each event whose reconstructed energy deviates from the generated, monte-carlo truth energy by a significant amount. The first two plots show the fraction of these electrons for which E^{Rec}/E^{truth} is less than 0.96 (a) and greater than 1.04 (b). Plot (c) shows the material distribution in the ID whilst plot (d) shows the distribution of E^{Rec}/E^{truth} for electrons with E_T of 10 GeV as a function of $|\eta|$ before the weighted energy measured in the pre-sampler and gap scintillator are added. Plots (c) and (d) both originated in the ATLAS TDR[2].

the ID. Energy measurements in the gap region of the detector also include data from a thin scintillator located inside the gap region. This scintillator has been incorporated into the detector specifically to compensate for the reduced instrumentation in the gap region. Figure 4.11 (c) and (d) were taken from the ATLAS TDR[2]. Plot (d) demonstrates the relative importance of the pre-sampler and scintillator corrections to energy reconstruction in the gap region. The figure shows the ratio of reconstructed electron energy to generated electron energy as a function of η for electrons with E_T of 10 GeV. The reconstructed energy in this figure does not include the weighted measurements taken from the pre-sampler and scintillator. As a result the reconstructed energy is much lower than the generated value in the gap region. When the weighted energy deposits in the pre-sampler and the gap scintillator are added the reconstructed energy distribution for the 10 GeV electrons becomes flat[2]. At η equals 1.5 the weighted pre-sampler and gap scintillator contribute approximately half of the reconstructed energy.

Figure 4.11 (a) and (b) were produced from the distribution of E^{Rec}/E^{Truth} for the highest energy reconstructed electron in each generated single electron event. This distribution is shown in figure 4.10 (a). The plots show the fraction of the electrons that occupy the tails of this distribution as a function of $|\eta|$. Figure 4.11 (a) shows the fraction with $E^{Rec}/E^{Truth} < 0.96$ whilst (b) shows the fraction with $E^{Rec}/E^{Truth} > 1.04$. These plots indicate that the fraction of electrons with reconstructed energy greater than expected is larger in the region $\eta < 1.5$. The fraction of electrons with reconstructed energy lower than expected is greater in the region $\eta > 1.5$. At $|\eta|$ equals 1.5 the magnetic solenoid in the ID and the pre-sampling layer in the ID come to an end. This can be seen in chapter 1 figure 1.8. The fraction of electron energy that is lost in the solenoid should fall as the incident energy increases. The depth of a shower in the calorimeter increases with energy but the thickness of the dead material in front of the calorimeter remains constant. As incident energy increases the fraction of the showers volume contained within the dead material will decrease. As the value of W_{ps} has no dependence on the incident energy it cannot compensate for this change in the fraction of energy lost in dead material. The weighting of the energy deposits in the pre-sampler is likely to over compensate for energy losses in dead material at the TeV energy scale. This over compensation may account for the excess reconstructed energy in the region just bellow $|\eta| = 1.5$ shown in figure 4.10 (b) and figure 4.11 (b). Further investigation would be necessary to confirm this.

The ATLAS collaboration's calorimeter group list the development of energy dependant weights on the pre-sampler as something they intend to work on in the future.

4.7 Momentum Reconstruction For TeV Energy Scale Electrons

Measurements of electron momentum rely on the associated track in the ID. The curvature of the track determines the measured P_T of an electron and this is used in combination with the η of the track to reconstruct its total momentum. The measurement of P_T is directly proportional to the electron track's radius of curvature. The radius of a track is in turn inversely proportional to the separation between hits in ϕ. The smaller the radius the more the direction of the track changes as is passes through the detector. The ϕ position of hits in the track is the measured quantity used to determine P_T and it is this that should display a normal distribution similar to the measured electron energy discussed above. Studying the distribution of $1/P_T$ provides a good measure of electron momentum reconstruction performance. Figure 4.12 shows the distribution of P_T^{truth}/P_T

for electrons reconstructed in the different regions of the inner detector.

The distributions shown in figure 4.12 have a mean greater than one in both the barrel and end-cap regions. This indicates that the generated monte-carlo truth momentum is slightly larger than the mean measured value. This is to be expected as electrons are likely to lose momentum through radiation in the ID. The emission of radiation reduces the magnitude of an electrons momentum, leading to reconstructed tracks with a smaller radius of curvature. This in turn produces a lower measure of P_T. The distributions also exhibit tails to high values of P_T^{truth}/P_T with the effect being larger in the end-cap region. These tails are also likely caused by momentum loss through radiation. Material density is higher in the end-cap, leading to an increased probability of radiation in that region which corresponds with the larger tails in the end-cap distributions.

The width of the P_T^{truth}/P_T distributions, as shown in figure 4.12 (d) is an order of magnitude larger than that of the energy distributions shown in figure 4.9. This confirms that the P_T reconstruction for TeV scale electrons is much poorer than the energy reconstruction. The width of the distributions in both the barrel and the end-cap increase almost linearly with energy. The uncertainty in momentum measurements is dominated by radiation at low energies and by the resolution of the tracking volume at energies above 200 GeV[2]. This is because radiation is produced in the rest frame of the original electron and boosted into the lab frame. Even though higher energy electrons produce more radiation than their lower energy counterparts, that radiation deviates less from the trajectory of the original electron. The samples of single electrons studied here fall entirely within the high energy regime. As the momentum of an electron increases its associated track becomes straighter and the angular separation between hits on the track becomes smaller. The resolution of the tracking volume remains constant and becomes increasingly

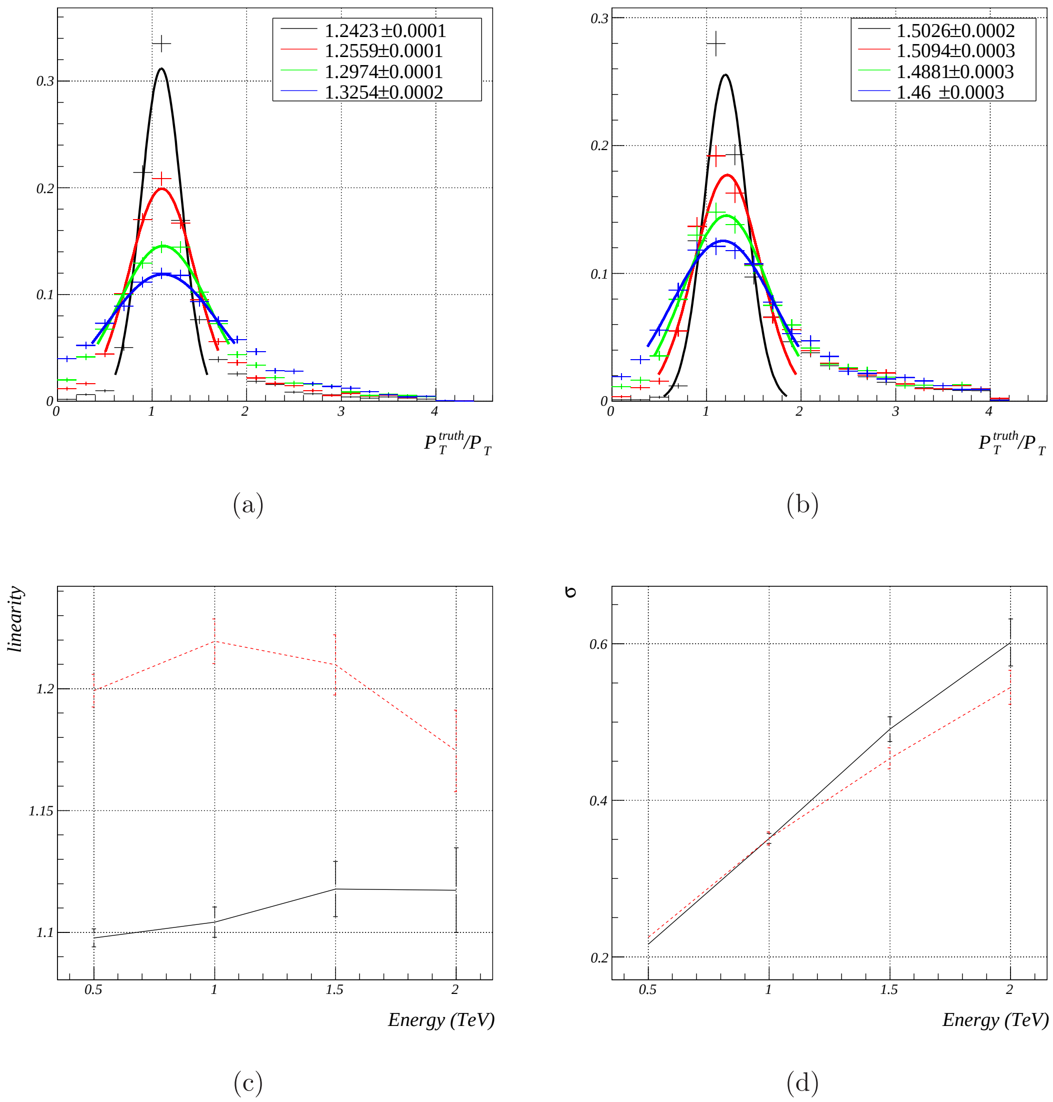

Figure 4.12: Showing the momentum distribution of the highest energy reconstructed electron in each event. The first two plots show P_T^{truth}/P_T for the barrel (a) and end-cap (b) regions of the detector. The distributions for 0.5 (black), 1.0 (red), 1.5 (green) and 2.0 (blue) TeV generated electrons are shown in both plots with fitted Gaussian. The mean of the fits are shown in (c) and the width in (d) for the barrel (black) and end-cap (red) regions of the detector.

large relative to the angular separation between hits as the momentum increases. This means that the linear increase in the width of the distributions shown in figure 4.9 (d) should be expected.

4.8 Summary

The efficiency for single electron event reconstruction in the ATLAS reconstruction software falls as the energy of those electrons increases. This study confirms that, as expected the momentum of electrons as measured from the tracks in the ID is not a useful variable in electron identification at the TeV energy scale. The broad distribution of E/P observed is due entirely to the poor momentum resolution of these TeV energy scale electrons. Track based momentum measurements should be re-interpreted in the study of TeV energy scale electrons. The E/P variable used in electron identification is not appropriate for TeV energy scale electrons. A cut on P above some minimum value could potentially be useful, but this would require further investigation.

5

Micro Black Hole Final State

5.1 Introduction

This chapter details the properties of micro black hole events and the corresponding signal in the ATLAS detector. The implementation of some aspects of the physics behind MBH decay in the Charybdis monte-carlo program is investigated along with the feasibility of measuring the properties of MBH events. Some aspects of the ATLAS reconstruction software present difficulties in the study of MBH events, these are also discussed.

MBH decay via the Hawking Process. They emit radiation in the the form of fundamental particles following an approximately black body thermal spectrum. The Hawking temperature T_H for this spectrum is inversely proportional to the black hole mass:

$$T_H = \frac{1+n}{4\pi R_{BH}} \approx \frac{1+n}{M_{BH}^{1/(1+n)}} \tag{5.1}$$

Any Micro Black Holes produced at the LHC would necessarily have a mass lower than the centre of mass energy of the collision which formed them. This leads to micro black holes with an extremely large Hawking temperature of $\sim 100GeV$ and results in the production of very high energy particle during the decay process. The apparently simple nature of MBH decay is complicated by a number of different theoretical and experimental effects. The theoretical effects, including charge conservation and grey body factors, are discussed in chapter 2. These additional factors will only become apparent in this study if they have been implemented in the MBH monte-carlo simulation which is covered in chapter 3. The experimental effects are those that result from the ATLAS detectors ability to reconstruct those particles emitted during MBH decay. Accounting for these experimental effects involves understanding the detector's response to all the SM particles in a previously unexplored energy regime.

5.2 Generated Event

The formation of MBH and their subsequent decay via Hawking radiation can be simulated using the Charybdis monte-carlo program, as described in chapter 3. The distribution of different particle types produced by the monte-carlo is not that of a simple black body. As discussed in chapter 2 the black body distribution expected from Hawking Radiation is modified by the properties of the MBH. The distribution of different particle types (identified by PDG id number) emerging from the primary vertex in simulated MBH events is shown in figure 5.1. This is equivalent to the distribution of particles emerging directly from the MBH event horizon as a result of the Hawking Radiation process in an MBH event.

Hawking Radiation should lead to the production of all particle types with equal probability. There are actually 8 different particles which are labelled as gluons whilst

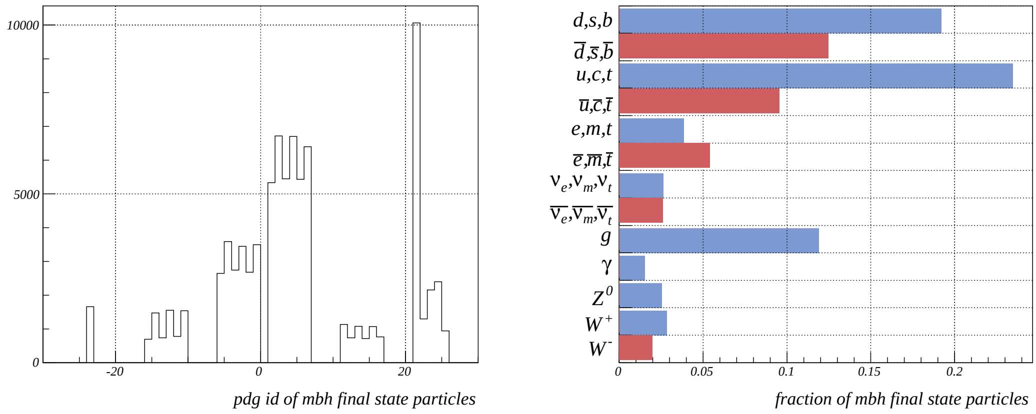

(a) (b)

Figure 5.1: Showing the distribution of particles emitted from the event horizon of simulated micro black holes in a sample of 10 000 such events with mass ranging between 5 and 14 TeV. Figure (a) shows a histogram of PDG id values whilst figure (b) shows the fraction of emitted particles falling into different groups. Figure (b) shows particle and anti-particles in blue and red. Up and down type quarks and anti-quarks have been represented in four separate group. Charged and neutral leptons and anti-leptons have been similarly amalgamated.

each of the other PDG ids show in figure 5.1 correspond to a single particle. This accounts for the large excess of gluons seen in the figure.

As discussed in chapter 2, MBH conserve basic quantum numbers during there decay via Hawking Radiation. These conserved quantities include momentum, angular momentum, electric charge and colour charge[1]. The monte-carlo is able to keep track of all of these quantities and ensures that they are conserved during the decay of a MBH. This contributes to the to the non-uniform distribution of particle types apparent in figure 5.1.

There is a notable asymmetry between quarks and anti-quarks evident in figure 5.1 above. The production of MBH requires very large CoM energies, the simulation used to produce the above results included a cut of 5 TeV on the minimum mass of MBH

[1]The Charybdis monte-carlo program is not currently capable of tracking all the colour charge information in an event. The monte-carlo does conserve the overall sign of colour charge (colour/anti-colour) but not the actual charge (r,g,b).

which has the effect of excluding all collisions with $\sqrt{s}$ less than that energy. Requiring a high $\sqrt{s}$ will usually bias a sample toward high x interactions and therefore select more collisions between valance quarks. The LHC is proton-proton collider so the available valance quarks will all have a positive colour charge. This means that MBH produced at the LHC will most likely have an overall positive colour charge as well. The Charybdis monte-carlo program is able to conserve the sign (but not the colour) of colour charge in MBH decays. The conservation of colour charge sign provides a reasonable explanation for the quark-anti-quark number asymmetry observed in the decay of MBH implemented by Charybdis.

There is also an apparent asymmetry between different electrically charged particles produced in the decays. There are more positively charged anti-leptons than negatively charged leptons whilst the numbers of neutrinos and anti-neutrinos are about the same. There are also more W^+ than W^- emitted by the MBH. This is probably a result of the overall positive charge of the valance quarks contained in proton and the bias toward high x interactions with valance quarks discussed above.

As MBH conserve some of the information associated with the hard scattering process which formed them it may be possible to determine something about that process. Measurements of the boost of the MBH final state as well as the sum of its electric charge may be useful in characterising MBH physics.

5.3 Reconstructed Event

The characteristics of reconstructed MBH events are quite different from those seen in the monte-carlo event generation stage above. Particle detectors are far from perfect in that they don't simply report the exact nature of the physics that occurs in an interaction. The interpretation performed by the reconstruction software, the construction of the detector and the physics that occurs between the IP and its active components will all act to distort the signal produced by MBH events. Comparison between generated monte-carlo events and the results of passing those events through simulations of the detector (and its reconstruction software) can be used to understand those distortions. This can be useful in developing ways of retrieving knowledge of the underlying physics from reconstructed data.

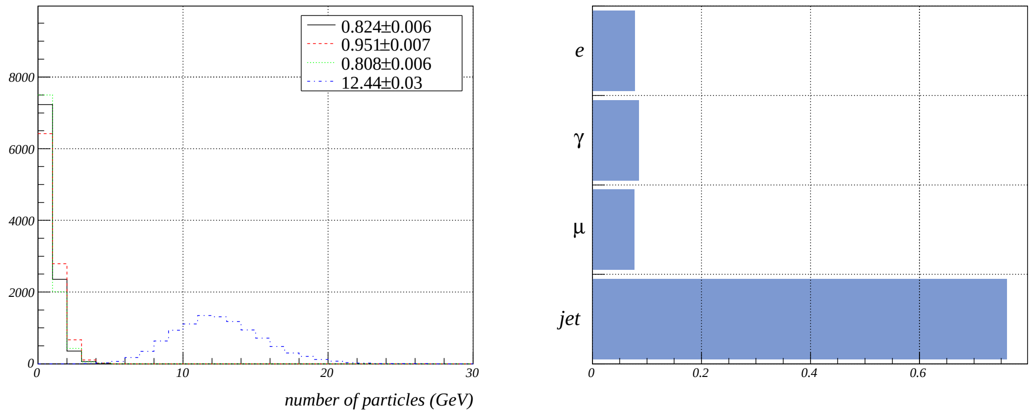

(a) (b)

Figure 5.2: The absolute and relative distributions of reconstructed particles types in the MBH final state for a sample of MBH with a generated mass range of 5-14 TeV. The histograms shown in (a) indicate the number of electrons (solid black), photons (dashed red), muons (dotted green) and jets (dash-dotted blue) reconstructed per event.

The number of electrons, photons, muons and jets reconstructed by the ATLAS detector software from 10 000 fully simulated MBH events are shown in figure 5.2. Only electrons reconstructed using the standard algorithm were included in the plots. Those produced by the *softe* algorithm were ignored. The muon distribution shown came from the *stacoMuonContainer* collection produced by the standard ATLAS reconstruction process. More information is given about the different reconstruction algorithms at the end of chapter 1. The jets from the cone4Tower algorithm. The choice of jet algorithm is discussed in a later section of this chapter. The electrons included in the distributions shown in figure 5.2 were required to pass all of the second stage electron identification tests except the *Track Match and E/P* test which was found to be inappropriate for the high energy electrons produced by MBH events (as described in chapter 4).

Figure 5.2 shows that the number of reconstructed jets is significantly higher than the numbers of other reconstructed particles. This is consistent with theoretical expectation that the ratio of hadronic to leptonic activity in the detector will be approximately 5:1.

5.3.1 Truth Matching

The truth matching algorithm implemented here was intended to find the set of particles in the reconstructed event that best represented the particles contained in the monte-carlo truth. The algorithm was implemented by taking each truth particle in turn and finding the single reconstructed object (particle or jet) which it most closely resembled. Matching was performed by first choosing the set of reconstructed particles with the same type as the monte-carlo truth particle, i.e. electron, photon, muon or jet[2]. The reconstructed particle with the closest four-momentum to the monte-carlo truth was then taken as the matching particle. After a reconstructed particle is matched with one from the monte-carlo truth it is marked as used, preventing a reconstructed particle from being matched with more than one monte-carlo truth particle.

This truth matching was useful for assessing the performance of the reconstruction software when applied to MBH events. Comparing the *matched* reconstructed particles with the monte-carlo truth can be used to determine whether or not individual reconstructed

[2]In the case of the monte-carlo truth particle being a gluon or a quark a suitable match was found amongst the events reconstructed jets

particles are an accurate representation of the individual monte-carlo truth particles. As particles lose energy, change momentum and undergo decay whilst moving through the detector it may be necessary to combine several reconstructed particles to determine the characteristics of a single particle emitted from a MBH. There are also several different algorithms available for the reconstruction of jets, the truth matching procedure can be used to help determine which is most useful for MBH reconstruction.

5.3.2 Jet Reconstruction

Unlike electrons, photons and muons, a jet does not represent a single physical particle. A jet is the result of hadronization from gluons or quarks and typically leaves a much broader deposition of energy than the other reconstructed objects. Jets can be reconstructed using a number of different algorithms, each of which employs a different definition of a jet and leads to different results. Three separate sets of reconstructed jets are produced by the standard ATLAS reconstruction software. Each set of jets is generated by one of three different algorithms. These algorithms are known as the Cone4Tower, ConeTower and KT algorithms. The ConeTower and cone4Tower algorithms employ the same process but use slightly different parameters whilst the KT algorithm uses a different approach. The different algorithms are described in more detail at the end of chapter 1.

As there is a choice of jet reconstruction algorithms available it becomes necessary to select one of them for use in MBH analysis. This can be done by determining which algorithm produces jets that are most representative of the underlying physics as simulated by the monte-carlo program. The truth matching algorithm described above was used to find the jets produced by each of the different algorithms which most closely represent the gluons and quarks contained in the monte-carlo truth. Histograms showing the difference in direction and energy between the monte-carlo truth particles and the jets with which they have been matched are shown in figure 5.3.

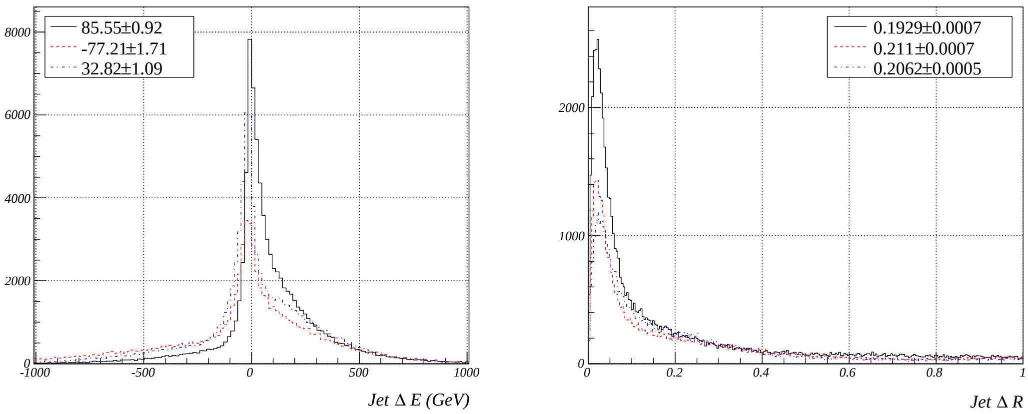

(a) (b)

Figure 5.3: Plots showing how well reconstructed jets produced by the cone4tower (solid black), ConeTower (dashed red) and KT (dot-dashed blue) jet algorithms represent the monte-carlo truth in simulated MBH events. The mean of each distribution is shown in the inset box. Gluons and quarks in the monte-carlo truth have been paired with reconstructed jets produced by each of the algorithms using the truth matching process. (a) shows the energy of each reconstructed jet subtracted from that of the associated particle in the monte-carlo truth. (b) shows the difference in the direction of the reconstructed jets and the associated monte-carlo truth particle R, where $R = \sqrt{\phi^2 + \eta^2}$.

Figure 5.3 (a) shows the energy of the monte-carlo truth particle minus the reconstructed energy of the associated jet. The peak of the cone4Tower distribution (solid black line) falls closer to zero and has a narrower peak than the other two algorithms. However, the mean of the distribution produced by the KT algorithm falls closest to zero. This would indicate that the energy reconstructed by the KT algorithm is closest to the energy of the matched parton. Negative values in the plot would indicate reconstructed jets with energy higher than the matched partons, whilst positive values indicate the opposite. The distribution indicates that the ConeTower algorithm is more likely to produce higher energy jets than the Cone4Tower algorithm. This is because the cone size of the ConeTower algorithm (0.7) is larger than that of the Cone4Tower algorithm (0.4). Jets produced with the larger cone can include more calorimeter cells so achieve higher energies.

The plot shown in figure 5.3 (b) shows the difference R in the direction (in $\phi\eta$ space) of monte-carlo particles and there associated reconstructed jets. The mean of the distribution produced by the cone4Tower algorithm is closest to zero. This indicates that the cone4Tower algorithm produces jets which are closer in R to the matched partons than the other two algorithms.

Both of the distributions shown in figure 5.3 contain more jets from the Cone4Tower algorithm than from the other two algorithms. The ConeTower algorithms larger cone size reduces the number of jets it can reconstruct when compared to the Cone4Tower algorithm. The KT algorithm “grows” clusters in such a way that overlapping jets can be combined with one another (see end of chapter 1), reducing the total number of reconstructed jets. The high multiplicity of MBH events produces a high density of jets in the final state, increasing the chances of jets overlapping and interfering with one another. The small cone size of the cone4Tower algorithm would provide an advantage in this environment and best represent the particles produced by an MBH event. The Cone4Tower algorithm has been used exclusively through out the rest of this work.

5.3.3 Overlap

The ATLAS software employs several separate algorithms in the reconstruction of the individual particles produced during each event. There is an algorithm for electrons and photons[3], one for muons and one for jets. These algorithms do not share results in any way, each one runs over the data generated by the detector and produces an independent list of reconstructed candidate particles. As a result of this design it is possible that the traces left in the detector by a single particle (energy deposits, tracks etc) can be reconstructed several times as separate physical particles. This problem is often referred to as *overlap*.

The strategy for particle reconstruction used in ATLAS is not flawed and is in fact the best way of reconstructing data for use in the majority of particle physics studies. Often an analysis will concentrate on one particle type, at least for event selection purposes. In these analysis it is better to reconstruct a particle more than once than it is to incorrectly identify it as the wrong type of particle. However, the analysis of MBH events suffers greatly from this strategy. The “democratic” nature of MBH decay means that all types of particle are likely to be involved in an event. Operations such as measuring the total mass of an MBH are impossible if some of the particles emitted are counted twice. As a result of these problems it is vital that the overlap be removed from reconstructed MBH events.

The problem of overlap can be resolved by identifying the particles that have been counted twice in an event and then removing all but one of them. The simplest way to do this is to consider the spatial separation between particles that have been reconstructed by different algorithms. Reconstructed particles from different algorithms that have very similar direction can be considered the result of overlap and be removed. The decision over which particles should be removed from a set of overlapping particles is based on a

[3]These are both reconstructed by the same algorithm. First the shower in the EM calorimeter is reconstructed, then if a track is found to match the shower the object is reconstructed as an electron. A photon is reconstructed if no suitable track match exists. See chapter 1 for more details.

simple order of preference. Electrons are preferred over muons which are preferred over jets. This procedure can also lead to the unwanted removal of physical particles which just happen to be close to one another.

Figure 5.4 (a) shows the separation between all pairs of electrons and jets in the $\eta\phi$ plane. Plot (b) shows the same for electron+muon pairs whilst (c) shows muon+jet pairs. All the reconstructed particle distributions include a peak at zero separation whilst the monte-carlo truth distributions do not. All of the distributions show an increase in the number of particle pairs as ΔR increases. This is because the area of a $\delta\theta \times \delta\phi$ bin is proportional to $\sin\theta$ with a maximum at $\pi/2$. As the emission of particles from a MBH is isotropic the number of particle pairs with a separation of ΔR will be proportional to this bin size. The distributions all drop off at ΔR equal to π. This is the maximum separation in ϕ and any separation beyond this value must be in the η direction. For values of $\Delta R > \pi$ the distribution falls off exponentially due to the relationship between η and θ[4]. Placing a cut on ΔR to remove the at peak at low values can be used to reject the particles which have been reconstructed more than once.

The reconstructed (black) distributions in plots (a), (c) and (d) show a local minimum at ΔR approximately equal to 0.4, followed by a sharp rise. This sharp rise after ΔR of 0.4 is present in all the distributions involving jets but not in plot (b) which shows the separation between electrons and muons. This is consistent with the minimum separation of 0.4 between any pair of reconstructed jets. There is no overlap within the jet algorithm, it is written in such a way as to prevent this. The cone size of 0.4 employed by the jet reconstruction algorithm sets the minimum separation between jets. Any reconstructed particle can only be within 0.4 of one single jet, placing it within that jets cone.

[4] $\eta = -ln\left(tan\left(\frac{\theta}{2}\right)\right)$

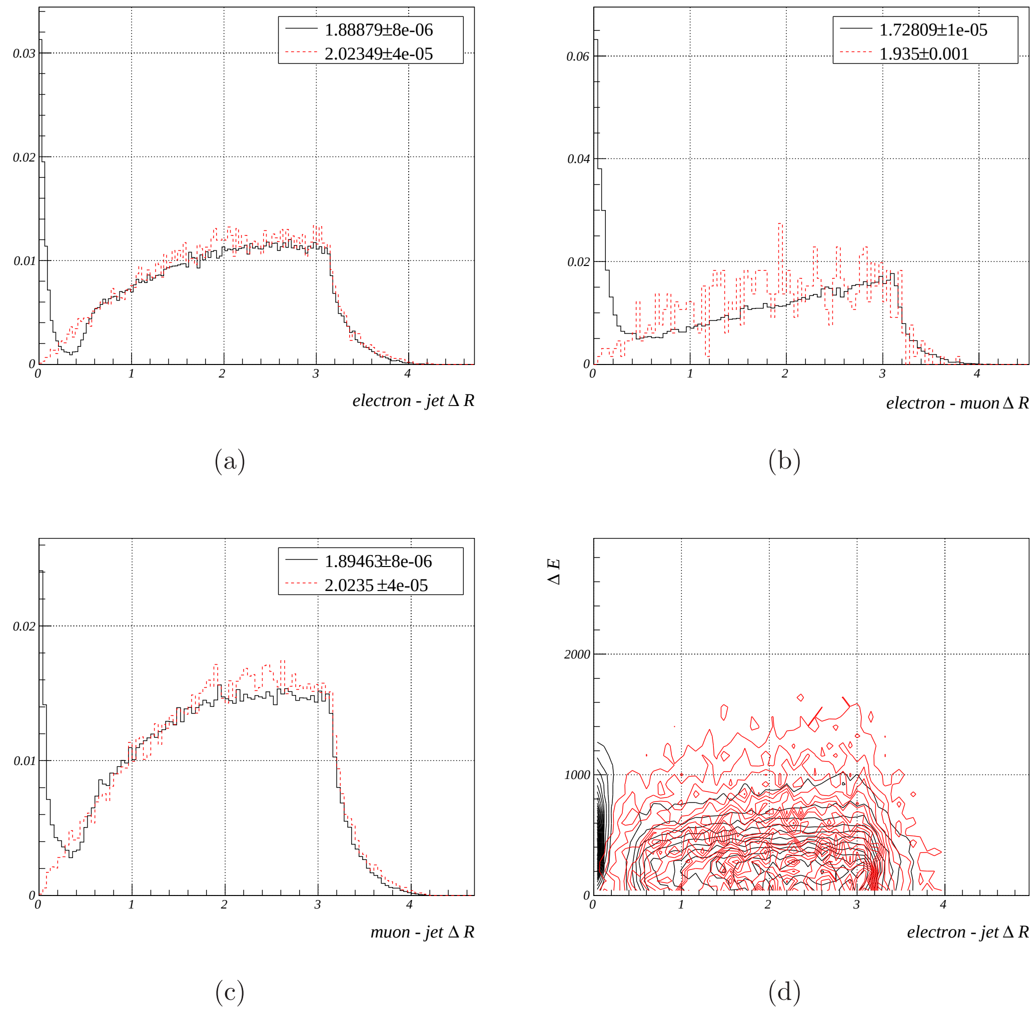

Figure 5.4: Showing the separation between different pairs of particles, ΔR, for a sample of 10 000 simulated MBH events with a mass of 5-14 TeV. (a) shows the separation between every possible combination of electron and jet in each event. The same distributions are shown for pairs of electrons and muons (b) and muons and jets (c). The difference in energy between every combination of electron and jet is plotted against their separation in (d). Each of the plots shows the vales from the reconstructed particles in black and those for the monte-carlo truth in red. The mean and the error on the mean for each distribution is shown in the inset box on each plot.

Figure 5.4 (d) shows the difference in energy, ΔE between all pairs of electrons and jets plotted against their separation, ΔR. The high occupancy in the reconstructed distributions at low ΔR seen in plots (a), (b) and (c) can be seen in this plot to extend over a large range of ΔE. This means that pairs of electrons and jets that are close to each other in space do not necessarily have similar reconstructed energy.

Figure 5.5 shows a comparison between reconstructed electrons and reconstructed jets in samples of simulated single electron events. These are the same samples discussed in chapter 4. The reconstructed jets in these samples are the result of overlap and the distributions shown in the figure can be used to determine suitable parameters for identifying jets that have been reconstructed from electrons. Every single electron event in the samples studied contained at least one reconstructed jet, confirming that electrons with energies above 500 GeV are often reconstructed as jets by the separate jet reconstruction algorithm. The number of reconstructed muons found in the single electron samples was very low, with a total of 7 muons in 10 000 2.0 TeV single electron events.

The distributions in figure 5.5 (a) show that the energy of the reconstructed jets is not very different from that of the reconstructed electrons. The reconstructed energy can also be used to determine the similarity between a reconstructed electron and jet and used to identify those jets resulting from overlap.

Figure 5.5 (b) shows the separation, ΔR between the highest energy reconstructed electron and the highest energy reconstructed jet in each event. The values of ΔR for these electron-jet pairs are much smaller than the 0.4 cone size of the jets. The mean and width of the ΔR distributions also decreases with energy. This could be a result of the increased boost of the higher energy electrons, leading to narrower showers in the ID. The distribution of $\Delta\phi$ in figure 5.5 (d) and the distribution of $\Delta\eta$ shown in (c) become

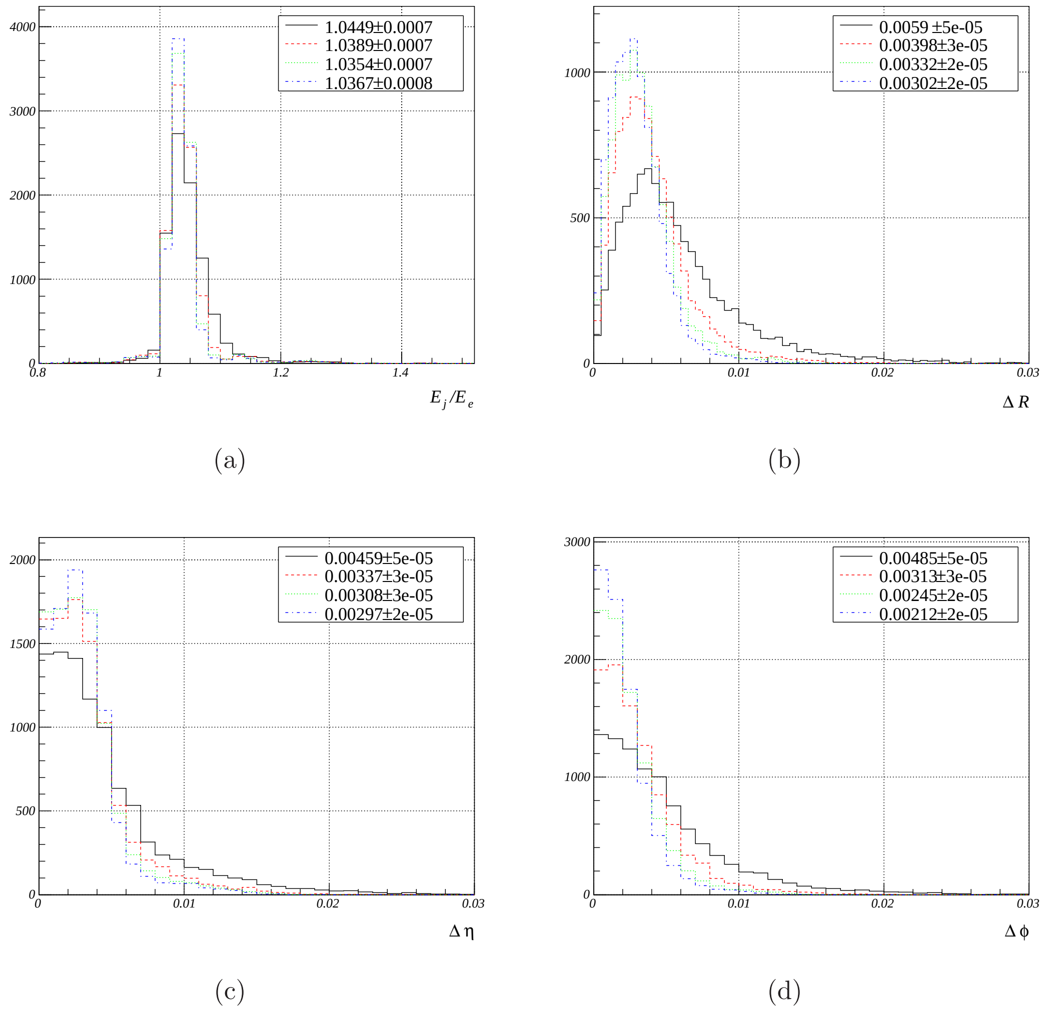

Figure 5.5: Showing a comparison between the highest energy reconstructed electron and the highest energy reconstructed jet in samples of single electron events. The simulated single electron samples used are the same as those described in chapter 4. Distributions are shown for samples of 0.5 (solid black), 1.0 (dashed red), 1.5 (dotted green) and 2.0 (dash-dotted blue) TeV single electron samples. The upper two plots show the ratio of reconstructed jet energy to reconstructed electron energy (a) and the separation, ΔR (b). The lower two plots show the components of ΔR, namely the separation between reconstructed electron and jet in eta (c) and ϕ (d).

overlap	ΔR	E_a/E_b
electron - jet	0.04	0.3
photon - jet	0.04	0.3
muon - jet	0.4	2.0

Table 5.1: Showing a summary of the cuts imposed on pairs of particles in MBH events to remove the effects of overlap.

broader as the generated electron energy decreases. However, the distribution of $\Delta\phi$ shows a greater degree of broadening. This indicates that the increase in separation, ΔR between electron and jet seen with decreasing energy is not caused by the ID's magnetic field alone but that the field does have some effect.

Cuts were imposed on ΔR and the ratio between the reconstructed energies of particles in an effort to remove the effects of overlap from reconstructed MBH events. The values for these cuts were determined for electron-jet pairs using the single electron samples and the plots shown in figure 5.5. The same values were also used for photon-jet pairs because of the similarity in the behaviour of electrons and photons as they pass through the ID. The overlap between electrons and muons was seen to be unimportant by considering the very small number of reconstructed muons found in the samples of single electrons. As a result, overlap between electron-muon and photon-muon pairs was ignored and no overlap related cuts placed on these combinations of particles. Overlap between muons and jets could not be studied in the same way without a sample of single muon events. A cut on ΔR of 0.4 was imposed on jets in the vicinity of reconstructed muons. This is the same as the cone size of the reconstructed jets, insuring that no jet containing a reconstructed muon remained in the reconstructed MBH events. The values of the cuts imposed on reconstructed MBH events to remove overlap are summarised in table 5.1.

Figure 5.6 shows the distribution of reconstructed particles in 5-14 TeV MBH events after the overlap removal cuts have been applied. These distributions can be directly compared with those in figure 5.2 which show the distribution of reconstructed particles in the same events before the overlap removal process has been applied. The overlap removal process has reduced the mean number of reconstructed jets per event by approximately 0.5.

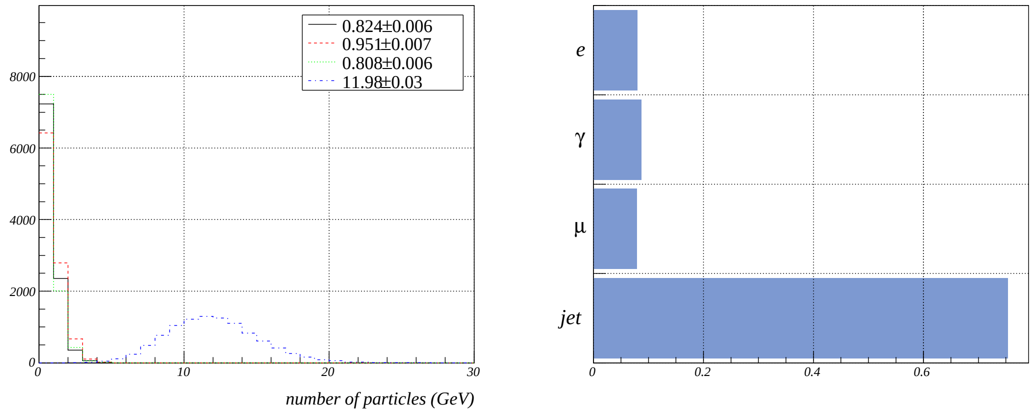

(a) (b)

Figure 5.6: The absolute and relative distributions of reconstructed particles types after the overlap removal cuts have been applied for a sample of MBH with a generated mass range of 5-14 TeV.The histograms shown in (a) indicate the number of electrons (solid black), photons (dashed red), muons (dotted green) and jets (dash-dotted blue) reconstructed per event.

5.4 Sum E_T and Missing E_T

Micro Black Hole events generate a large number of very energetic particles. As a result, the total amount of energy deposited in the detector by these events is very large. MBHs do not conserve lepton number as they decay (at least not in the monte-carlo program used during this analysis). This, combined with the democratic nature of MBH decay (see chapter 2) means that neutrinos are produced just as readily as any other uncharged particle. Neutrinos are also produced in MBH events through secondary decays of other particles such as $W^{\pm}$ and Z^0. Neutrinos are effectively invisible to the ATLAS detector. The large fraction of neutrinos produced in MBH events leads to large amounts of missing energy. This can be observed to some degree after reconstruction by summing the momenta of all the particles in an event. As momentum is conserved, the total transverse momentum of all the particles in an event should be zero. A non zero total transverse momentum for an event must mean that some of the particles emitted during that event were not detected. The magnitude of the missing transverse momentum is the missing E_T. Figure 5.7 shows the $\sum E_T$ (a) and missing E_T (b) distributions for a sample of simulated MBH events.

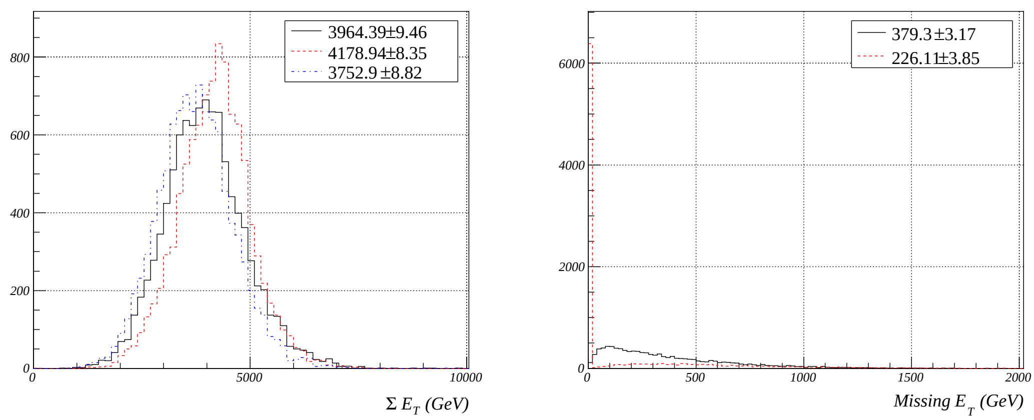

(a) (b)

Figure 5.7: Showing the $\sum E_T$ (a) and missing E_T (b) distributions for a sample of 10 000 MBH events with a mass range of 5-14 TeV. Each plot shows the value obtained from the reconstructed event (solid black) and the equivalent value from the monte-carlo truth (dashed red). Plot (a) also shows the reconstructed $\sum E_T$ after the overlap removal process has been applied (dot-dashed blue). The monte-carlo truth $\sum E_T$ was calculated by summing the transverse energy of all the particles emitted from the simulated event horizon, excluding the neutrinos. The monte-carlo truth missing E_T was calculated by summing the transverse component of the momenta of all the neutrinos emitted from the simulated event horizon.

The reconstructed $\sum E_T$ distribution shown in figure 5.7 (a) (solid black line) was produced by summing the transverse energy of all the reconstructed particles in each event. The monte-carlo truth distribution was produced by summing the transverse energy of every visible particle emitted from the simulated MBH event horizon. This summation excluded any emitted neutrinos. The mean of the reconstructed distribution is approximately 200 GeV higher than the distribution after overlap removal. The means of both the reconstructed distributions are lower than the mean of the monte-carlo truth distribution.

The missing E_T distributions shown in figure 5.7 (b) indicate that the reconstructed missing E_T is much larger than the monte-carlo truth. The monte-carlo truth value was calculated by summing the momenta of the neutrinos emitted directly from the simulated event horizon. The difference between the reconstructed and monte-carlo truth distributions could be caused by the decay of particles into neutrinos. The mean of the monte-carlo truth distribution is approximately 2/3 of that from reconstruction. Considering the branching ratios $W^{\pm}$ and Z^0, direct decays of these particles from the event horizon should produce enough neutrinos to make up half of the deficit[5]. The difference could also be caused by mistakes in the reconstruction software leading to inaccurate values of missing E_T. However, providing that reconstruction is correct, the reconstructed missing E_T should always be equal to or less than the actual missing E_T. This is because invisible particles may be emitted in different directions and have components of momenta which cancel each other out. A further investigation of the final stage of the monte-carlo truth could potentially determine the cause of the discrepancy seen in figure 5.7 (b).

[5]Branching ratio for $W^{\pm} \rightarrow l\nu$ is $\sim$ 30%, whilst that for $Z^0 \rightarrow \nu\nu$ is $\sim$ 20%. This means that approximatly 15% of the energy emitted in $W^{\pm}s$ and 20% of that in Z^0s will be transferred directly into neutrinos. Considering the relative numbers of neutrinos, $W^{\pm}$ and Z^0 shown in figure 5.1, the energy in neutrinos produced by the decay of $W^{\pm}s$ and Z^0s should be about half that in neutrinos produced directly from the event horizon.

5.5 Mass Reconstruction

As Micro Black Holes decay they produces a large number of highly energetic particles. Calculating the invariant mass of an MBH event involves summing the four momenta of all the particles produced, as shown in Equation 5.2. The difficulty in this operation lies entirely in deciding which momenta should be included in the summation.

$$M_{BH}^2 = \left[\sum E_i\right]^2 - \left[\sum P_i\right]^2 \tag{5.2}$$

The truth mass of each event was calculated by finding the invariant mass of particles leaving the the first vertex as listed in the monte-carlo truth section of the event record. These entries in the truth represent a direct copy of the list of particles generated by the monte-carlo program which are subsequently hadronized by Herwig. They represent the particles produced as a direct result of the Hawking radiation process and can be thought of as originating on the event horizon.

As stated in chapter 2 the process of Hawking radiation produces all particles with equal probability. This includes particles which may be completely undetectable. As a result it is useful to derive a true visible mass for each event. This can be achieved to by removing the four momenta of any neutrinos emitted by the black hole before calculating the true mass. However, subsequent decays of particles passing through the detector can also produce neutrinos. This means that the visible mass calculated from the MBH's event horizon will still be greater than the invariant mass of particles measured by the detector.

Figure 5.8 shows the distribution of MBH mass as calculated from the monte-carlo truth and the reconstructed event. Figure 5.8 (a) includes the distribution of recon-

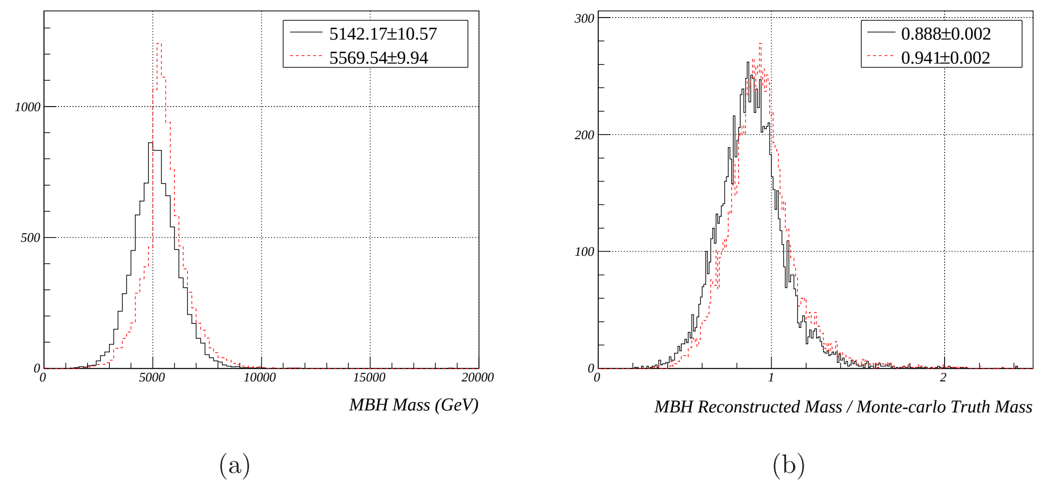

Figure 5.8: Showing the mass of MBHs as calculated from the monte-carlo truth and the reconstructed event. The invariant mass of the reconstructed MBH event (solid black line) and those monte-carlo truth particles that would be visible to the detector (dashed red line) are shown in (a). The invariant mass of the reconstructed MBH event divided by that of the monte-carlo truth (solid black) and the visible monte-carlo truth (dashed red) particles is shown in (b).

structed MBH mass, after the initial cuts and overlap removal process discussed above has been applied. Plot (a) also shows the invariant mass of the visible monte-carlo truth particles as emitted from the simulated MBH event horizon. The reconstructed mass has a broader distribution than the monte-carlo truth, which is to be expected. The mean of the reconstructed distribution is also approximately 400 GeV lower than the visible monte-carlo truth. This shows that, even after removing the invisible particles from the MBH's decay some energy is still lost between the simulated event horizon and the end of the reconstruction. Figure 5.8 (b) shows the reconstructed mass divided by the invariant mass of all the monte-carlo truth particles as well as the mass of the visible monte-carlo truth particles. The plot shows that the visible monte-carlo truth mass is closer than the total monte-carlo truth mass to the reconstructed mass.

The mass of an MBH is not fixed and the range over which it can vary is not well defined by the theory. This makes it difficult to asses the success of mass reconstruction without a good understanding of the generated mass. When analysing potential MBH events in real data it will be desirable to estimate the mass of MBH, including the energy lost to invisible decay products. The mass of potential MBH events must be compared to their cross section. This can be used to ascertain whether the events are actually the result of MBH production. Figure 5.7 (b) on page 107 shows that the mean of the missing E_T distribution for MBH events is approximately 380 GeV. The missing E_T will always be an underestimate of the energy lost to invisible particles, as discussed above. However, the missing E_T could potentially be incorporated into the mass reconstruction procedure for MBH. This would require further analysis before its feasibility is understood.

5.6 Summary

MBH events are identified by very large ΣE_T and missing E_T combined with an isotropic distribution of particles of all types. The minimum energy cut-off presented by the theory means that MBH events must necessarily have very high energy. The proton-proton beam employed by the LHC combined with the distribution of momenta between the quarks in the proton leads to a bias towards MBH events with an overall positive electric and colour charge.

The reconstruction process does not reproduce the properties of the underlying physics event but several steps can be taken to remedy this. The hadronic activity produced by MBH events is best represented by reconstructing jets using the a cone algorithm with a cone size of 4 as described above. Reconstruction can lead to some particles in an event being counted more than once, an effect referred to as overlap. The artifacts of overlap can be removed to some degree by placing a cut on the separation between reconstructed particles in the $\eta\phi$ plane.

6

Event Selection And Efficiency

6.1 Introduction

The experimental nature of Micro Black Hole events has been described in chapter 5. A study of MBH physics requires that those events are identified and separated from the products of other physics processes. This *event selection* will necessarily be based on the the characteristics of events found in real data produced by the ATLAS detector. A set of selection criteria which can be used to separate MBH events from other, *background* physics processes can be identified. This is done by studying monte-carlo simulations of both the signal and background samples.

The selection criteria used to separate signal from background events will not be perfect. There will always be the possibility that signal events are incorrectly discarded or backgrounds falsely identified as signal. For this reason it is necessary to measure the *efficiency* of any event selection criteria. Determining the efficiency allows the cross section of signal events to be calculated from physics data.

MBH events are quite different from any process in the SM. As a result the background to these events is expected to be small. Background samples were chosen to maximise the similarity with the MBH signal.

This chapter details the possible physics processes which could mimic MBH events and develops ways to remove the effects of these backgrounds from particle physics data.

6.2 Potential Backgrounds

A study of potential backgrounds to a micro black hole signal were made using Herwig and the ATLFAST fast simulation of the ATLAS detector, as described in chapter 3.

The ATLFAST software provides a less accurate but less computationally intensive simulation of the ATLAS detector than the full simulation. This fast simulation was used to provide an approximate idea of the standard model physics processes that might be comparable to MBH events. The results of this investigation were used to determine the background samples that were to be generated by the ATLAS collaboration using the full simulation software as part of a larger computing effort.

6.2.1 Signal Sample

A sample of 10000 micro black hole events was produced using the Charybdis monte-carlo program and the ATLAS fast simulation. The sample was used for comparisons with the potential background samples.

physics process	cross section (PB) for min P_T (TeV)			
	0.1	**0.2**	**0.5**	**1.0**
$t\bar{t}$	250.9	65.46	1.622	2.968×10^{-3}
$W \rightarrow ll + jets$	298.4	27.94	0.5783	1.460×10^{-2}
$Z \rightarrow \nu\bar{\nu} + jets$	104.6	10.57	0.2221	5.508×10^{-3}

Table 6.1: Summary of the background samples generated using the ATLAS fast simulation and used for comparison with the MBH signal sample. Samples of three different physics processes with minimum P_T of 0.1, 0.2, 0.5 and 1.0 TeV were produced. Each sample was generated with Herwig and contained 10000 events. The values for cross section were calculated by Herwig and are given in pico barns (PB).

6.2.2 Background Samples

A number of different physics processes were generated using Herwig and passed through ATLFAST. These processes were chosen largely because of particularly high transverse energy, ΣE_T and missing E_T. Table 6.1 contains a summary of the three different background samples along with the cross section of each process combined with a minimum P_T cut.

Micro black hole events produce a relatively large number of high energy particles compared to processes in the SM. The minimum P_T cut was used to increase the number of high energy events in the background samples. This in turn increased the number of events in each sample with properties comparable to MBH events.

6.2.3 Other Sources Of Background

given the nature of micro black hole events the major source of backgrounds or *fake* signals may not come from standard model physics.

Supersymetric physics events present a possible background which could appear much more similar to MBH than any SM process available.

Artifacts of the particle collider environment may prove the most troubling source of backgrounds. Reconstructed events with very large ΣE_T and large missing E_T could result from parts of the beam leaving the beam pipe as a result of instabilities in the beam etc.

6.3 Micro Black Hole Identification

Micro Black Hole events have a number of very prominent distinguishing features, including high sum E_T, large missing E_T and a spherical, isotropic distribution of particles.

6.3.1 Sum E_T

This is the total transverse energy produced by an event and is calculated by summing the transverse energy of every reconstructed particle contained in that event.

6.3.2 Missing E_T

Particle physics events are assumed to conserve momentum in the production of particles. However, the sum of the momentum of all the reconstructed particles in an event is not always zero. This can be the result of particles passing through dead regions of the detector or miss calibrations of active components in different regions of the detector. The production of SM neutrinos or potentially other exotic particles can also lead to a non-zero sum of particle momentum. The magnitude of the sum of an events momentum is called the *missing energy* and is a measure of how much energy may be absent from the reconstructed event. The missing transverse energy is just the magnitude of the competent of missing momentum perpendicular to the beam line.

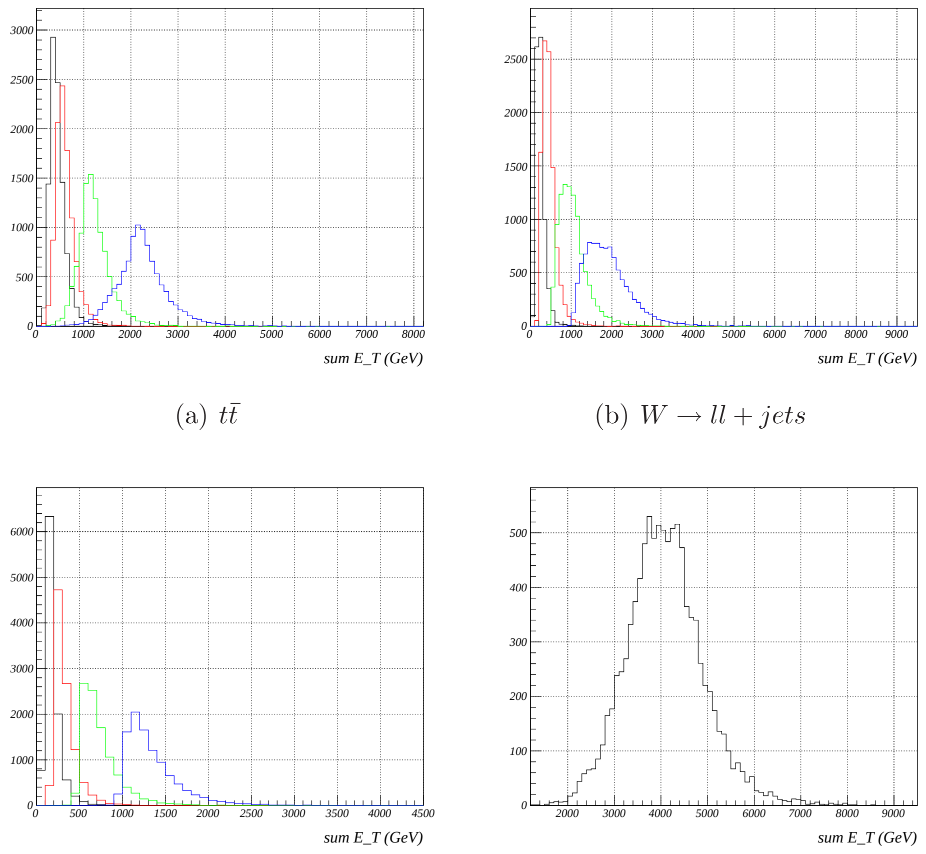

(a) $t\bar{t}$

(b) $W \rightarrow ll + jets$

(c) $Z \rightarrow \nu\nu + jets$

(d) MBH

Figure 6.1: Showing the sum of transverse energy (ΣE_T) in samples of (a) $t\bar{t}$, (b) $W \rightarrow ll + jets$, (c) $Z \rightarrow \nu\nu + jets$ and (d) micro black hole events. The black, red, green and blue plots represent samples with minimum P_T cuts at 0.1, 0.2, 0.5 and 1.0 TeV respectively. The MBH sample has a mass range of 5-14 TeV.

The missing E_T of MBH events is again relatively large when compared to SM processes and may provide a good way of identifying these events.

6.3.3 Event Shape Sphericity

The geometric properties of an event can be characterised by a set of *event shape variables*. These variables are determined by the distribution in θ and ϕ of all the reconstructed particles in an event as well as the their momentum and the separation between those particles. The most commonly used event shape variables in high energy physics are sphericity, thrust and the fox-wolfram moments. A set of algorithms were written to calculate these event shape variables for events in the ATLAS detector. The sphericity variable proved to be the most useful in the study of MBH events.

The sphericity of an event describes how evenly reconstructed particles are distributed in θ and ϕ. A sphericity of one would indicate and event with a completely isotropic distribution of particles. The maximum achievable sphericity will be limited by the acceptance of the detector.

Micro Black Hole events have an unusually high sphericity. This is because of the nature of Hawking radiation and the very high numbers of particle produced in MBH decays.

The Sphericity calculation implemented in this analysis was based loosely on the implementation employed by Pythia. Three eigen values are calculated from the matrix generated by equation 6.1 by diagonalising it using a routine provided by the CLHEP library[19].

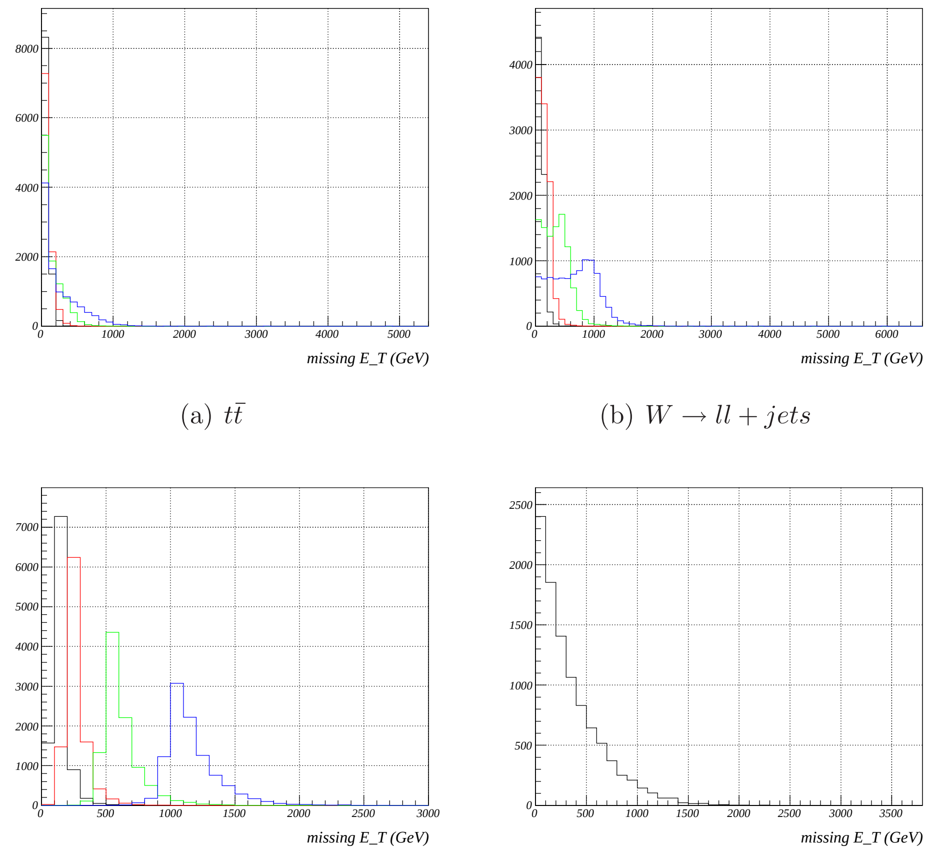

(a) $t\bar{t}$

(b) $W \rightarrow ll + jets$

(c) $Z \rightarrow \nu\nu + jets$

(d) MBH

Figure 6.2: Showing the missing E_T distributions for samples of (a) $t\bar{t}$, (b) $W \rightarrow ll + jets$, (c) $Z \rightarrow \nu\nu + jets$ and (d) micro black hole events (d). The black, red, green and blue plots represent samples with minimum P_T cuts at 0.1, 0.2, 0.5 and 1.0 TeV respectively. The MBH sample has a mass range of 5-14 TeV.

$$M = \Sigma_i \begin{bmatrix} P_x P_x & P_x P_y & P_x P_z \\ P_y P_x & P_y P_y & P_y P_z \\ P_z P_x & P_z P_y & P_z P_z \end{bmatrix} \cdot \frac{1}{\Sigma P^2} \tag{6.1}$$

The three eigenvalues are labelled according to there relative size and obey certain restrictions, as shown in equation 6.2.

$$\begin{aligned} \lambda_1 \geq \lambda_2 \geq \lambda_3 \\ \lambda_1 + \lambda_2 + \lambda_3 = 1 \end{aligned} \tag{6.2}$$

The sphericity is then calculated using the first two eigenvalues, as described in equation 6.3 bellow.

$$S = \frac{3}{2}(\lambda_1 + \lambda_2) \tag{6.3}$$

6.4 Summary

A preliminary study of potential backgrounds to MBH events was performed using samples of simulated data generated with the Herwig and the ATLFAST software. The results were contributed to discussions held with the ATLAS Exotic physics group on the production of shared background samples that might be useful to the majority of group members. As a result of these discussions it was decided that samples of $W \rightarrow ll + jets$ events that were already scheduled for production would be suitable as background for MBH events. Unfortunately, these samples were not produced in time to be included in this study.

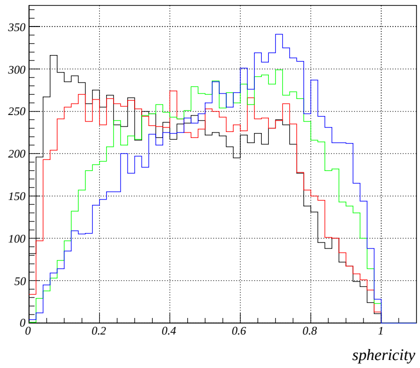

(a) $t\bar{t}$

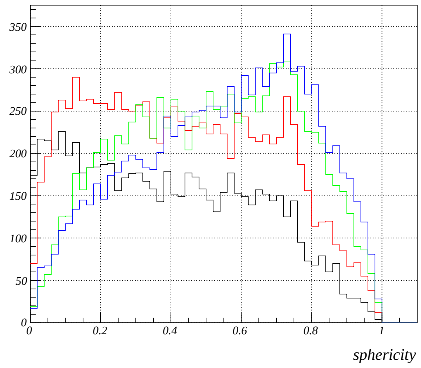

(b) $W \rightarrow ll + jets$

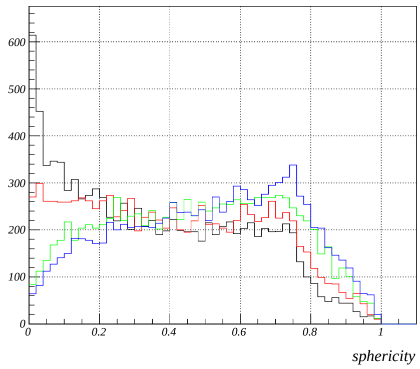

(c) $Z \rightarrow \nu\nu + jets$

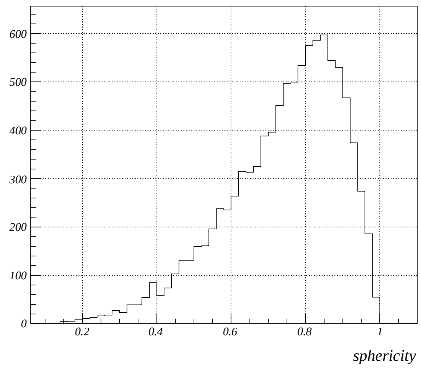

(d) MBH

Figure 6.3: Showing the sphericity distributions for samples of (a) $t\bar{t}$, (b) $W \rightarrow ll + jets$, (c) $Z \rightarrow \nu\nu + jets$ and (d) micro black hole events. The black, red, green and blue plots represent samples with minimum P_T cuts at 0.1, 0.2, 0.5 and 1.0 TeV respectively. The MBH sample has a mass range of 5-14 TeV.

Part II

X-ray Survey Of The ATLAS SCT

7

An X-ray Survey Of The ATLAS SCT

7.1 Introduction

The purpose of the tracking system in any particle physics experiment is to determine the path taken by the charged particles which pass through it. The tracking system in the ATLAS detector is made up of several separate sub-systems (chapter 1), one of which is the Semi-Conductor Tracker (SCT).

When a charged particle passes through one of the SCT silicon modules it interacts, creating electron-hole pairs in the semi-conductor. The data returned from a module after such an interaction can be interpreted to reveal the coordinates of the interaction in the module. This information is referred to as a hit. The SCT has been designed so that a charged particle leaving the experiment's interaction point will pass through > 4 of these silicon modules. Tracking software can be used to determine the path of the particle through the SCT by fitting an appropriate function to the hits recorded by each of the silicon modules through which the particle passed. This fit, along with the position of the hits and other appropriate information, is called a *track*. The ATLAS particle detector includes an approximately uniform 2 T magnetic field in the tracking volume. The field causes charged particles to follow a helical path in the ID. The curvature of a charged particle's track can be combined with a good knowledge of the magnetic field to reconstruct the particle's momentum. This measurement is an important variable in many different analysis of particle physics processes.

The error in a reconstructed track is determined in part by the error in the hit coordinates returned by the SCT. The silicon modules have been constructed with a precision which satisfies the physics requirements placed on the accuracy of the reconstructed tracks. However, the process by which modules are attached to the SCT's support structure cannot be so precise. As a result it is necessary to measure the positions of the modules after they have been mounted. The shape of the SCT's support structure and the position of the modules on it are also likely to change during the construction and operation of the SCT. The requirements placed on the SCT mean that the relative positions of the SCT modules must be measured during construction and operation of the ATLAS detector.

The X-Ray Tomography system has been designed to measure the relative positions of the active detector components in the ATLAS SCT. This survey of the SCT was to be carried out during the final stages of the SCT's construction. Operational requirements for the SCT place stringent requirements on the accuracy of the module positions. The tolerances on the positioning of the SCT modules is summarised in table 7.1 below. The error in each modules position is measured in z (deviation along the barrels axis), r (deviation perpendicular to the barrels axis) and $r\phi$ (deviation in ϕ times position in r).

SCT section	rφ	r	z
barrel	$12\mu m$	$100\mu m$	$50\mu m$
end-cap	$12\mu m$	$50\mu m$	$200\mu m$

Table 7.1: Summary of the required accuracy in the known relative positions of silicon modules when mounted on the SCT support structure.

The x-ray survey is one of several procedures proposed to determine the alignment of modules in the ATLAS SCT. These are the software based track alignment, the real-time hardware based FSI measurement and the x-ray survey.

ATLAS will make use of one or more track based alignment procedures. These procedures are common place in particle physics and represent a tried and tested mechanism for accurate determination of detector alignment. A large amount of data is collected during the normal physics operation of the detector. Tracks reconstructed using this data can then be studied for systematic deviations from their expected trajectories. The alignment algorithm will attempt to identify modules in which hits are always displaced from their associated track by a similar vector. These modules are likely to be misaligned and the information about the position of such modules can be changed to reflect this. The ATLAS collaboration expects to get the most useful track based alignment information from a global chi squared algorithm which takes into account all the degrees of freedom of every module in the SCT, varying the alignment parameters until it produces the best set of tracks from a large data set. The track based alignment procedures are expected to produce the most accurate measurements of the SCT module positions but require a large amount of data to do so. The requirement of a relatively large data set limits the track based alignment mechanisms to a relatively poor time resolution as it takes time to acquire the necessary data set. They are also insensitive to certain kinds of systematic problems.

The construction of the SCT includes a hardware based optical alignment system. The Frequency Scanning Interferometry (FSI) system consists of a tunable laser which can be routed to a network of retro-reflectors mounted to the SCT support structure and the surface of some silicon modules. The retro-reflectors form a geodetic grid within the SCT. The shape of this structure is entirely constrained by the distance between its vertexes. The distance between retro-reflectors can be precisely measured using an interferometric technique which means that changes in the shape of the grid and therefore the SCT support structure can be monitored over time. Changes in the shape of the SCT support structure can then be used to infer changes in the position and orientation of the individual silicon modules. The FSI system does not provide a measure of the absolute alignment of the SCT modules but does identify movement in the SCT during its operation. The complete readout of the ATLAS FSI system should take a significantly shorter time than that required to collect enough data for track based alignment.

An x-ray survey of the SCT would measure the relative positions of the silicon modules immediately after the completed assembly of the SCT This procedure can provide an absolute measurement of the SCT's shape, something which cannot be achieved by either of the other alignment techniques. The survey would not be repeated during the operation of the SCT but the measurements taken would be used in conjunction with the other two alignment techniques.

The three different alignment techniques are designed to compliment one another. The track based alignment should produce the highest precision measurement of the SCT's alignment but requires large data sets whilst the FSI can be used to monitor the changes in the shape of the SCT over short periods of time. However, the track based alignment can potentially converge on an incorrect set of alignment results. This is a particular problem if there are real asymmetries in the construction of the SCT. The measurements produced by the x-ray survey act as a powerful constraint on the fitting process involved in the track based alignment system. An x-ray survey can also be performed in conjunction with an FSI survey of the SCT to provide a precise mapping between the measured positions of the silicon modules (by the x-ray survey) and the shape of the SCT support structure as measured by FSI. The systematics of the combined FSI and x-ray survey are different from those of the track based alignment.

The proposed x-ray survey of the SCT was removed from the ATLAS construction timetable. The decision was made as a result of time constraints caused by delays in construction and has weakened the alignment strategy for the ATLAS detector. However, the techniques and understanding developed during the design and testing of the x-ray survey system may prove useful to future experiments. The work performed has shown that the system could be implemented successfully and has provided invaluable insights into the requirements of any future design.

The x-ray survey system has been designed primarily for use with the barrel section of the SCT. Further proposals exist to survey the two SCT end-caps but have not been developed as far as those for the SCT barrel section. An overview of the proposal for the x-ray survey of the forward section of the SCT is presented in section 7.5 of this chapter.

7.2 Underlying Principles

The ATLAS SCT is composed of 4088 active silicon strip detector modules which have been mounted on a carbon fibre composite support structure. The structure consists of four concentric cylinders, each approximately 1.85m in length which make up the barrel section and 18 wheels with a diameter of 1.14m forming the two forward sections. The

SCT's coordinate system is normally defined in cylindrical polar coordinates. The z-axis runs along the centre of the SCT in place of the beam line. The angle ϕ represents rotation about this axis.

The SCT modules are mounted on this structure and positioned so that they overlap one another. The modules in the barrel section are mounted in rows parallel to the z-axis. The modules in a row are positioned in alternating upper and lower positions. Every other module sits at a slightly larger radius than its two neighbours in the in the row. The ends of these modules overlap one another. The rows are positioned on the barrel such that they also overlap one another in the ϕ direction. One side of each row is mounted below the neighbouring row whilst the other side is above the opposite neighbouring row. The overlap means that there are no gaps in the tracking provided by the SCT. Figure 7.2 is a photograph of the SCT's barrel 3 after completion and shows the layout of the modules as described above. The modules used end-cap sections are slightly different in design from those in the barrel. The strips on the end-cap modules are orientated in the radial direction so the separation between strips varies with r. Figure 7.1 shows the basic layout of the ATLAS SCT support structure upon which the active detector modules are mounted.

Each SCT module has 1536 p-on-n doped strips which are separated by 80 μm. The strips run approximately parallel to the z-axis in the barrel section and in the radial direction in the forward sections of the SCT. The modules are approximately 12 cm long and 6 cm across, consisting of four separate silicon wafers. The wafers are wire-bonded together into pairs, then two pairs of wafers are mounted back to back with a stereo angle of 40 Mrad. A Beryllia support plate is sandwiched between the two pairs, acting as a mechanical support for the silicon and as a thermal conductor. When the modules are

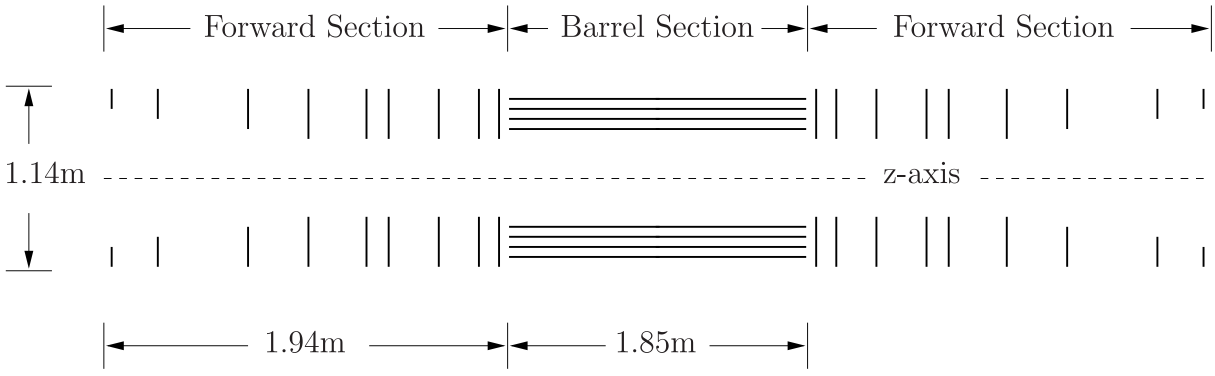

Figure 7.1: Figure showing the layout of the active components of the ATLAS SCT. The figure shows a cross section through the yz plane. The barrel section consisting of four concentric cylinders is shown in the centre surrounding the interaction point. The barrel section is flanked on either side by the two matching forward sections.

mounted onto the SCT support structure and exposed part of the Beryllia plate is placed in thermal contact with a cooling block.

The SCT has a designed operating temperature of −20°C. This temperature maximises the the expected operational lifetime of the SCT in the harsh environment in which it must operate. An evaporative cooling system using a liquid C_4F_{10} coolant is employed to maintain the required temperature.

The silicon strips are read out by a series of eight Application Specific Integrated Circuits (ASIC's) known as ABCD's. Four of these are mounted on each side of the module. The chip's employ a binary readout system. A threshold cut is applied to the charge read out from a strip each clock cycle. A hit is registered when this threshold is exceeded. Only information about strips containing a hit is transmitted out of the module. This mechanism drastically reduces the amount of data transmitted between the SCT modules and external electronics and results in a similar reduction in the amount of cabling required in the detector.

The SCT module readout chips contain a 132 bit first in first out (FIFO) stack. The

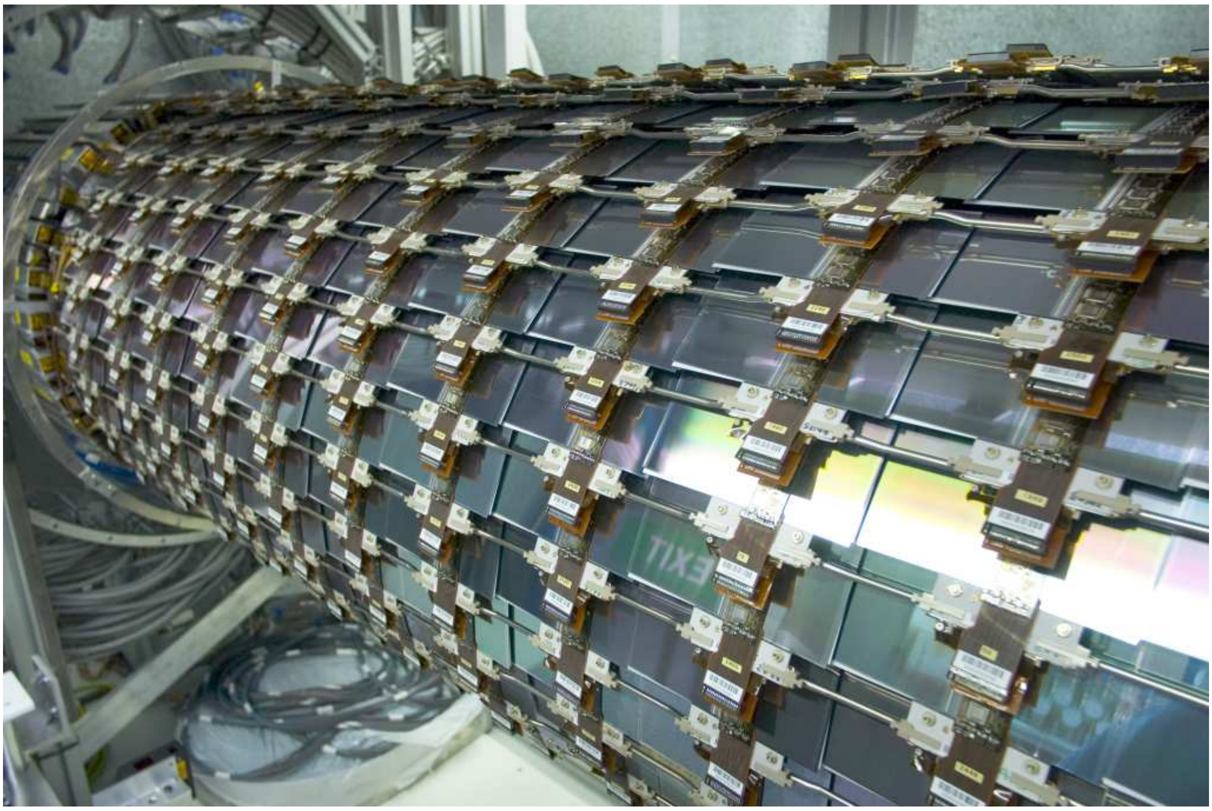

Figure 7.2: Photograph of the ATLAS SCT's Barrel 3 after assembly at Oxford showing the layout of the modules on its surface. The electrical connection of each module is also visible in the photograph, as are the cooling pipes which run along the length of the barrel

stack is used as a buffer which allows the modules to store data from previous bunch crossings. The modules only transmit data for a given bunch crossing when a level 1 accept trigger signal is received. The length of the buffer multiplied by the period of the clock signal determines the maximum time available for the trigger system to make a decision on weather or not to keep an event.

The x-ray survey relies on the fact that the silicon modules that make up the SCT are sensitive to x-rays. A single x-ray beam can pass through many layers of silicon modules and potentially, the position of the beam can be measured by each of the modules in its path. A survey can be carried out by placing an x-ray source within the SCT and directing a number of collimated x-ray beams outward through the silicon modules on precisely known trajectories. The points where the two x-ray beams pass through a module can be used to fix the module's position relative to the beams and therefore its position relative to the beams' source. A precise measurement of the x-ray source's position combined with a measurement of each module's position relative to the x-ray source can be used to produce a map of the relative position of every module in the SCT.

The SCT has been designed to track particles leaving the interaction point (IP) positioned at the centre of the barrel section. The resulting geometry of the SCT (figure 7.1) means that an x-ray survey of the type proposed is best preformed with an x-ray source placed approximately where the IP would be during the operation of the detector. The different geometries employed by the barrel and forward sections of the SCT mean that the survey of each requires a slightly different approach. The survey system for the barrel section of the SCT is almost complete whilst work on the system for the forward section remains in the planning stages.

The proposed x-ray survey of the barrel section described in this work involves a self propelled carriage referred to as the *scanning head* which positions a source of x-ray beams within the structure of the SCT. Figure 7.3 shows a simplified diagram of the scanning head and labels the important components. The scanning head can be positioned on the z-axis and the x-ray tube + collimators rotated through 2π radians in the ϕ using a pair of electric motors. These motors are labelled *linear motor* and *rotary motor* in figure 7.3. These motors along with some additional instrumentation and the structure which supports the scanning head inside the SCT form the positioning system. This system is described in detail in chapter 8. The x-ray source is mounted on the front of the scanning head. The source consists of an x-ray tube and two collimators, all of which are mounted on the rotary positioning stage. The x-ray source requires a number of services, including a High Voltage power supply, water cooling loop and a number of data cables. These services are coiled around the rotary motor and supported away from the scanning head on a telescopic rod, labelled *cable guide* in the figure.

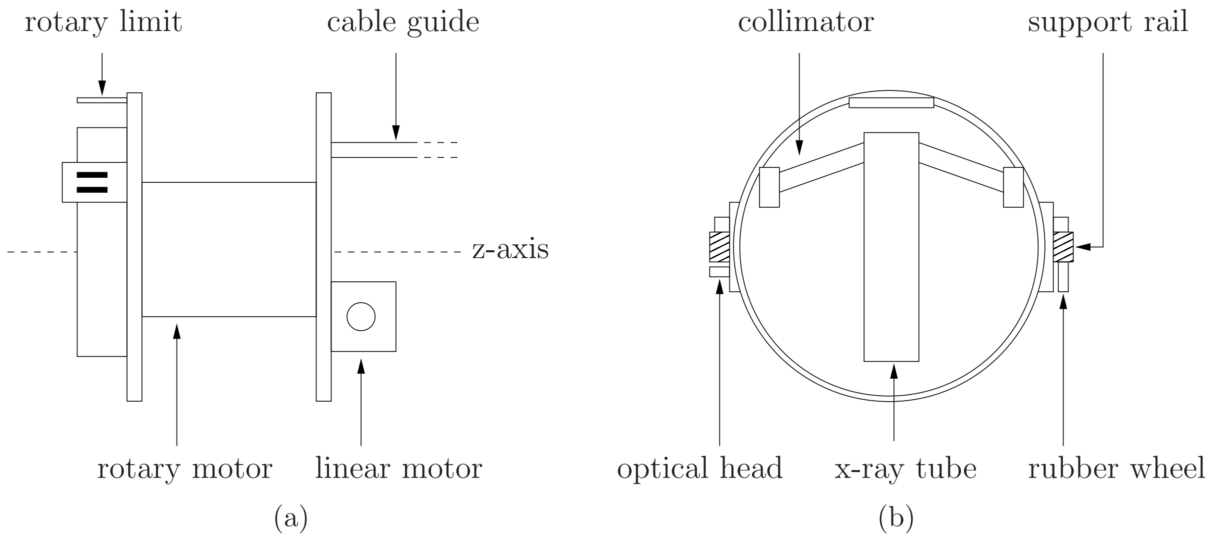

Figure 7.3: Showing a simplified diagram of the x-ray scanning head assembled for the survey of the SCT barrel section. Part (a) shows a view of the scanning head from the side (a projection in the yz plane) whilst (b) shows a view from the front (a projection in the xy plane). (b) also shows the support rails (hashed) which are not part of the scanning head.

The x-ray survey system can be used to measure the position and orientation of a single module. This is done by first locating the x-ray scanning head on the z-axis and rotating the x-ray source in ϕ such that one of the x-ray beams passes through a point on the module. The hits produced by the x-ray beam passing through the module can then be read out. When sufficient hits have been collected to accurately determine the position of the beam in the module (see next paragraph) the read out stops. The x-ray source is then rotated in ϕ by a fixed amount so that the beam passes through a different part of the module and the process is repeated. A number of points on the module are *scanned* in this manner by rotating the scanning head in ϕ and translating it in the z direction. A module's position in r can be determined by scanning it with x-ray beams which emanate from two different points. The position in r can be found by combining these measurements and the separation between the two beam sources, using triangulation. The process of measuring points on a module using the x-ray system was referred to as a *scan*.

The distribution of hits resulting from an x-ray beam passing through a silicon module should be Gaussian about the centre of the beam. The point at which beam and module intersect can be determined by fitting a Gaussian function to that distribution. Each module is divided into two separate detector planes, or sides, as described in chapter 1. The two sides of a module are mounted back to back. The strips on each side run almost parallel but are offset by a small stereo angle. The position of the beam on each side of the module was determined by finding a fit to the distribution. As each side of the module consisted of parallel strips this position could only be known in the $r\phi$ direction. This measurement was labelled as the strip position of the beam in the module. The two strip position measurements were combined with the known stereo angle between the sides of the module to determine the beam's position along the module's z-axis. The number of hits in the distribution will have a bearing on the error in the fitted beam position. The configuration of the modules (see chapter 9) was chosen to ensure that sufficient hits were collected during each measurement.

Software was written to reconstruct the position and orientation of an individual module using data collected during a scan. The software operated under the assumption that each SCT module was a flat plane. An assumption that the x-ray scanning head had been correctly calibrated was also made. The software was designed to reconstruct a module's position by considering the distribution of x-ray hits on its surface from successive measurements. The position of the beam in the module was determined by finding a Gaussian fit to the distribution of hits, as described above. The ϕ position of the x-ray beams and the angle between the beams emitted by the two different collimators as they intersect the module was recorded by instrumentation on the scanning head. The information could be combined to find the location and orientation of the module relative to the scanning head. The ϕ position of a single beam, compared with the beams position in the module identifies the location of a point on the module in ϕ relative to the scanning head. The difference in position between the two collimators when each of the x-ray beams pass through the module can be used to determine its location in r. The module's position can then be determined by finding the best fit to a number of points on its surface.

The algorithm developed to perform this analysis attempts to minimise the difference between the position of the x-ray beam in the SCT's coordinate system and the position in the module's coordinate system. Figure 7.4 summarises the principles behind the reconstruction algorithm. The Minuit[24] program is used to fit a Gaussian function to the hit distributions on the modules surface. The algorithm then iterates over expanded and linearised versions of the equations given in figure 7.4 to find the most likely position of the module relative to the x-ray beams.

7.3 X-ray source

The x-rays were generated using a commercially produced fine focus spot x-ray tube[23]. The tube had a focus spot size of $100 - 400\mu$m and operated with a voltage in the range 20-60kV and a maximum power of 1-2kW. This x-ray tube was powered by a high voltage

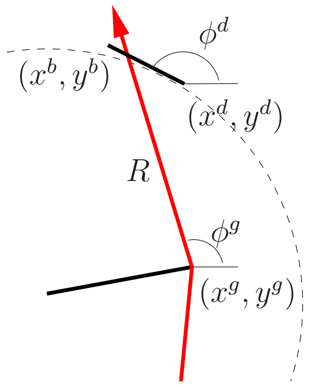

position of beam at detector

$$\begin{aligned} x^b &= x^g + R\cos\phi^g \\ y^b &= y^g + R\sin\phi^g \\ R &= ((x^b - x^g) + (y^b - y^g))^{1/2} \end{aligned}$$

position of detector strip

$$\begin{aligned} x^s &= x^d + ps\cos\phi^d \\ y^s &= y^d + ps\sin\phi^d \end{aligned}$$

find $\mathrm{x^d}, \mathrm{y^d}, \phi^\mathrm{d}$ by minimising

$$\sum_i \left(x_i^b - x_i^s)^2 + (y_i^b - y_i^s\right)^2$$

Figure 7.4: The basic mathematical principles underlying the modules position reconstruction algorithm. Here, x^s, y^s, represent the location of the x-ray beam in the modules coordinates system. In the SCT's coordinate system x^d, y^d, ϕ^d represent the position of the detector module, x^g, y^g, ϕ^g the x-ray source and x^b, y^b, ϕ^b the point where the x-ray beam intersects the module. The remaining variables are the distance between the source and the hit position on the module R, the strip number s and the 80μm strip pitch p.

power supply with maximum output of 50kV, 60mA and 1% stability. The x-ray tube was operated at 40kV with a current of 20mA during all of the work described here. The x-ray tube was cooled by a water jet arrangement which sprayed distilled water onto the back of the x-ray target.

X-ray beams were produced by shaping the output from the focus point of the x-ray tube with two collimators. Each collimator defined a narrow beam for position measurements and a wide beam for calibration purposes. The collimators consisted of a tantalum mask with a 2mm circular aperture followed by a pair of collimator slits. The masks were adjusted using a microscope to ensure that they emitted beams with approximately the same orientation. The collimator slits had widths of 50μm and 300μm for the narrow and wide beams respectively. The collimator slits only determined the beam shape in the $r\phi$

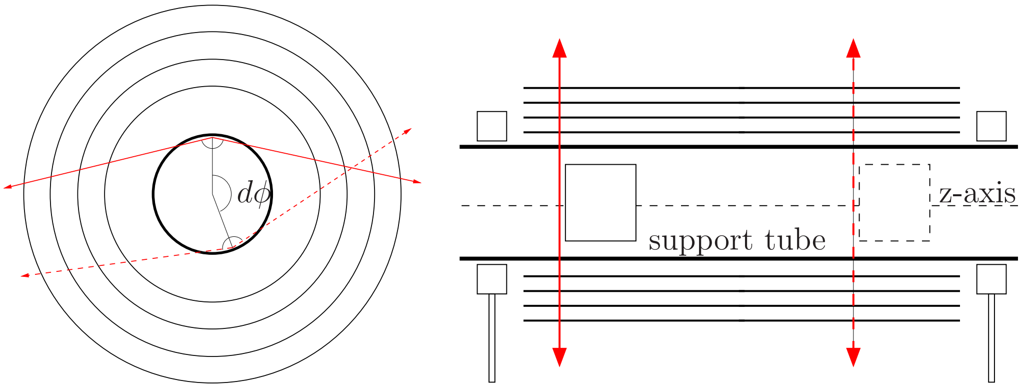

Figure 7.5: Diagram showing the orientation of x-ray scanning head during the survey of the SCT barrel section. (a) shows a projection in the xy plane and describes the movement of the x-ray beams in ϕ. (b) shows a projection in the yz plane and describes the movement of the x-ray beams in the z direction. The four concentric cylinders that make up the SCT barrel section and the x-ray survey support tube are indicated by solid black lines. The solid and dashed red lines show the orientation of the x-ray beams emitted from the scanning head whilst in two different positions.

direction. As a result both the narrow and wide beams were much more extensive in the z direction, leading to a ribbon like beam profile. A more detailed description of the x-ray source can be found in [21].

7.4 Survey of SCT Barrel Section

The barrel section of the SCT is intended to surround the interaction point at the centre of the ATLAS detector. The x-ray survey equipment must be placed inside the completed barrel section during the survey process. The x-ray beams produced by the survey equipment are projected outwards through the active portions of the barrel section, as shown in figure 7.5.

The scanning equipment is designed to emit beams of x-rays in two different directions.

The beams are confined to the xy plane and originate from a point some distance from the z-axis, as shown in figure 7.5. The two beam directions are almost anti-parallel, separated from one another by a small *stereo* angle. This design allows the x-ray beams and the silicon modules to form the kind of geometrical arrangement which allows the position of the modules to be constrained.

7.5 Survey of SCT Forward Section

A similar x-ray survey of the SCT forward sections was also developed using the equipment from the barrel survey with some modifications.

The silicon modules in the SCT forward section are of a similar design to those in the barrel section although the strips are aligned in the radial direction, causing the strip pitch to vary across the module. The forward section's silicon modules are all mounted such that the detector plane is perpendicular to the SCT's z-axis. As part of the survey the x-ray beams produced by the survey equipment would have to pass through the surface of the silicon modules in much the same way as they do in the survey of the barrel section. As a result, the x-ray source should be positioned outside of the SCT forward sections and aligned with its z-axis. The x-ray beams can then be orientated toward the SCT with an acute angle to the z-axis.

The geometry of the forward section survey is presented in figure 7.6 which shows the relative positions of the SCT forward section and the x-ray survey equipment.

The proposed survey of the SCT forward section operates on a similar principle to the survey of the barrel section. The position of several points on the surface of each module is illuminated using a beam of x-rays. Beams coming from two different positions and passing through the same module can then be used to calculate that modules position.

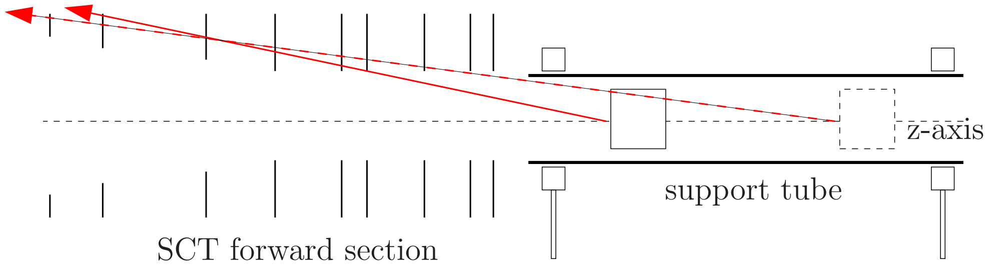

Figure 7.6: A simplified diagram showing the basic geometry behind the proposed x-ray survey of the SCT forward sections. The x-ray scanning head is shown in its support tube on the right hand side of the diagram whilst one of the two forward sections of the SCT is shown on the left. The red lines indicate the trajectories of x-ray beams emitted from the modified scanning head in two different positions.

The survey of the forward section requires a single x-ray beam. The beam is initially positioned at a fixed angle θ from the z-axis, using a set of accurately measured dowels to hold it in place. With θ fixed, the survey equipment is translated through a number of points on the z-axis and rotated through 2π in the ϕ direction at each point. The angle θ is then changed and the process repeated until sufficient data has been collected.

This proposed method for surveying the SCT's forward section has the advantage that the majority of the apparatus needed is in common with that developed for the survey of the barrel section which minimises cost and development time. The method described here is also more accurate than the earlier proposal, which involved fixing the position of the x-ray source on the z-axis and using an additional motor to move the beam through the entire range in θ.

7.6 Summary

An x-ray survey method was designed to measure the position and orientation of every silicon module in the ATLAS SCT. The survey takes place only once, during the construction phase of the ATLAS detector but provides data useful to the alignment of the detector and complimentary to the other proposed alignment procedures.

The survey involves placing a source of x-rays inside the completed SCT and exploits the tracking abilities of the SCT modules to determine the location of the beams produced by the x-ray source as they pass through the silicon modules. This information is then combined with accurate information about the position of the source and used to determine the position of the SCT modules relative to each another.

The construction schedule prevented the system begin used as intended in ATLAS, but the technique has been demonstrated to work well and is a candidate for further detectors, such as the upgraded ATLAS tracker that would be used in conjunction with an upgraded LHC (the proposed SLHC).

8

Positioning System

8.1 Introduction

The x-ray survey procedure required that the scanning head move through the SCT barrel section along the z-axis. The four x-ray beams needed to be rotated through 2π radians in ϕ. The requirements placed on the precision of information about module positions in the SCT (specified in chapter 7 section 7.1) determined the precision required in the measured position of the x-ray beam relative to the SCT support structure.

The x-ray survey system was held in position within the SCT by a specially designed support structure described below. The required movement of the x-ray system within that structure was achieved through two stepper motors mounted on the scanning head. Both of the electric motors were both manufactured by the same company[25] and received power and control signals through the same motor controller [27]. The configuration of the motor control system is shown in figure 8.1.

A large part of the motor control system was incorporated into a PC compatible ISA

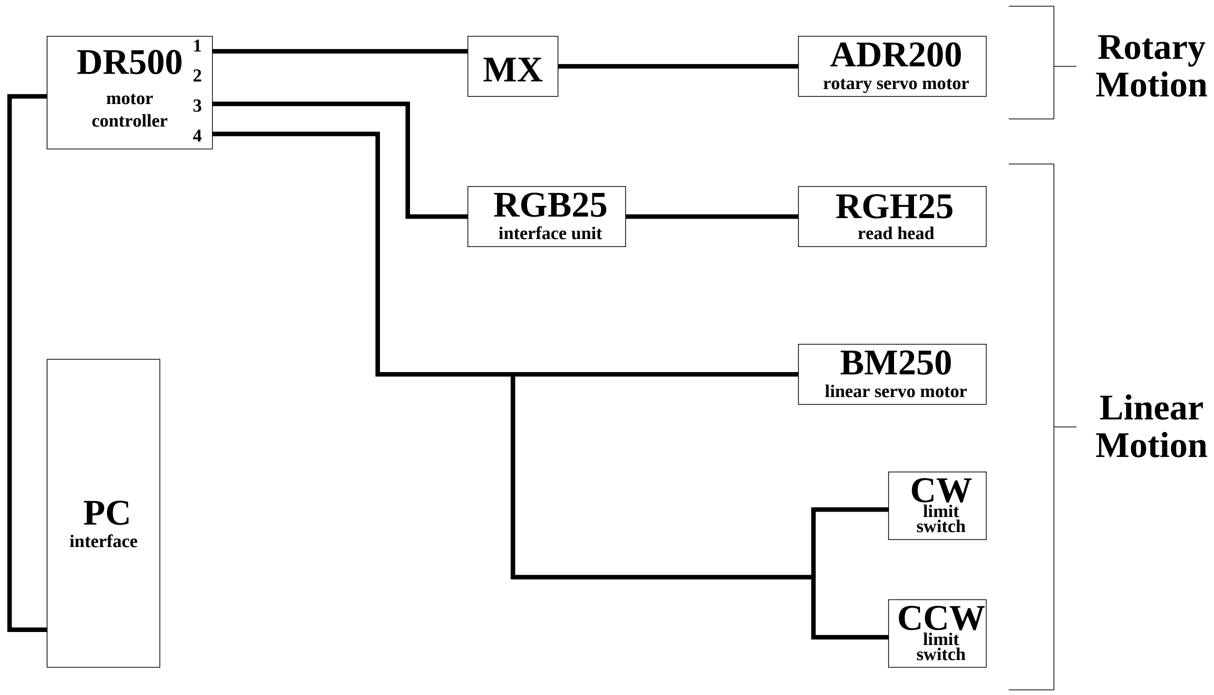

Figure 8.1: Simplified diagram showing the connection between the various components of the x-ray motor control system.

card. The ISA card interpreted commands from software running on the PC and passed the appropriate control signals to the motor controller. The motor controller supplied electrical power to the motors and acted as an interface between them and the ISA card. The electric motors both provided information about the current position of their axis. The feedback provided by each motor was required by the motor control system in order to generate appropriate signals and drive the motors correctly.

The positioning system was divided into two separate sub-systems at the motor controller. The rotary stage consisted primarily of the ADR200 electric motor. A separate set of electronics (named MX decoder) was positioned between this motor and the motor controller. These electronics processed the analogue position feedback from that motor, producing a signal which could be interpreted by the motor controller. The rotary stage determined the orientation of the x-ray beams in ϕ by rotating them about the z-axis. The linear stage included the BM250 electric motor, a pair of limit switches and an optical device for position measurement. This stage translated the scanning head in z. The rotary and linear stages were independent of one another and are described separately below.

The ISA card, motor controller, rotary stage and linear stage motors were all commercially available devices manufactured by the same company, AEROTECH[25], and the components of the positioning system had the product names UNIDEX 500[26], DR500[27], ADR200[28] and BM250[29] respectively.

The rotary and linear stages incorporated measurement systems which were used to determine the orientation of the x-ray beams relative to the scanning head and the position of the scanning head on the z-axis. However, these systems were not sufficient to entirely determine the position and orientation of the x-ray beams relative to the SCT. Additional measurement devices are required and these are described below.

Finally, the entire positioning system was controlled by purpose built software which is described in the last section of this chapter.

8.2 Support Structure

The x-ray survey requires that the x-ray source be positioned inside the SCT. The SCT cannot support the weight of the x-ray scanning head so an independent support structure is required. The relative positions of the SCT and the coordinate system of x-ray survey apparatus must be known throughout the survey. The final design for the x-ray system placed the scanning head inside a support tube which could be inserted into the completed barrel section of the SCT. The support tube was made from two concentric carbon fibre cylinders separated by a layer of foam. The support tube was strong enough to support the weight of the scanning head whilst minimising its effect on the x-ray beams passing through it.

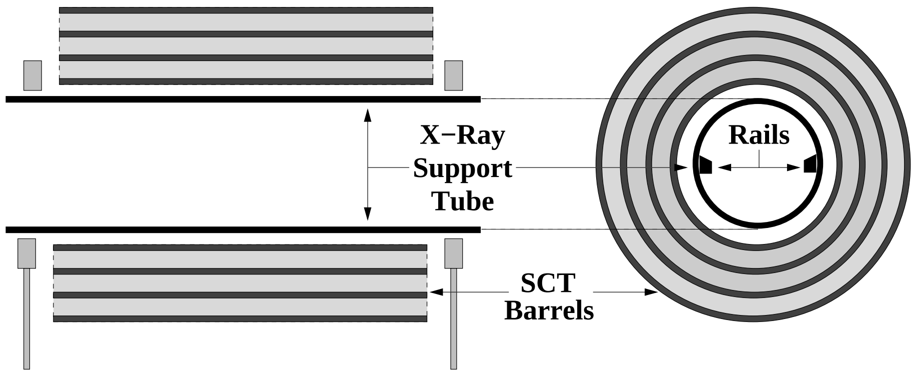

Figure 8.2: A diagram of the support tube used as part of the x-ray survey system. The support tube is shown inside the barrel section of the SCT and is suspended from a structure that remains independent of the SCT. The left hand diagram shows a cross section through the SCT in the yz plane whilst the right hand diagram shows a cross section through the xy plane.

Figure 8.2 shows the x-ray survey support tube positioned within the barrel section of the SCT. The scanning head was designed to rest on a set of rails positioned on opposite sides of the support tube. These rails are shown in the right hand diagram of figure 8.2. The rails run along the entire length of the tube and are an integral part of the support tube. They are made of the same carbon fibre and foam structure as the outer cylinders.

The SCT was designed with an extremely lightweight structure with the aim of minimising the amount of material present in the inner detector. As a result the x-ray survey system had to be supported independently from the the SCT. The carbon fibre part of x-ray support tube was attached to a pair of aluminium collars, one placed at each end. The collars were in turn suspended from a support structure made of steel box section.

8.3 Rotary Stage

The x-ray source and collimators are mounted on a single rotary stage which is driven by a precise stepping motor. The motor's axis can be positioned with a resolution of ~ 1 arc second, which is equivalent to a resolution of $0.16\mu m$ in $r\phi$ at the radius of the outermost barrel of the SCT[1]. The motor also incorporates a measurement device called an encoder which produces a pair of analogue signals which indicate the position of the motors axis. These signals are then interpreted by an external device referred to as a decoder which is capable of resolving the orientation of the motors axis with a precision of 0.36 arc seconds ($0.057\mu m$ at the outermost barrel). The position can then be read by the motor controller and subsequently made available to the ISA card mounted inside the PC. The decoder is produced by the same manufacturer as the rotary stage motor and has the product name of MX decoder [30]

An optical limit switch was used in conjunction with the rotary stage motor. The switch was comprised of two light gates positioned close together on either side of the motors zero position. A strip of metal attached to the rotary stage would pass through both of the gates if the allowed range of the stage was exceeded. The limit switch was designed to disable the rotary stage motor when activated. The ISA card controlling both the rotary and linear motor stages also incorporated a set of user defined software limits on the allowed range of motor positions. The mechanical limit switches acted as a fail-safe backup to these software limits.

The design of the rotary stage was constrained by a series of services which were required by the components mounted on the rotary stage. These included a High Voltage (HV) power supply for the x-ray source and a water cooling loop for the x-ray target.

[1] Radius of barrel 6 is $0.57m$ and 1 arc second is $1/3600$ degrees

Providing rotating connections for these services would have been impractical (especially for the HV power supply) and unnecessary as rotation through 2π radians is sufficient to cover the entire SCT. The final design involved coiling the service cables and pipes around the axis of the rotary stage motor. Sufficient slack was provided to allow the rotary stage to move through 2π radians. The design made it possible to damage the services by rotating the motor through more than 2π radians. This danger made it necessary to incorporate the optical limit switches described above.

8.4 Linear Stage

The scanning head can be moved along the rails by an induction motor mounted on the rear of the scanning head. The motor is coupled to the rails by a simple rubber wheel which presses against the underside of one of the two rails. The precision of the linear stage motor is insufficient for the measurement of translation along the z-axis. The linear stage is also subject to cumulative errors as the motor must undergo many revolutions in order to move the scanning head along the entire length of the SCT. The rubber wheel which connects the axle of the linear stage motor to the support tube rails is also prone to deformation and slipping. These factors mean that the linear motors internal position measurements cannot be used to determine the position on the z-axis and an additional measurement system is required.

The position of the scanning head on the z-axis is measured using a low CTE gold plated strip attached to the underside of one of the support rails and an optical reading device mounted on the scanning head[31]. The strip has marks etched at intervals of $20\mu m$ along its entire length. The optical reading device measures the amount of light reflected from the strip in two places and compares this to an internal threshold value, producing a logical one or zero depending on its amplitude. As a result the device produces two square wave signals as it moves along the the strip, each with a period of $20\mu m$. These signals can be interpolated to produce a measurement of the reading devices position with a resolution of $\sim 5\mu m$. The system also incorporates a hall probe which detects the presence of a small magnet, providing fiducials. Three of these magnets are located along the z-axis of the support tube, under the support rail next to the strip and provide a location accuracy of 7μm.

The signal produced by the optical strip reader and its associated hall probe can be interpreted by the same motor control system used by the rotary and linear stage electric motors. This removes the need for any additional equipment and simplifies the requirements placed on the motor control software. The output from the optical strip reader is connected to the motor controller and to the ISA card mounted inside the PC (figure 8.1)[2]. The motor controller was configured to accept both sets of feedback information and associate them with the linear stage motor. Feedback from the optical strip system was used for motor positioning whilst feedback from the motor was used to determine the orientation of its axis.

A pair of limit switches are installed in the linear stage system. These limit switches are marked clock-wise (CW) and counter clock-wise (CCW) in figure 8.1. These devices are mounted on the front and back of the scanning head and intended to disable the linear stage motor if either of them is opened (electrical connection broken). An aluminium rod is attached to either end of the x-ray support tube and aligned with the limit switches on the scanning head. In the event that the x-ray scanning head moves to the end of the support rails these rods make contact with the CW or CCW limit switches, disabling the

[2]The feedback provided by the linear stage motor is still required by the the motor control system which uses it to generate the correct sequence of signals to drive the motor

linear stage motor and halting the motion.

8.5 Position Measurement

The precision of the x-ray survey is dependant on the precision of the measured position and orientation of the x-ray beams. This measurement includes the location of the scanning head and the the beam's orientation relative to it. The x-ray beam orientation is determined by the rotary stage motor and measured by its integral encoder. The specifications of the rotary stage motor are such that movement other than rotation about its axis is negligible.

The scanning head has six degrees of freedom (DoF) described by translation along and rotation about the x, y and z axis. The optical encoder used in conjunction with the linear stage motor determines the translation along the z-axis but the remaining DoF are undetermined and further measurements are required. Two further measurement systems are used. The first consists of a laser attached to the SCT and a number of solid state optical sensors (CCDs). The beam is directed along the x-ray support tube parallel to the z-axis, passing through a pair of beam splitters mounted on the scanning head, and continues to a final CCD. This CCD is mounted on a peg attached directly to the SCT through a hole cut into the x-ray support tube. Two further CCDs of the same design are mounted on the scanning head and positioned so that they collect light from the scanning head's two beam splitters. Figure 8.3 shows a simplified diagram of the optical position measurement system.

The data produced by each CCD can be used to determine the position of the laser beam on its surface. The location of the laser beam on the surface of the two CCDs mounted on the scanning head is dependant on the position and orientation of the pair

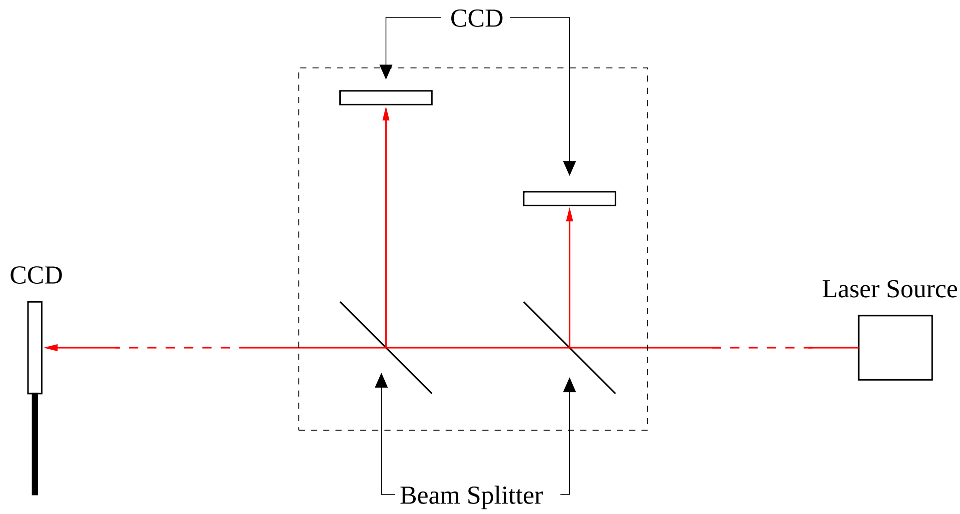

Figure 8.3: A diagram of the optical position measurement system incorporated into the x-ray survey equipment. The system consists of two beam splitters and a pair of CCDs mounted on the scanning head combined with a laser and CCD mounted on the support tube and SCT respectively. The components mounted on the scanning head are enclosed with a black dashed line in the diagram.

of beam splitters relative to the beam. The location of the beam on the final CCD can be used to measure any deviation in the relative positions of the SCT and the beam.

The second measurement system consisted of a number of solid state tilt sensors which are mounted on the scanning head. These devices report the absolute orientation relative to the direction of gravity. The combination of the data from the optical system and the tilt sensors can be used to completely determine the orientation of the scanning head as well as any translation in the xy plane.

The commercially available tilt sensors were not incorporated into the system during this work. The optical alignment system was tested but is not reported here. These alignment systems are not required for the critical calibration work described in chapter 10.

8.6 Control Software

Software was written to control both the linear and rotary motor stages through a graphical user interface. The software is capable of monitoring the position of both stages through the feedback they provide to the motor control hardware. The software incorporates a TCP/IP based communication system for the purpose of synchronisation with the SCT module readout system discussed in chapter 9.

The software used to control the x-ray positioning system was largely written in LabView 7.0[33], a commercially available high-level programming language which provides a graphical environment in which programs are constructed and viewed as flow diagrams. Simple drivers were provided by AEROTECH which allowed easy interface between the LabView program and the motor control hardware.

During the course of the x-ray calibration work discussed in chapter 10 the rotary stage was moved to a given position in ϕ and then stabilised for the period of data taking. The process was repeated many times and the software was designed to make this simple and reliable. A feature was implemented enabling the user to specify an angle (in units of machine steps) through which the rotary stage should move and the number of times this movement should be repeated. After each change in position, when the rotary stage had stabilised[3], a message was sent to the SCT Test DAQ system causing it to read out all of the SCT modules. After a time delay (chosen to be longer than the time required to finish reading out the modules) the process would be repeated. This continued until the range of positions specified by the user had been covered.

[3]The position of the rotary stage was monitored continuously until the difference between the positions of the stage in several successive measurements was smaller than a preset value. This was done to ensure that the position of the x-ray beam was stable before data taking began.

8.7 Summary

The x-ray survey system relies on two electric motors to rotate the x-ray source in the ϕ direction and position it along the z-axis. The position of the x-ray scanning head is measured by a number of different devices. These include an optical strip reader, an optical alignment system and a series of solid state tilt sensors. The rotation of the x-ray source in ϕ was measured using an encoder built into the rotary stage motor.

The electric motors and the optical strip reader incorporated into the linear stage were configured and tested during this work.

9

X-ray Detection System

9.1 Introduction

The x-ray survey of the ATLAS SCT relies on the ability of the SCT modules to detect x-rays produced by the surveying equipment. The testing and calibration of the x-ray system required the use of several SCT modules that were correctly configured to detect x-rays. The work involved in building and configuring the x-ray test detection system is described in this chapter.

The setup of the ATLAS SCT silicon modules is described in the section 9.2. This is followed by section 9.3 describing the Data Acquisition (DAQ) system that was used to service and communicate with the modules. Section 9.4 details the results of operating the x-ray detectors.

9.2 SCT Modules

An ATLAS SCT module[22] has a total of 768 separate strips on each side. These strips are read out by 12 separate ABCD chips, each chip governing 128 strips. The modules employ a binary readout system and a hit is identified as a strip containing more charge than a predefined signal threshold.

The ATLAS SCT modules have an entirely digital readout system and have been optimised for minimum ionising particles. The photons produced by the x-ray system have an energy of $\sim 27KeV$ and will produce a detectable signal but their probability of interacting with an SCT module is very low. In order to accommodate the needs of the x-ray survey the ATLAS SCT modules were designed with an x-ray, or *accumulation* mode. A module records a hit or a miss on each strip every $25ns$[1]. When in accumulation mode, the module performs a logical OR of all the $25ns$ bins over a pre-determined integration window every time a trigger is received. Accumulation mode multiplies the occupancy of a strip by the size of the integration window. The rate at which hits can be read out from a module is limited and the hit occupancy produced by an x-ray beam is small. Without accumulation mode it would take a prohibitively long time to readout sufficient x-ray hits from a module and determine the position of the beam.

The response of the silicon modules to x-rays is likely to change between strips. To correct for this inconsistent response, two separate x-ray beams are produced by each arm of the scanning head. This leads to a total of 4 x-ray beams. One of these beams from each arm has a much larger cross section than the other. This wide beam is known to have a flat distribution in $r\phi$ and can be used to determine the response of different strips on a

[1] A hit or miss is determined by comparing the charge accumulated on a strip in the $25ns$ period to a threshold

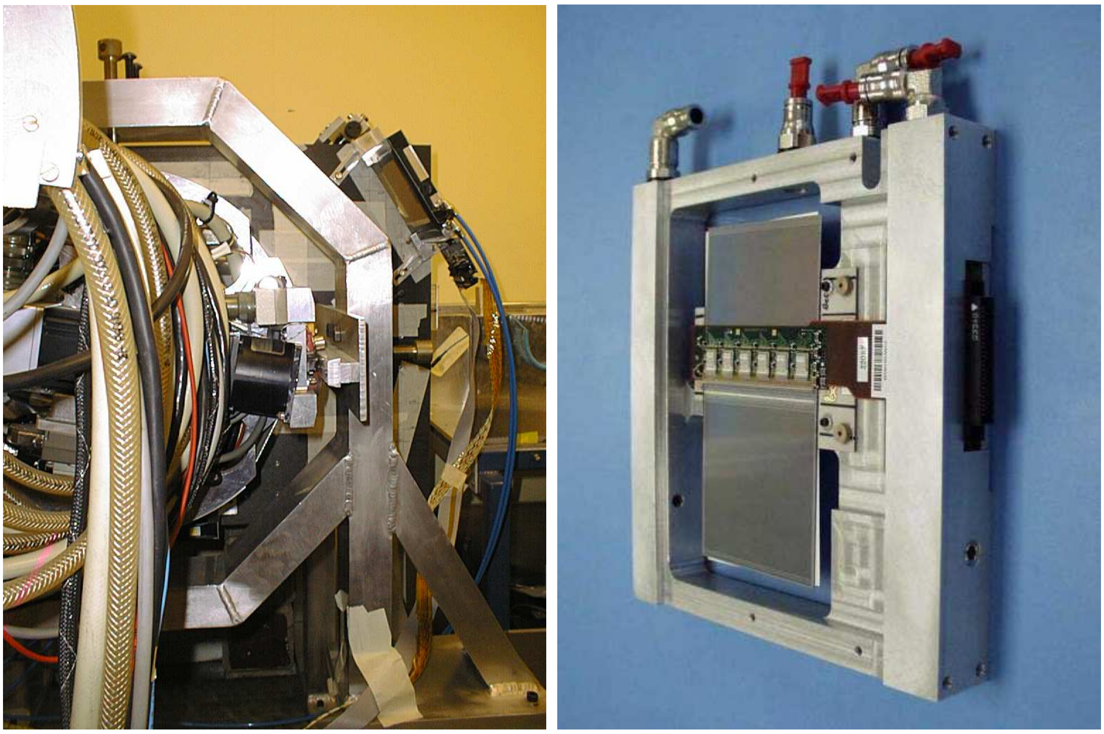

(a) (b)

Figure 9.1: (a) Photograph showing the calibration setup. The scanning head is shown to the left, in front of the optical table. A test beam case containing a module is shown in the top right corner of the optical table. (b) Photograph showing an SCT barrel module mounted in a test beam case (front and back panels removed).

module. Position measurements are made by fitting a Gaussian to the signal produced by the narrow beam after it has been divided by the signal produced by the wide beam when incident on the same part of a module. This procedure produces a marked improvement in the x-ray system's position resolution.

9.2.1 Configuration

The SCT silicon modules incorporate a number of configuration options which are designed to increase flexibility and operation lifetime. The configuration of the modules can be determined by the SCT DAQ system. Options are set in DAQ software and transmitted to the modules during initialisation. The accumulation mode can be activated and configured using a number of these configuration options.

During the x-ray work, the modules operated in accumulation mode. Without activating the accumulation mode, the modules are designed to read out the signal from each strip every 25ns. A hit is recorded if the signal in a strip exceeds the predefined signal threshold. The hits are recorded as logical 1's or 0's in a buffer held on the modules. A hit is only transmitted off the module if a trigger signal is received for the exact time the hit was recorded. The modules are capable of reading out the strips much faster than they can transmit hit information. The design of the modules makes it impossible to transmit every single recorded hit. Operating in accumulation mode, the module performs a logical OR of all the bits held in its buffer within the predefined integration window. A hit is recorded if any of the 25ns periods within the last integration window contained a signal above the threshold. The accumulation mode effectively sums the probability of observing an x-ray hit over all the bins in the integration window. This has the effect of reducing the time required to record sufficient hits to accurately determine the position of an x-ray beam in the module.

The results presented in this work were produced using accumulation mode with an integration window of $5\mu s$. The length of the window was set by multiplying the 25ns clock period by 200. When in accumulation mode, the coefficient of this multiplication is determined by the *com delay* option. When accumulation mode is inactive, the com delay option has a different purpose and is used primarily to determine the levels of cross talk between modules during the commissioning of the SCT. Each module's signal threshold was set to $140mv$ with a High Voltage (HV) p.d. of $75V$. A summary of the SCT module

configuration option	value
threshold	140mv
HV	75V
accumulation mode	true
com delay	200
trigger type	SR+L1A (type 31)
number of triggers	30000

Table 9.1: Summary of changes to the default SCT module configuration used during the x-ray survey test and calibration work.

configuration that were changed as part of the x-ray work along with the final values used is given in table 9.1.

9.2.2 Calibration

The production mechanism used for the SCT modules means that each one is unique. The response of detector strips to ionising radiation varies across a module due to inconsistencies in the silicon, the local doping and the wire bonds between strip and chip. A strip's response can also vary between chips and will change during the lifetime of the modules as they operate in the harsh radiation environment of the ID. These variations can be accounted for by applying a different weight to the threshold values applied to each strip. These weights can be found automatically using the SCT Test DAQ software. The weight's are stored in a *trim file* which is associated with each module. The range of values that the weights can take is limited by the design of the ABCD read out chips which use a 4-bit digital-to-analogue converter to apply the threshold correction. However, the weights on each chip represent a fraction of a specified *trim range* which can be different for each chip. This allows for finer tuning of weights over a smaller range on well behaved chips and a courser tuning over a larger range on poorer chips. There are also a number of modules that contain broken strips which fail to respond correctly, either by not communicating at all or always returning the same hit/no hit result. These strips are usually referred to as *dead* or *stuck* channels and hits reported by them must be ignored. Broken channels can be removed from a module's configuration by passing a *mask* to each chip on a module, detailing which strips should be ignored. The masks for each module are stored in a mask file.

The SCT modules were manufactured in a number of different locations and then tested extensively. The highest quality modules were assigned to the inner most parts of the SCT, nearest the interaction point. The lower quality modules were assigned to the outer barrels. The poorest modules were reserved for use only in the case of an accident damaging better modules or rejected entirely. The modules made available for the x-ray calibration work were rejects and contained a high number of broken strips and in one case physical damage to the silicon resulting from an accident during assembly.

Trim and mask files are calculated for each module and stored centrally by the ATLAS collaboration. Each module has a unique serial number which can be used to identify it and discover its history, calibration files etc. These centrally stored calibration files could not be applied to the damaged modules used in the x-ray test setup. The damage they had received altered the properties of those modules. The settings used when the modules were in x-ray mode also served to alter the response of the module strips from those measured centrally. The SCT Test DAQ setup that was assembled for the x-ray work was used to recalculate the module trim files and the initial mask files. The automated process was capable of identifying channels which needed masking off, but additional channels were masked by hand, specifically those in the physically damaged region of one of the modules.

9.2.3 Mounting

The SCT modules were mounted on an optical table in a variety of positions relative to the x-ray source. The modules had to be protected from physical damage during the testing and also required cooling to remove heat produced during operation. The detector strips on the modules were sensitive to visible light so had to be covered during operation in order to produce reasonable signals. The modules also needed to be properly grounded to shield them from external electrical noise during data taking.

Housing

The delicate nature of the SCT modules made it necessary to put them inside protective cases whilst they were used in the x-ray test and calibration work. The cases used were made primarily from aluminium and were originally designed for use in ATLAS test beam. A photograph of a module mounted in a test beam case is shown in figure 9.1 (b).

The two sides of the case which run parallel to the plane of the detector were replaced with perspex windows that are transparent to x-rays. A number of these windows were already in existence but were unfortunately transparent to visible light as well. The SCT modules are sensitive to visible light so electrical insulation tape was applied to ensure that the cases were light tight.

Each of the three test beam cases used had a slightly different construction, as did the *patch cards* which served to connect the modules inside the cases to a set of ports on the outside of the cases. The integration windows used when the modules are in accumulation mode coupled with the relatively low signal threshold required for x-rays makes them especially sensitive to noise[2]. Electrical shielding for the modules was provided by ensuring

[2]Increased sensitivity to the weak signals produced by x-ray photons is the reason for the existence of

a good electrical connection between both the analog and digital ground and the test beam case in which each module was housed. The different designs of the patch cards and test beam cases meant that this electrical connection already existed for some of the module-case combinations but not others. Modifications had to be made to some of the patch cards and one of the support cards to ensure all the modules were adequately shielded.

Cooling

The test beam cases incorporated a cooling loop consisting of a u-shaped channel cut directly into the aluminium underneath the point where the SCT module's berillia base plate is attached. Thermally conductive silicon grease was placed between the surface of the aluminium case and the module's base plate to ensure good thermal contact.

The two ends of the test beam case's cooling loop are fitted with $6mm$ diameter push fittings. A small cooling system was designed and built for the SCT modules used during the x-ray test and calibration work. The system consisted of a radiator and a pump which both used $10mm$ diameter piping. The $10mm$ pipes were then split into 3 loops of $6mm$ diameter pipes using a simple manifold. Each of the loops cooled one of the three SCT modules that were in operation. The coolant was distilled H_2O with approximately 25 percent anti-freeze. This was intended to inhibit the growth of algae etc.

As the cooling system used a conductive coolant, it posed a potential hazard to the SCT modules. To mitigate the risk, the cooling system was leak tested before use and PTFE tape was applied to all screw fittings. The push fittings proved to be water tight only when the end of the plastic piping used was sufficiently flat and perpendicular to the shaft of the pipe. The pipes involved in the push fitting joints had to be trimmed and

---

an accumulation mode.

the joints leak tested several times.

The test beam cases also allow attachment of a dry air supply to the module via a second pair of $6mm$ push fittings. Dry air is used to prevent condensation from forming on the surface of the modules and only becomes necessary when modules are cooled to a temperature below the dew point. During normal operation as part of the ATLAS SCT the modules are cooled to $-20°C$ in order to maximise their operational lifetime in the harsh radiation environment. However, the modules can safely operate at room temperature and remain stable at temperatures up to $\sim 60°C$.

The operating temperature of the SCT modules was approximately $30°C$ when the small cooling system was employed and didn't drop below room temperature. This made the dry air supply unnecessary.

Positioning

The modules inside the test beam cases were mounted on a carbon fibre optical table using a set of specially designed aluminium clamps. The optical table was approximately $1.5m$ by $1m$ and had threaded holes for M5 screws positioned on a square $5cm$ grid. The mounting clamps were designed so that the module cases didn't have to be aligned with the table's square grid. This was necessary because the modules had to be mounted on a tangent to the rotation of the x-ray scanning head.

The x-ray calibration procedure (described in chapter 10) demanded that the modules be placed in a number of different positions relative to the x-ray source. The accuracy required in the placement of the modules was approximately $1cm$ but those positions then needed to be known with a precision of $1mm$. This was achieved by applying masking tape to the optical table before attaching the modules. The positions of three separate fiducial points defined on each of the module cases[3] was then marked on the tape. After x-ray data taking had been completed and the modules removed from the table the positions of the marks was measured using a rule. Figure 9.1 (a) shows a module (inside a test beam case) mounted on the optical table.

9.3 SCT Test DAQ

The assembly of the SCT involved the manufacture of over 4000 silicon modules, each of which was tested before and after shipping between various institutions around the world. Further testing and calibration was carried out before and after mounting on the SCT's support structure. A dedicated *SCT Test DAQ* was designed for these operations.

The SCT test DAQ system was used for the x-ray survey test work. The system supplied all power, clock and command signals as well as reading data from the modules and storing it in an accessible file format.

The Test DAQ assembled for use in the x-ray work consisted of a number of VME boards that were mounted in a VME crate. An interface board connected the crate to a PCI card mounted in a desktop PC. Figure 9.2 shows a photograph of the SCT test DAQ.

The purpose of the various components in the SCT test DAQ system is outlined below.

VME Crate The crate includes a VME (**V**ersa**M**odule **E**urocard) bus which runs along the back plane behind the component boards and allows for communication between them. The crate used in the Test DAQ system was modified to provide a $-5.2V$ supply on specific pins of the J2 back plane, as required by the component boards.

[3]The position of each module relative to these marks was also measured using a rule and used to find the approximate position of each module from the position of the marks on the optical table.

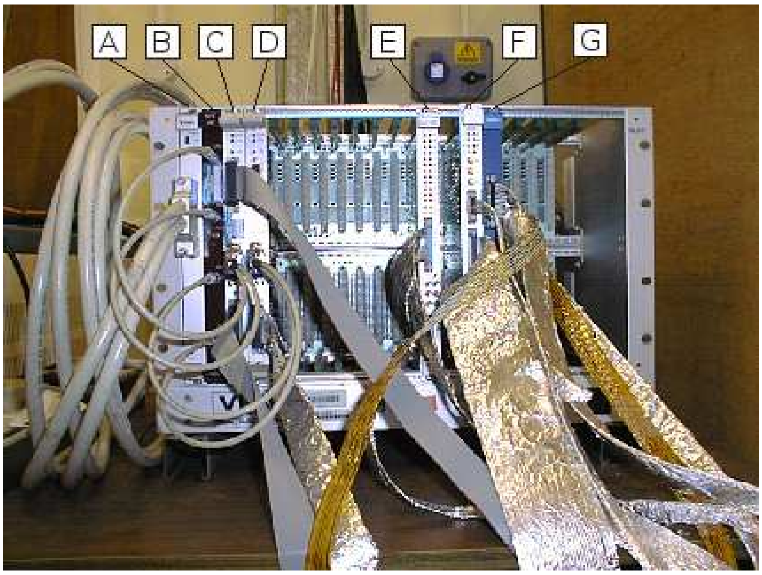

Figure 9.2: A photograph of the SCT Test DAQ system used to readout the silicon modules as part of the x-ray survey test work. The image shows the VME crate containing, from left to right; (a) VME interface, (b) HV supply, (c) 1st LV supply, (d) 2nd LV supply, (c) MuSTARD, (d) SLOG and (e) PPR.

The component boards were configured (by moving jumpers) to receive the $-5.2V$ supply from the J2 back plane instead of the JAUX connector (as they would in a CERN standard crate).

VME interface Facilitates communication between an external PCI controller card in the computer and the other VME modules on the bus.

HV Supply Provides the High Voltage (HV) supply required by the modules. Each HV board produces four separate HV supplies.

LV Supply Provides the Low Voltage (LV) power supply required by the modules. Each LV board houses two LV power supplies. The HV for the modules is routed via the LV boards and is output on the same IDC cable as the LV.

SLOG The **SL**ow command **G**enerator (SLOG) module sends commands to the SCT modules over an IDC cable. The SLOG is based around 16 32K blocks of RAM. Command strings can be placed in this array of memory and sent to the modules one at a time. The SLOG module is also used to generate the 40MHz clock signal required to synchronise communication with the SCT silicon modules in the x-ray setup. A separate module (CLOAC) exists for this and other purposes but was not used in the x-ray work.

MuSTARD The **Mu**ltichannel **S**emiconductor **T**racker **A**BCD **R**eadout **D**evice (MuSTARD) module is employed to readout the SCT silicon module. The board can read signals from the modules, decode them and construct events which are made available to the PC via the VME interface. The board is also able to construct histograms of the data retrieved from the modules and make these available.

PPR The **P**atch **P**anel **R**eplacer is a passive component that has no connection to the crate back plane. The PPR consists of a number of sockets which serve to connect a single MuSTARD to up to six SCT silicon modules.

Support Card The support cards provide an interface between the modules and the Test DAQ. Signals produced by the modules are typically buffered by repeater chips on the support card. The support card attaches to a module via a small patch card which is incorporated into the test beam cases. The patch card provides a mechanically robust connection with the module and electrical connection between the test beam case and ground.

The SCT test DAQ control software was written in the ROOT framework[32] and consists largely of a series of root macros that are run through an interpreter and need not be compiled. Some of these macros were modified to include the x-ray specific configuration options detailed in table 9.1 to ensure that the modules were correctly configured automatically.

The calibration procedure (chapter 10) involved positioning the x-ray source using the motor control software, waiting for the position to stabilise and then reading out data from the modules. In order to facilitate automatic data taking in multiple positions a simple TCP/IP based communication system was added to the Test DAQ software. This enabled the DAQ to send triggers to each of the modules in response to a message from the motor control software. The message included the current position of the x-ray source which was stored, along with the data readout from the modules (and the time at which the data was taken), in a ROOT file.

9.4 Results

The DAQ system and the modules were successfully used to detect the x-rays produced by the survey equipment. Figure 9.3 shows an example of the data retrieved from one of the modules during an exposure to both the narrow and wide x-ray beams.

9.5 Summary

ATLAS SCT modules were used as the detection element in the studies in order to properly evaluate the performance of the x-ray survey equipment. The SCT test DAQ was adapted for use in reading out three SCT silicon barrel modules. The modules were mounted inside ATLAS test beam cases. A cooling system was built and used to maintain the module's operating temperature at approximately $30°C$. The modules were re-calibrated to account

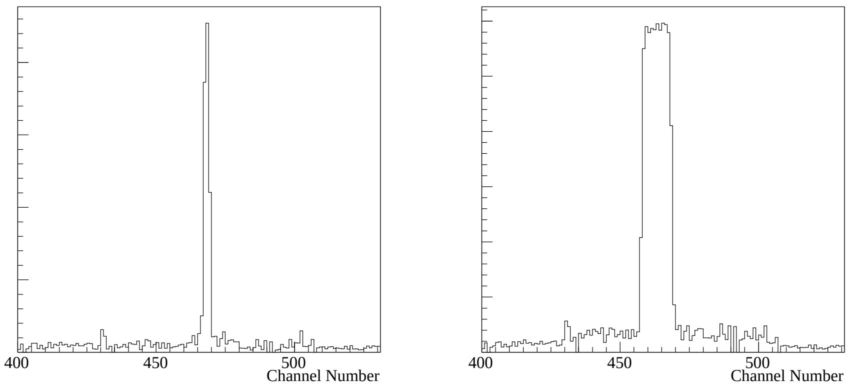

(a) (b)

Figure 9.3: Figure showing an example of the data collected from an SCT silicon module when the (a) narrow and (b) wide x-ray beam is incident on its surface. The plots shown were taken from side 0 of module 0 in run 1 of the x-ray calibration data taking as described in chapter 10.

for damage received before reaching the x-ray and configured for x-ray detection.

The SCT Test DAQ software was modified to include x-ray specific configuration options as defaults. An additional TCP/IP based interface was implemented so that the module readout process could be controlled remotely. The process of moving the x-ray source and subsequently taking data from the modules was then automated.

10

X-ray Scanning Head Calibration

10.1 Introduction

The x-ray survey system produces a total of four x-ray beams, two wide and two narrow. These beams emanate from a single source and are shaped by two pairs of collimators, all of which are mounted on the rotary stage of the x-ray scanning head. Chapter 8 describes the positioning and position measurement systems incorporated into the x-ray scanning head. The interpretation of data from an x-ray survey would rely on using the measurements taken from these systems to calculate the position of the x-ray beams. Extensive measurements of the x-ray scanning head are required in order to place constraints on all the degrees of freedom involved in its construction and find the relationship between the position of the scanning head and the location of the x-ray beams in the SCT. This chapter describes the work undertaken to measure this relationship and calibrate the x-ray scanning heads rotary stage.

10.2 Experimental Setup

The setup used to calibrate the scanning head was designed to replicate the x-ray machines intended operation. Three modules were used to measure the position of the x-ray beams. An optical table was positioned perpendicular to the axis of the scanning head's rotary stage. The modules were mounted on this table using clamps and beam test boxes as described in chapter 9. The modules were arranged around the x-ray scanning head with the plane of each detector orientated towards the z-axis. They were aligned such that their active detector strips ran approximately parallel to the axis of the rotary stage. The configuration is shown in figure 10.1.

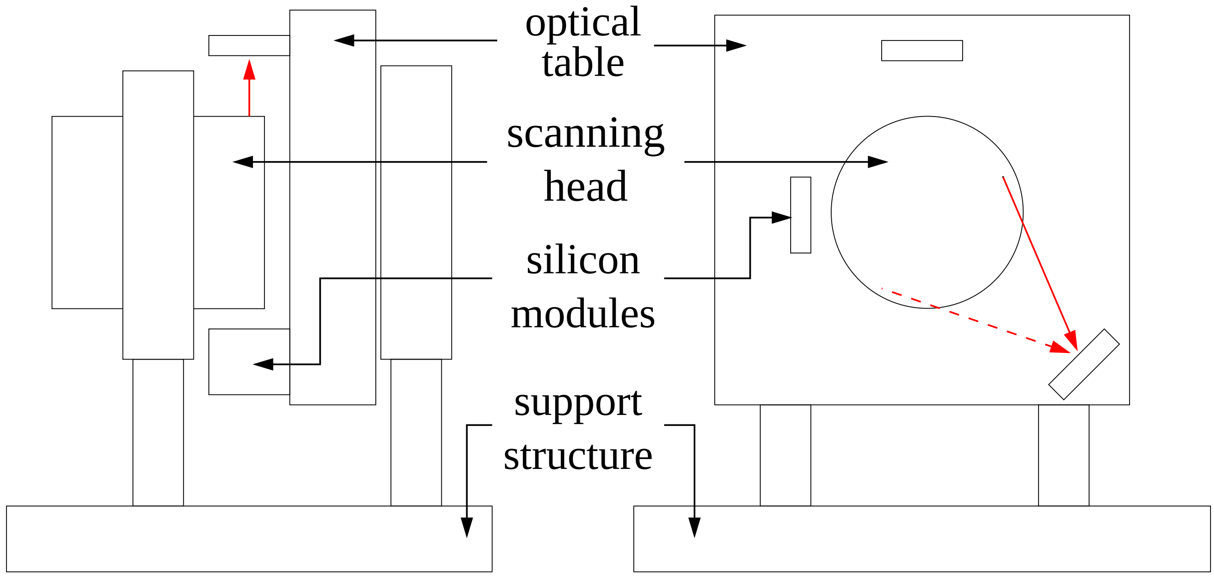

Figure 10.1: Diagram showing the relative positions of the x-ray scanning head and the SCT modules as they were mounted on the optical table. The left had diagram shows a view from the side of the scanning head (a projection in the yz plane) whilst the right hand diagram shows a view from the back of the scanning head (a projection in the xy plane). The optical table and the scanning head are mounted on a support structure. The silicon modules are shown mounted on the optical table. The red lines indicate the x-ray beams in some of the possible orientations. The solid and dashed red lines in the right hand diagram illustrate the positions of the beams emitted from the 1^{st} and 2^{nd} collimators when the scanning head is in two different positions.

The x-ray scanning head is designed to rest on the pair of rails that run along the inside of the support tube. For the purposes of the calibration work the scanning head was not placed inside the support tube but instead rested in a different support structure. This consisted of a hexagonal steal frame which was bolted to the same plinth as the optical table's support frame. The frame included two short aluminium rails of similar dimensions to those in the carbon fibre support tube. The scanning head was placed on these rails and clamped into position with a pair of brass bolts. The bolts were positioned directly above and below the scanning head and passed through the support frame. Tapered holes cut into the frame of the scanning head received the bolts and ensured they were located correctly.

The modules were read out using the DAQ system (chapter 9). The support card and cabling were always positioned on the positive side of the module with respect to the direction of ϕ in the scanning heads coordinate frame. This meant that the support card's position in ϕ was always larger than the that of the modules centre. This rule ensured that the orientation of each module remained consistent between successive runs[1].

Three different sets of module positions were used for the calibration (table 10.1). The modules were positioned by hand on the optical table. The position of each module box was marked on masking tape which had been applied to the optical table underneath the expected positions of the modules. The marked positions were measured with a precision of $\sim 1mm$ after the run had been completed and the modules removed from the table.

The data produced by the calibration work was interpretation using software originally designed for the survey of the completed SCT. The calibration served as an aid to the development and testing of this software.

[1]This determined the side of the module facing the x-ray source and the order in which strips were traversed during a scan

	module 1	module 2	module 3
set 1	(400, 250)	(0, -250)	(-340, 250)
set 2	(400, -170)	(0, 250)	(400, -250)
set 3	(360, 0)	(50, 250)	(-360, -80)

Table 10.1: Summary of the position of the SCT modules used during each calibration data taking run. The positions are represented as coordinates in the xy plane occupied by the optical table. All dimensions are given in mm. The coordinates are relative to the centre of the optical table which was approximately in line with the centre of rotation of the x-ray scanning head.

10.3 Control Software

The SCT Test DAQ control software is based on the ROOT [32] software framework and consists of a collection of C macros running in the CINT interpreter. The x-ray motor control software has been written in LabView and has been described in chapter 8.

During the calibration work the motor control software and the Test DAQ software ran independently on separate computers. The data taking from the modules was synchronised with the positioning of the x-ray beam by transmitting the position from the motor control software to the DAQ system via a TCP/IP connection.

A ROOT macro was written to handle the x-ray data taking and added to the Test DAQ software. The macro waited for position information from the motor control software, then sent 1000 level 1 triggers to each of the silicon modules. Data received from the modules was histogramed and stored using the received position as part of the file name.

10.4 X-Ray Beam Positioning

Each arm of the x-ray scanning head produced two x-ray beams (chapter 7). The wide x-ray beam is required to deconvolve the SCT module's x-ray response function from the data produced by the module when illuminated by the narrow x-ray beam. Therefore, it is necessary to ensure that every histogram produced with the narrow beam has an associated histogram produced using the wide beam that covers the same region of the detector. Further more, uncertainties in the shape of the wide beam near its edges mean that narrow beam must fall on a part of the module which is close to the centre of the associated wide beam.

The x-ray scanning had to be rotated through a particular angle to ensure that the narrow beam fell on the same part of a particular module as the preceding wide beam. The wide and narrow x-ray beams produced by each of the collimators were separated by a fixed angle. However, the beams were not emitted from the scanning head's centre of rotation. This meant that the rotation required to overlap the two beams was different for each module position and each collimator arm of the x-ray machine. The x-ray survey required that the positions of a number (~ 20) of different points be measured across the surface of each module. The survey of each module was performed by repeatedly moving the scanning head by a small angle, or *step* and taking data from the module. The wide beam would move across the module, followed by the narrow beam. The step size was chosen such that after ~ 20 steps the narrow beam would fall in the same position as the first position occupied by the wide beam.

The appropriate step sizes were calculated using an empirical method. All four of the x-ray beams were used to illuminate a number of positions ($\bigcirc(10)$) on each of the modules. Positions showing the wide and narrow beams were used to determine the separation between the two beams on the modules surface. The strip position of the narrow beam at two different points in ϕ was then used to determine the relationship between changes in strip position and movements in ϕ. The separation between wide and narrow beams was then converted from number of strips into degrees in ϕ. This gave the rotation of the x-ray source required to position the narrow beam in the place currently occupied by the wide beam. The appropriate step size could then be found by dividing the separation between beams by the number of points that were required across the module. This is summarised in equation 10.1.

$$Step\ size = (S_w - S_n).\frac{\phi^1 - \phi^0}{S_n^1 - S_n^0}.\frac{1}{n\ points} \tag{10.1}$$

Where S is strip number and ϕ the position of the rotary stage. Subscripts w and n indicate the wide and narrow beams whilst superscripts 0 and 1 indicate two different positions of the x-ray source.

The modules are flat and, as a result, lie on a tangent to a circle centred on the z-axis. The x-ray beams don't emanate from the centre of rotation (the z-axis) but from a point some distance away from it. This means that the optimum step size required to ensure overlap between the narrow and wide beams changes across the surface of each module. The width of the wide beam allows for some error in the step size. However, if a module is very close to the centre of rotation then it covers a greater range in ϕ and the effect becomes a problem.

The need for different step sizes for every module + collimator combination would present a problem during an actual survey of the SCT. The SCT barrel section contains modules with four different radii which would need to be scanned by beams from both of the x-ray collimator arms. Using the technique described above would require surveying the entire SCT with eight different step sizes which would take an unnecessary amount of work. Instead, the wide beam could potentially be made wider to ensure that all points on the SCT's surface were covered by it during successive scans. This would remove the

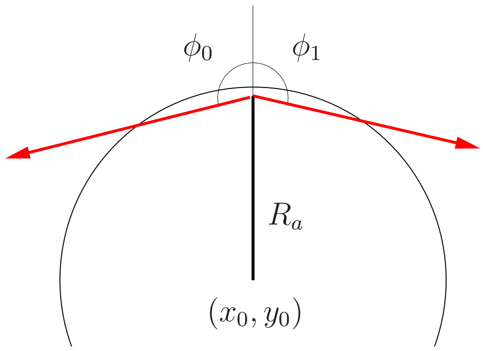

Figure 10.2: The parameters measured during the x-ray calibration procedure. The figure shows a simplified diagram of the x-ray scanning head viewed along the z-axis. The red lines represent the direction of the narrow x-ray beams whilst the thick black line indicates the separation between the centre of rotation of the scanning head and the position of the x-ray source.

need to calculate step sizes. Alternatively, a more complex software algorithm could be developed to minimise the number of survey points required to cover the entire SCT.

10.5 Analysis Software

The calibration procedure relied on the position reconstruction software described in chapter 7. The positions of all three modules in a single data set were reconstructed using an initial set of calibration parameters. The parameters were varied and the fit repeated until the χ^2 was minimised. The calibration fit parameters were the position of the scanning heads centre of rotation (x_0, y_0), the separation between this centre and the x-ray source R_a and the angle between each of the narrow beams and the line between the scanning head's centre and the x-ray source, ϕ_0 and ϕ_1. These parameters are indicated in figure 10.2 on a simplified diagram of the scanning head.

The measured positions of the modules (with an accuracy of a few mm) were used as an initial constraint on the fitting procedure but were removed as the fits began to converge. The 80μm separation between the active strips on the modules was precisely known and provided another important constraint in the fitting process.

10.6 Data Taking

Data taking followed a simple procedure that was largely automated in order to save time and reduce the possibility of introducing errors in record keeping. First, the approximate position of the modules in ϕ was calculated. From those positions the range in ϕ over which beams from each of the x-ray collimators was likely to pass through each of the three modules could be estimated. These ranges were then checked by moving the x-ray scanning head into the ϕ positions and examining the relative alignment of the collimators with the edges of the modules by eye. The SCT Test DAQ system was then turned on, the modules configured and the x-ray system HV supply ramped up. The control software was used to move the x-ray scanning head and take data over the previously determined ranges in ϕ with a step-size of 1 degree. This first set of data was then used to calculate an appropriate step-size to be used with each collimator for each module, six different step sizes in total. This initial data was also used to ensure that the ϕ ranges were correct. After the first run the x-ray system was disabled and the x-ray scanning head moved back to its starting position[2]. The x-ray system was then ramped up and the control software used to take data over the ranges in ϕ using the calculated step-sizes.

[2]This had to be done by hand without using the rotary stage motor. The design of the x-ray scanning head made it possible for the service cables to become tangled in the rotary limit switch system when the rotary stage turned in the negative ϕ direction. The tangled cables could cause damage to the limit switches. This problem in the design of the x-ray system would need to be resolved before it could be used for a full survey of the SCT.

Scanning a pair of beams (wide + narrow) from a single collimator across one module took approximately 20 minutes. This lead to a total time of 2 hours to scan all the module + beam combinations. The time required for preparation before the scans and measurements of the module positions afterwards meant that each run took approximately a day to complete.

The procedure described above was performed with modules in each of the three sets of positions noted above. Two further data sets were produced by putting the modules in the positions for data set 1 and then moving the x-ray scanning head by 22mm in the negative z direction (away from the optical table) and then moving back to the nominal z position used for the previous data sets.

During and after data taking the data sets collected were checked by hand to ensure an appropriate overlap between the wide and narrow beams.

10.7 Results

A total of five sets of data were used to produce the final calibration of the x-ray scanning head. Each of these sets contained data retrieved from three different modules and lead to a single set of calibrations parameters for the scanning head. Subsequently, each set of calibration parameters was used to reconstruct the position of each of the modules in each of the five different data sets. This generated a total of 75 ($5 \times 5 \times 3$) position measurements in co-ordinates of r and $r\phi$. The difference between those measurements and the mean of those measurements for each module position is plotted in figure 10.3 (a). The rms error is 27μm in the r direction and 7μm in the $r\phi$ direction. These errors show the uncertainty in the measured calibration parameters for the x-ray scanning head.

The measured calibration parameters were then used to reconstruct the positions

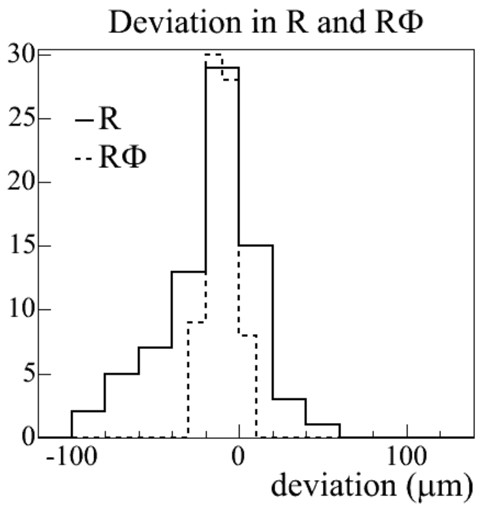

(a)

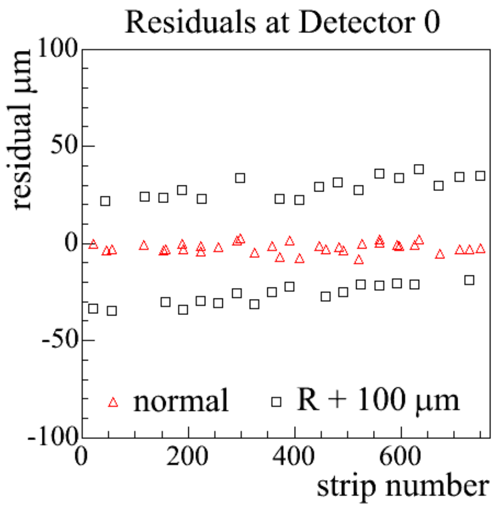

(b)

Figure 10.3: Shows some of the results from the x-ray calibration work. (a) shows the deviation from the mean reconstructed value for the module's position in $(r, r\phi)$ for all combinations of module position and calculated calibration parameters. (b) shows the residuals of reconstructed module positions using the measured calibration parameters as red triangles. The black squares indicate the distribution that would result if the measured radial co-ordinate r where wrong by 100μm.

of the silicon modules using the method described in chapter 7. The residuals for a typical detector are shown in figure 10.3 (b). This is the difference between the mean reconstructed position of the module plane in (x_m, y_m, ϕ_m) and the reconstructed position of each point on the module. The figure shows the residuals for the reconstructed points as red triangles and an example of the distribution of residuals that would be expected if the reconstructed points were displaced in the radial r direction by 100μm. The true residuals have an rms of 2.51μm which demonstrates that the positioning of the rotary stage motor in ϕ and the measured calibration parameters are correct to within $2-3\mu$m.

10.8 Summary

The work described in this chapter lead to a good understanding of the x-ray scanning heads construction. The relationship between the position of the rotary stage and the corresponding orientation of all four x-ray beams is now known to a degree of precision which satisfies the requirements of the x-ray survey.

Bibliography

[1] L. Vacavant, I. Hinchliffe *Signals of models with large extra dimensions in ATLAS* [JPG 27(2001) 1839]

[2] The ATLAS collaboration *ATLAS Detector and Physics Performance*
1999

[3] The ATLAS collaboration *ATLAS Inner Detector Technical Design Report Volume 1*
CERN/LHCC/97-16 ATLAS TDR 4 30 April 1997

[4] W.-M. Yao *et al Review of Particle Physics*
Journal of Physics **G** 33, 1 (2006)

[5] N. Arkani-Hamed, S. Dimopoulos and G. Dvali *The Hierarchy Problem and New Dimensions at a Millimetre*
Phys.Lett. B429 (1998) 263-272

[6] C.D.Hoyle, U.Schmidt, B.R.Heckel, E.G.Adelberger, J.H.Gundlach, D.J.Kapner and H.E.Swanson *Submillimeter Test of The Gravitational Inverse-Square Law: A Search for "Large" Extra Dimensions*
Phys. Rev. Lett. 86 1418 (2001)

[7] D.J. Kapner, T.S. Cook, E.G. Adelberger, J.H. Gundlach, B.R. Heckel, C.D. Hoyle, and H.E. Swanson *Tests of the Gravitational Inverse-Square Law below the Dark-Energy Length Scale*
arXiv:hep-ph/0611184 v1 14 Nov 2006

[8] Steen Hannestad and Georg G. Raffelt *Stringent Neutron-Star Limits on Large Extra Dimensions*
Phys. Rev. Lett 88 071301 (2002)

[9] V. Kabachenko, A. Miagkov, A. Zenin *Sensitivity of the ATLAS detector to extra dimensions in di-photon and di-lepton production processes*
ATL-PHYS-2001-012

[10] L. Randall, R. Sundrum *Large Mass Hierarchy from a Small Extra Dimension*
Phys. Rev. Lett., 83(17):3370-3, 1999

[11] J. Goldstein, S. Harper and P. Renton *The Search for New Physics in High Mass Di-Electron Events in* $\mathbf{p\bar{p}}$ *Collisions at* $\sqrt{\mathbf{s}}$ *= 1.96 TeV*
CDF/PUB/EXOTIC/PUBLIC/8694

[12] S. Hawking *Black hole explosions (quantum gravitational thermal emission)*
Nature. Vol. 248, pp. 30, 31. 1 Mar. 1974

[13] R. Casadio, B. Harms *Can black holes and naked singularities be detected in accelerators?*
Int. J. Mod. Phys. A 17 (2002) 4635 [hep-th/0110255].

[14] G. Corcella, I.G. Knowles, G. Marchesini, S. Moretti, K. Odagiri, P. Richardson, M.H. Seymour and B.R. Webber, *HERWIG 6.5*
JHEP 0101 (2001) 010, [hep-ph/0011363], hep-ph/0210213

[15] C. Harris, P. Richardson, B. Webber *CHARYBDIS: A Black Hole Event Generator*
CERN-TH/2003-170

[16] *Geant4 developments and applications*
IEEE Transactions on Nuclear Science 53 No. 1 (2006) 270-278

[17] C. Harris, M. Palmer, M. Parker, P. Richardson *Exploring Higher Dimensional Black Holes At The Large Hadron Collider*
JHEP05(2005)053

[18] J.M. Butterworth, J.R. Forshaw, M.H. Seymour *Multiparton interactions in photoproduction at HERA*
Z.Phys.C72:637-646, 1996

[19] Leif Lönnblad *et. al CLHEP - a class library for particle physics* version 2.0.4.1 - 18th October 2006

[20] ATLAS Collaboration *Calorimeter Performance Technical Design Report*
CERN/LHCC 96-40 13th January 1997

[21] G. Doucas, J. Grosse-Knetter, R. Nickerson, L. Vertogradov, *X-ray tomography for the ATLAS semi-conductor tracker*
NIMPH A 457 (2001) 43-51

[22] A. Abdesselam et al, *The Barrel Modules of the ATLAS SemiConductor Tracker*
Nuclear Instruments and Methods A568 (2006) 642-671

[23] *x-ray tube supplier*

[24] Application Software Group, Computing and Network Division, CERN, *MINUIT Reference Manual*

[25] *Aerotech inc.*
101 Zeta Drive, Pittsburgh, PA 15238, USA

[26] Aerotech inc, *PC-Card Multi-Axis Motion Controller*
20 Oct 2006 http://www.aerotech.com/products/pdf/u500.pdf

[27] Aerotech inc, *Drive Racks*
15 Sep 2004 http://www.aerotech.com/products/pdf/DriveRacks.pdf

[28] Aerotech inc, *ADR175/240 Series Rotary Stages Mechanical-Bearing Rotary Stage*
31 Aug 2004 http://www.aerotech.com/products/pdf/adr175.pdf

[29] Aerotech inc, *BM Series Brushless Rotary Servomotors*
29 Nov 2006 http://www.aerotech.com/products/pdf/BM.pdf

[30] Aerotech inc, *MXH Series High Resolution Encoder Signal Multiplier*
6 Feb 2007 http://www.aerotech.com/products/pdf/MX_MXH.pdf

[31] Renishaw PLC, *RGH25 Series Digital and Analogue Readhead data sheet*
http://resources.renishaw.com

[32] Rene Brun and Fons Rademakers, *ROOT - An Object Oriented Data Analysis Framework*

Proceedings AIHENP'96 Workshop, Lausanne, Sep. 1996, Nucl. Inst. & Meth. in Phys. Res. A 389 (1997) 81-86. See also http://root.cern.ch/.

[33] *LabVIEW*
National Instruments Corporation, Austin, Texas